TIME RESOLVED STUDIES OF SHOCK WAVE PROPAGATION IN LASER IRRADIATED TARGETS

by

Andrew James Rankin

A thesis submitted for the degree of
Doctor of Philosophy of the University
of London and for the Diploma of
Membership of Imperial College

July 1985

The Blackett Laboratory
Imperial College of Science and Technology
London SW7 2BZ

ABSTRACT

Experimental research using high power lasers to irradiate foil targets at wavelengths of 1.06, 0.53 and 0.35 μm has been performed. The measurements made have centred on a common theme of shockwave propagation and have involved four complementary areas which are relevant in the understanding of laser irradiation of materials. These are : the measurement of shockwave velocity and the development of a low level preheat diagnostic, the observation of shock transit through a multilayer target, comparative measurements of the smoothing of imposed laser beam inhomogeneities and the compression of material to high density using colliding shockwaves.

Shockwave velocities have been measured using stepped target emission to infer shock pressures at laser wavelengths of 0.53 and 0.35 μm. An accurate scaling of pressure as a function of irradiance has been obtained for 0.53 μm and pressure enhancement using 0.35 μm radiation has been demonstrated. A dual channel low level preheat diagnostic has been developed and used to measure shock and preheat temperatures in aluminium foils in the range 0-2 eV and 0.1-0.5 eV respectively.

The use of a multilayer transparent target to diagnose the position of the shockfront during irradiation has been introduced. Colour enhancement of streak camera images has

revealed a temporal emission sequence which shows abrupt changes in shock luminosity as the shockfront crosses the boundary between materials of different acoustic impedance.

Measurements of the smoothing of imposed laser beam inhomogeneities using three different techniques are described. Results using a previously untried modulated shock transit time approach show degrees of smoothing which are significantly lower than those reported previously. It is concluded that previous studies are likely to have been dominated by hydrodynamic effects inherent with target acceleration based measurements.

The thesis is concluded with time resolved X-ray radiographic measurements using dual and single sided 0.53 μm irradiation to compress materials to high density. Compressions of the order of six and three respectively have inferred density enhancements of the order of two by using colliding shockwaves. Single sided irradiation has allowed the simultaneous measurement of shockwave and particle velocities defining a point on the E.O.S. for mylar. Computer simulations using the 1-d hydrocode MEDUSA have shown good agreement in both cases.

CONTENTS

ACKNOWLEDGEMENTS

The author would like to express his gratitude to Dr J.D. Kilkenny (his supervisor) for his guidance and support throughout the duration of this work. He would also like to acknowledge the assistance and co-operation of Dr D.K. Bradley and Dr J.D. Hares of Imperial College, Dr A.J. Cole and Dr S.J. Rose of the Rutherford Appleton Laboratory, and Dr P.D. Carter, Dr N.J. Freeman and Dr P.C. Thompson of the Atomic Weapons Research Establishment, Aldermaston.

This work would not have been possible without the support of the staff of the Rutherford Appleton Laboratory Central Laser Facility in target preparation, target area and laser control. The author would like to thank AWRE Aldermaston for making it possible for him to perform experiments using the Merlin laser system and the use of their image analysis facilities. Thanks are due to the Merlin laser team and the target preparation group.

The work in this thesis was performed whilst the author was supported by a Science and Engineering Research Council grant.

LIST OF FIGURES

LIST OF TABLES

CHAPTER ONE

INTRODUCTION

1.1 Abstract

A brief outline of the physics of laser compression of matter to high density is given with emphasis on processes relevant to the topics covered in the thesis. The work contained in the following chapters is summarised stressing the role of the author.

1.2 Introduction

This chapter serves as a general introduction to the thesis providing a background to the experiments described in later chapters. The underlying theme of laser compression research was principally inspired by Nuckolls and co-workers[1.1] in 1972 with the publication in the literature of a scheme to compress spherical targets to high density using a high power pulsed laser. The pressures generated by the spherically converging shockwaves, driven by material ablation, would produce densities and temperatures of the order of 1000 g cm^{-3} and 10^8 K respectively. Potential applications of laser compression include the study of hot matter in conditions comparable to those in the centre of the sun (density $\sim$ 200 g cm^{-3} and temperature $\sim$ 1-2 keV) and the generation of controlled

thermonuclear energy using hydrogen isotopes as a basic fuel. A considerable amount of theoretical and experimental work has been invested in the study of laser irradiation of matter since that time. Although the attainment of the goal of a fusion power reactor is still remotely distant the complexity of the processes poses a challenge which is being met with intense activity. One noteworthy area of study is that of the properties of shockwaves and their application in diagnosing the state of laser irradiated targets.

1.3 Summary of the thesis/role of the author

The topics covered in the thesis have a common theme of the propagation of laser generated shockwaves in planar geometry. They range from direct measurements of the properties of shockwaves (shock velocity, temperature and density) to their use in diagnosing effects occurring in laser produced plasmas (e.g. thermal smoothing).

Chapter Two describes experiment to measure laser induced shock pressure at different wavelengths of irradiation. The measurement of shockwave velocity using shock heated thermal emission in stepped targets provides an accurate scaling relation between laser irradiance and pressure at a laser wavelength of 0.53 μm. Pressure enhancement at 0.35 μm has been achieved and attributed to the higher absorption fraction and hydrodynamic efficiencies predicted for these conditions.

Chapter Three demonstrates a technique to monitor the position of the shockfront at different times during laser irradiation. An abrupt change in shock luminosity signals the

transit of the shock as it crosses the interface of materials of different acoustic impedance. Such an approach holds potential as a time resolving diagnostic of the evolution of the spatial shape of the shockfront.

Chapter Four describes the development and use of a dual channel low level (few eV) temperature diagnostic which utilises the spectral content of the thermal emission from the rear of a laser irradiated foil. Shock and preheat temperatures in the range 0-2 eV have been measured.

Chapters Five and Six describe comparative measurements of the smoothing of imposed laser beam inhomogeneities at wavelengths of 1.06, 0.53 and 0.35 μm. A modulated shockwave transit approach measures smoothing rates lower than previous studies, the origin of which is discussed in the light of these new results.

A novel technique is introduced in Chapter Seven employing X-ray streaked radiography of thin bismuth tracer strips buried in mylar slab targets. The targets are strongly heated and highly compressed by the collision of two opposed shocks driven by dual sided 0.53 μm radiation. Single-sided irradiation has provided a simultaneous measurement of particle and shockwave velocity defining a point on the mylar E.O.S. Computer simulations using the 1-d hydrocode MEDUSA have given good agreement in both cases.

The experimental work, analysis, interpretation of the data and conclusions in all the chapters is entirely the work of the author with three exceptions. The computer simulations in Chapters Three and Seven were performed by Dr S.J. Rose,

practical assistance was provided by Dr A.J. Cole taking the measurements in Chapter Six and the experiments in Chapter Seven were performed in collaboration with Dr J.D. Hares and Dr D.K. Bradley.

1.4 Absorption of laser light

Several absorption mechanisms occur in laser irradiated material. The two major ones which will now be described are Inverse Bremsstrahlung absorption and resonance absorption which are more effective at low and high irradiance respectively.

1.4.1 The critical density

When laser light is incident on a plasma the refractive index of the plasma can be expressed as[1.2]

$$n_i = \left[1 - \left(\frac{\omega_p}{\omega_o}\right)^2\right]^{1/2} \qquad 1.1$$

This holds for the case when the electron ion collision frequency ν_{ei} is much less than the frequency of the laser light ω_o where the electron plasma frequency is defined by

$$\omega_p = \left(\frac{4\pi n_e^2}{m_e}\right)^{1/2} \qquad 1.2$$

From equation 1.1 it can be seen that when the laser

light frequency ω_o becomes greater than ω_p, the refractive index becomes imaginary and laser light can no longer propagate into the plasma. The light will be incident on an increasing density gradient and from equation 1.2 will only be able to propagate up to a density at which $\omega_p = \omega_o$. This is known as the critical density n_c

$$n_c = \frac{\omega_o^2 n_e}{4\pi e^2} \qquad 1.3$$

This gives

$$n_c = \frac{1.12 \times 10^{21} \text{ cm}^{-3}}{\lambda \text{ (/}\mu\text{m)}}$$

where λ is the laser wavelength in μm. Therefore for lower wavelength laser irradiation absorption takes place at higher densities.

1.4.2 Inverse Bremsstrahlung

Inverse Bremsstrahlung is the process by which an electron absorbs a photon in the coulomb field of an ion. The absorption coefficient K_i which describes this effect can be expressed as(1.2)

$$k_i = \frac{\nu_{ei}}{c} \left(\frac{\omega_p}{\omega_o}\right)^2 \frac{1}{[1 - (\omega_p/\omega_o)^2]^{1/2}} \qquad 1.4$$

where ν_{ei} = the electron ion collision frequency. This expression is true when $\omega_o >> \nu_{ei}$ which holds for the underdense region of the plasma where the laser light is absorbed. Inverse Bremsstrahlung is most effective at low irradiance ($\leqslant 10^{13}$ Wcm^{-2}) and short wavelengths (< 1 μm)(1.3,1.4). As high irradiance for a low z target inverse bremsstrahlung becomes insignificant and resonance absorption(1.5) becomes the dominant absorption mechanism.

1.4.3 Resonance absorption

When laser light is incident at angle θ_o to the target surface it will be refracted as it moves up the density gradient. Since the restriction $n_i \sin\theta$ = constant applies to the beam path the density at which the beam will be reflected is

$$n_e = n_c \cos^2 \theta_o \qquad 1.5$$

i.e. it is reflected before it reaches the critical density. This process of refraction and reflection of the laser by the density gradient is illustrated schematically in Fig.1.1.

If the incident laser light is p polarised it will have a component of its electric field vector parallel to the density gradient which can drive electrostatic plasma waves. If the density scale length L is short enough the electric field component can tunnel through to the critical density surface as

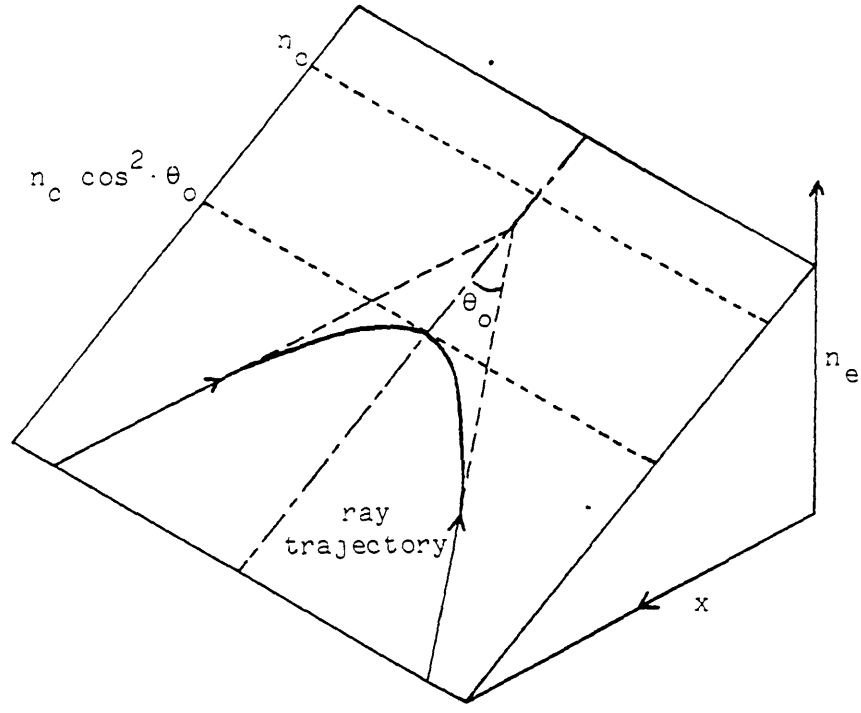

Fig.1.1 Schematic representation of an incident ray at angle θ_o to a density gradient illustrating resonance absorption mechanism.

an evanescent wave and resonantly excite the plasma waves. The energy coupled to these oscillations is transferred to the electrons around the critical density by wave breaking and

damping. This process of transferring incident laser light to the plasma is known as resonance absorption[1.5-1.7]. It is sensitive to both the angle θ_o and the density scale length. If θ_o of L is too large, the evanescent wave will not reach critical density and if θ_o is too small the parallel component of the electron field may be too weak. The optimum angle for resonance absorption can be given by[1.8,1.9]

$$\sin^2 \theta_o \left(\frac{L \omega_o}{c}\right)^{2/3} = 0.6 \qquad 1.6$$

For high intensity irradiation the light pressure or ponderomotive force[1.10] is comparable to the plasma pressure and steepens the density profile[1.7,1.11] enhancing resonance absorption. Up to 40% absorption may occur by this process[1.12].

There exist a number of other absorption mechanisms not described here such as the two plasmon instability[1.13], parametric decay instability[1.13] and the oscillating two stream instability[1.14].

1.5 Laser ablation

Laser energy is absorbed at or near the critical density surface and is transported to the solid target by electronic thermal conduction. Here the heated surface material responds to its own pressure by moving away from the target (ablating). Due to conservation of momentum, this ablation process drives a

compression or shockwave into the solid target acting as a 'rocket' effect. The driving or ablation pressure can be determined by measuring the rate at which material ablates (mass ablation rate[1.12]), or by measuring the velocity of the shockwave produced[1.15]. The ability to predict the ablation pressure for particular conditions of laser wavelength and irradiance is important in order to plan laser irradiation experiments. Much work has been done to measure mass ablation rates both in planar[1.16-1.19] and spherical geometry[1.16,1.20]. The difference in scaling with absorbed irradiance and wavelength between these two geometries has been attributed[1.21] to lateral transport of energy away from the laser focal spot in planar measurements.

1.6 Energy transport

Absorption of the laser energy takes place at densities up to critical density, whereas ablation of material from the target takes place at densities greater than critical. The transport of energy between the absorption and ablation regions is therefore important in the laser ablation process and the subsequent generation of shockwaves.

1.6.1 Thermal/flux-limited transport

Electron thermal conduction has been derived by Spitzer[1.22] in the limit of temperature scale lengths much larger than the electron mean free path. In the region between critical density and the ablation front temperature gradients are such that the temperature scale length is comparable to the

electron mean free path. An artificially imposed limiting factor is used in calculations at a maximum value corresponding to the so-called free 'streaming' heat flux. This is the case when all the electrons travel in the same direction with their thermal velocity. The saturated heat flux q_{sat} is then given by

$$q_{sat} = f\, n_e\, K_B\, T_e \left(\frac{k_B T}{m_e}\right)^{1/2} \qquad 1.7$$

where the parameter f is known as the flux limit.

A number of experiments have been performed(1.23,1.24) which suggest a flux limit of only 0.03 but these were conducted in planar geometry where lateral transport effects are significant(1.21). Recent work has suggested a value of 0.08(1.25,1.26) in better agreement with two independent theories(1.27,1.28).

1.6.2 Fast electron transport

Suprathermal or fast electrons are produced with temperatures typically over 10 keV(1.29) by wavebreaking during resonance absorption(1.8,1.29) and can deposit their energy at high density. This process is undesirable as fast electrons will preheat the target ahead of the shockfront increasing the temperature of the cold material. In spherical compression experiments the entropy of the target will be increased degrading the final compression. Much work has been performed on the hot electron temperature T_H and range λ_L(1.30,1.31).

The scaling of fast electron temperature has been found empirically as[1.32]

$$kT_H \propto (I\lambda^2)0.39 \qquad 1.8$$

Fast electron preheating effects are important at high laser wavelength and irradiances i.e. when $I\lambda^2 \geqslant 10^{14}$ Wcm^{-2} μm^2.

1.6.3 Radiation transport

Transfer of energy by X-ray radiation can be an important factor in laser irradiated targets. Preheating of the target by radiation from the ablation region can be inferred from measurement of the soft X-ray spectrum emitted by the ablation plasma[1.33]. Recent work[1.34] suggests that radiation effects are a dominant mechanism in the heating of the rear surface of laser irradiated targets.

1.7 Thermal smoothing

Inhomogeneities in the laser beam profile give rise to spatial non-uniformities in pressure on the ablation front. These in turn produce non-planarity in the shockfront[1.35] and in spherical geometry, given degraded compression. If a sufficiently large absorption-ablation front separation can be achieved, thermal diffusion can smooth out the beam maxima and minima. Recent work, described in Chapters 5 and 6 suggest previous smoothing measurement[1.36] may have overestimated the

effect of this mechanism due to anomalous contributions from hydrodynamic effects. The wavelength and irradiance scaling from the results presented in this thesis suggest a tentative relation of

$$\frac{1}{\Delta} \propto I_a^{0.6} \lambda_L^{0.8-1.4}$$

where $1/\Delta$ is the degree of smoothing and λ_L and I_a is the laser wavelength and absorbed irradiance respectively.

1.8 Shock waves

At the beginning of laser irradiation shockwaves are driven into the solid target material, as the laser pulse power rises shocks of greater strength overtake the preceding ones to form a propagation shockfront or compression wave(1.12). The temporal profile of the laser pulse governs the shock dynamics and in an I.C.F. scheme the spherically converging shockwaves coalesce at the time of peak compression(1.37).

Useful relationships can be derived to relate the properties of material behind or in front of a propagating shockwave. In Fig.1.2 a disturbance corresponding to the shockfront is propagated with a velocity V_s into an undisturbed state defined by pressure P_o, density ρ_o $(=1/V_o)$ and mass velocity zero. The shockfront is assumed to consist of a time-independent pressure profile.

The pressure, density and mass velocity behind the front

are denoted by P_1, ρ_1 , and V_p respectively.

By the conservation of mass, the mass flux in and out of the shockfront must be equal,

$$\rho_o V_s = \rho_1 (V_s - V_p) \qquad 1.9$$

Similarly, by conservation of momentum, the time rate of change of momentum for the material between x = A and x = B is the mass flux $\rho_o V_s$ multiplied by the associated change in velocity V_p. The net force on unit cross section of the material is $P_1 - P_o$.

$$P_1 - P_o = \rho_o V_s V_p \qquad 1.10$$

From the conservation of energy, the power input to a unit cross section of material A and B, $P_1 V_{p1}$ must equal the time rate of change of energy for the enclosed material i.e.

$$P_1 V_p = \rho_o V_s \left(\frac{V_p^2}{2}\right) + \rho_o V_s (E - E_o) \qquad 1.11$$

where E_o and E_1 are the specific internal energies ahead and behind the shock. This may also be expressed using equation 1.9

as

$$E - E_o = \frac{P_1 V_p}{{}_o V_s} - \frac{V_p^2}{2} = \frac{1}{2} V_p^2 \qquad 1.12$$

These equations can be combined to form the equation

$$E_1 - E_o = \frac{1}{2} (P_1 + P_o)(V_o - V_1) \qquad 1.13$$

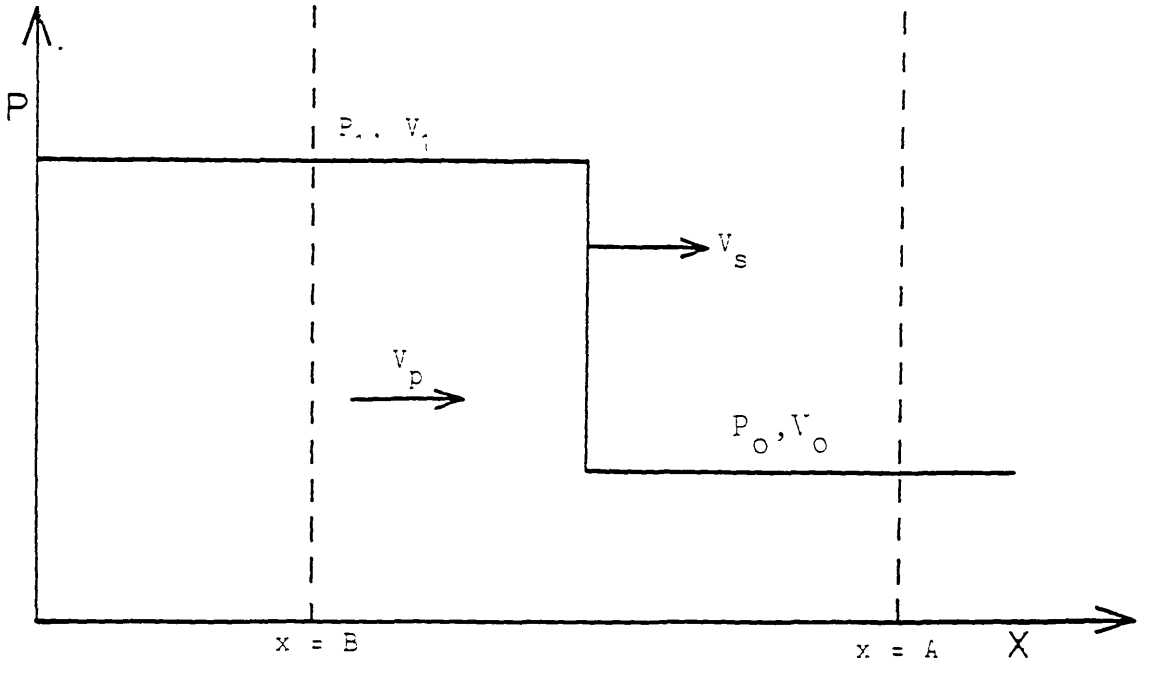

Fig.1.2 A schematic illustration of a shockwave pressure profile.

These equations were first derived by Rankine and Hugoniot[1.38-1.40] and represent the locus of all P_1, V_1 states attainable by propagating a shockwave into a fixed initial state P_o, Vo. This locus is often termed the shock Hugoniot curve.

1.8.1 Shock launch time

Particular problems arise when an attempt is made to measure the shock velocity using the time taken for the shock to emerge from the rear of a planar target. If the rise time of the laser pulse is very short the time at which the shockfront is launched into the material is well defined and an unambiguous measurement is possible. As shown in Fig.1.3 however, if the laser pulse has a slow rise time (e.g. as in a gaussian or trapezoidal pulse) ambiguities arise in the definition of the shock launch time. This problem can be avoided by using a stepped target and measuring the delay in shock propagation at a time when the shock is travelling at a constant velocity. The accuracy in defining the time at which the shockfront can be considered to be launched is heavily dependent on laser irradiance and target conditions. Midway between the first half of the rising edge of the laser pulse has been suggested by some workers[1.41,1.42], and this can provide a useful basis for approximation in experimental studies.

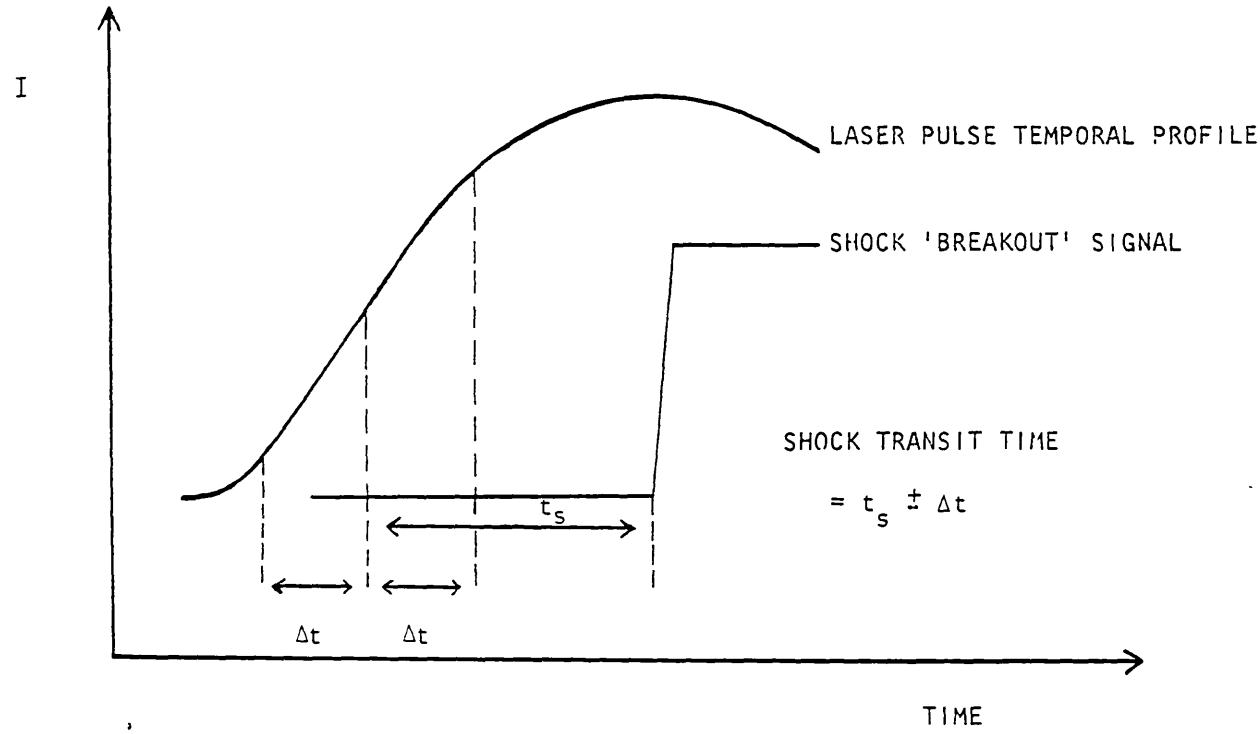

Fig.1.3 A schematic diagram illustrating the uncertainty introduced in the time of shockwave launch for a laser pulse profile with a slow rising edge.

CHAPTER TWO

MEASUREMENTS OF LASER INDUCED SHOCK PRESSURE AT 0.53 μm AND 0.35 μm

2.1 Abstract

Stepped and planar aluminium foil targets have been irradiated with single beams of 0.53 μm and 0.35 μm laser radiation. Optical streak photography has detected well defined stepped emission profiles as the shockfront emerges from the rear of the target with no evidence of precursor emission. Average shock velocities in the range $(2.3 - 5.5) \pm 0.8 \times 10^6$ cm s^{-1} have been measured. This data provides the first systematic measurement of shockwave pressure over a laser irradiance of $3.9 \times 10^{13} - 3.0 \times 10^{14}$ Wcm^{-2}. Pressures, up to 50 MBAR, inferred from E.O.S data for Aluminium, are in good agreement with 1-d hydrocode simulations(2.1) and values obtained from mass ablation rate measurements(2.2).

2.2 Introduction

The measurement of laser ablation pressure with wavelength and irradiance has been studied by foil acceleration measurements(2.3,2.4), mass ablation rates(2.2,2.5-2.7), and sporadically by both stepped and planar shock transit measurements(2.8-2.12). This chapter describes a systematic

study using stepped shock transit measurements over a range of irradiances at 0.53 μm and 0.35 μm.

It is well appreciated that stepped shockwave breakout provides a more reliable measurement of shockwave velocity (and hence drive pressure) than the total transit time through a planar target, the latter approach being complicated by shock acceleration phases(2.13) and laser pulse risetime effects (section 1.8.1). Accurate measurement of the laser induced shock pressure relies principally on three conditions being achieved. These are : that a constant pressure drives the shock steadily during transit through the target, the trajectory is one-dimensional such that significant lateral expansion of the shockfront during transit does not occur, and that the target material encountered by the shock is not significantly preheated above its cold state. In these experiments emphasis has been placed on fulfilling these conditions together with the achievement of well defined stepped emission profiles providing an unambiguous measurement.

Precise calibration is necessary to allow accurate measurements with the optical streak camera used in this and other experiments described in the following chapters. Both the temporal and spectral calibration of this diagnostic have been undertaken and this is fully described in Appendix A.

2.3 Experimental

A single beam of the VULCAN Nd glass laser system was frequency doubled and tripled to produce pulses of either 0.53 μm radiation 900 psec FWHM duration or 0.35 μm radiation 500

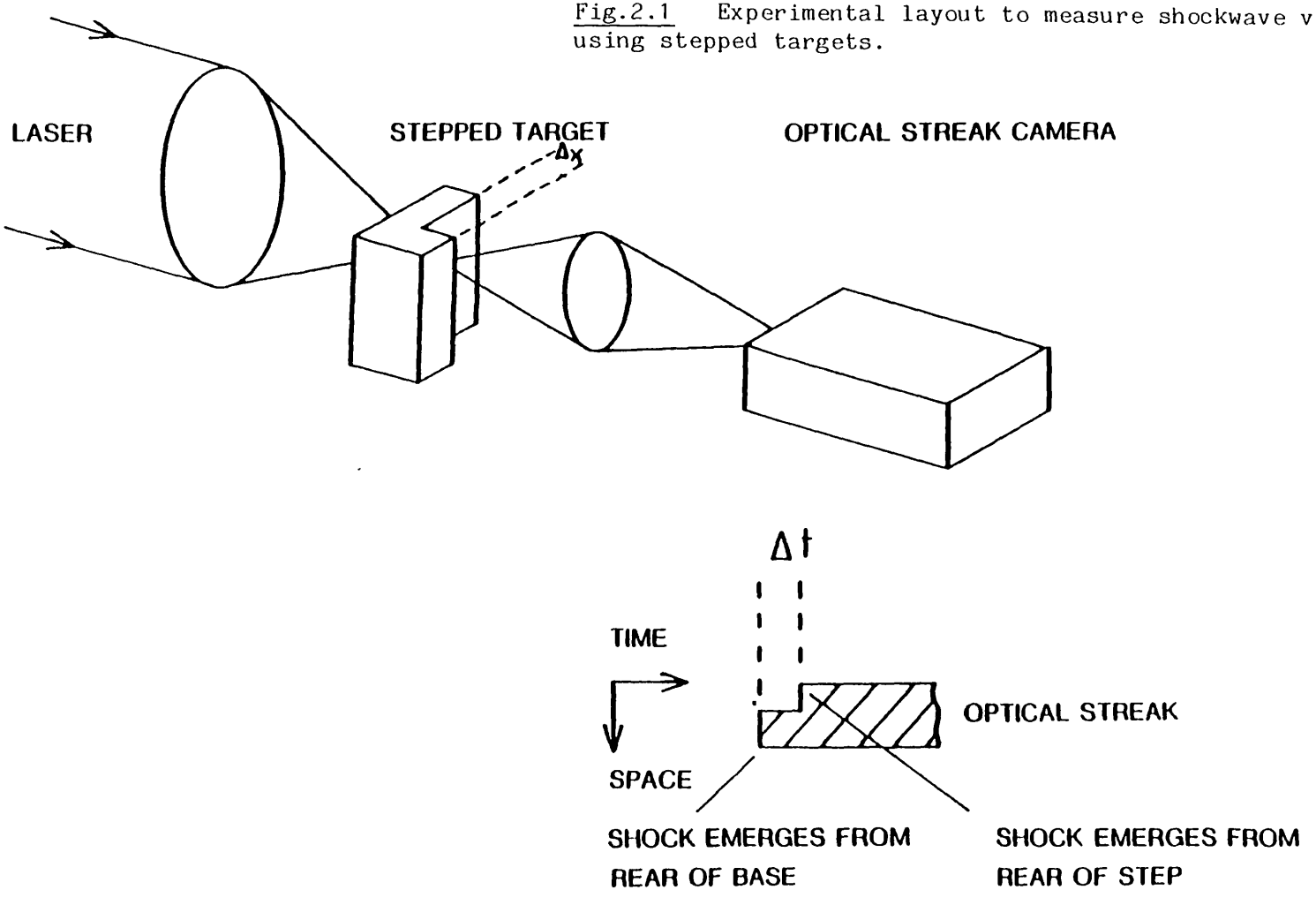

Fig.2.1 Experimental layout to measure shockwave velocity using stepped targets.

psec FWHM duration. The laser irradiance was varied in the range $3.9 \times 10^{13} - 3.0 \times 10^{14}$ Wcm^{-2} by varying the incident laser energy with a constant focal spot size. An f1.5 aspheric doublet was used to focus the 10 cm diameter beam to a focal spot size of 150 μm onto aluminium targets. The spot diameter was chosen to be compatible within limits of minimal shock non-planarity due to 2-d effects(2.1,2.14) yet also allowing access to a moderately high laser irradiance region. The foil targets, of the order of cm in lateral extent (to prevent anomalous energy transport around the targets), were both planar and stepped and typically consisted of a 12 μm base with a 6 μm step. The accurate step profile was prepared using a photomasking technique, typical samples examined under an S.E.M confirmed target dimensions to ± 0.1 μm accuracy. The arrival of the shockfront at the rear of the targets is signalled by the prompt heating of the rear surface of the target. The average shockwave velocity can be calculated from the delay in onset of the thermal emission between the arrival at the target base and step. Fig.2.1 shows a schematic layout of the experiment. The targets were aligned using a CW beam axis reference together with a rear surface illumination system to locate the step image onto the 100 μm wide streak camera slit orientated transversely to the step plane. The imaging system consisted of a 25 mm microscope objective relayed to a 38 cm achromatic camera lens to give an overall magnification of 25 onto the Hadlands 675 IMACON streak camera fitted with an S20 photocathode. This gave nominal temporal and spatial resolution of 10 psec and 10 μm respectively. A small fraction of the incident beam was relayed

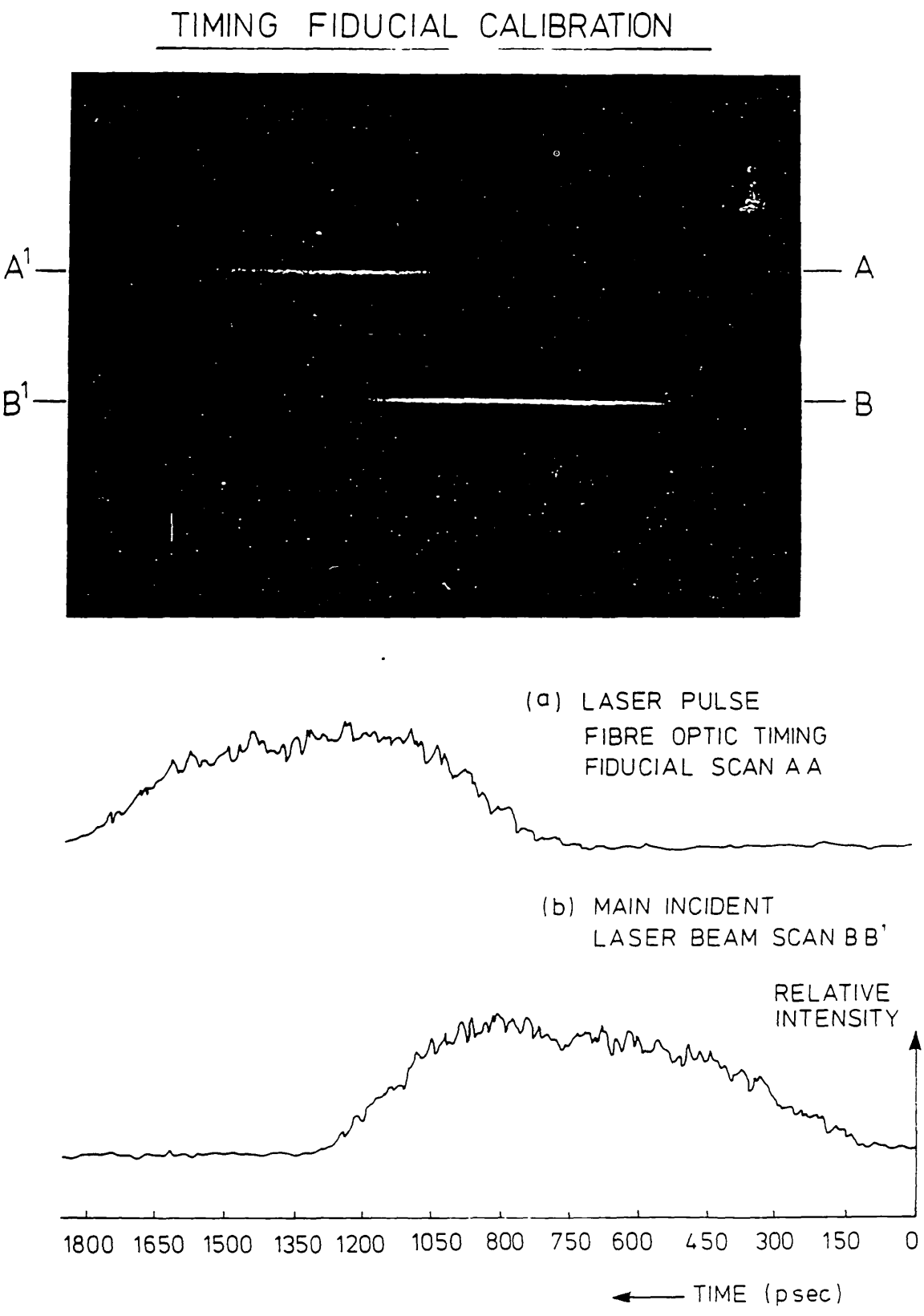

Fig.2.2 An optical streak photograph and microdensitometer tracing showing the calibration of the laser beam timing fiducial.

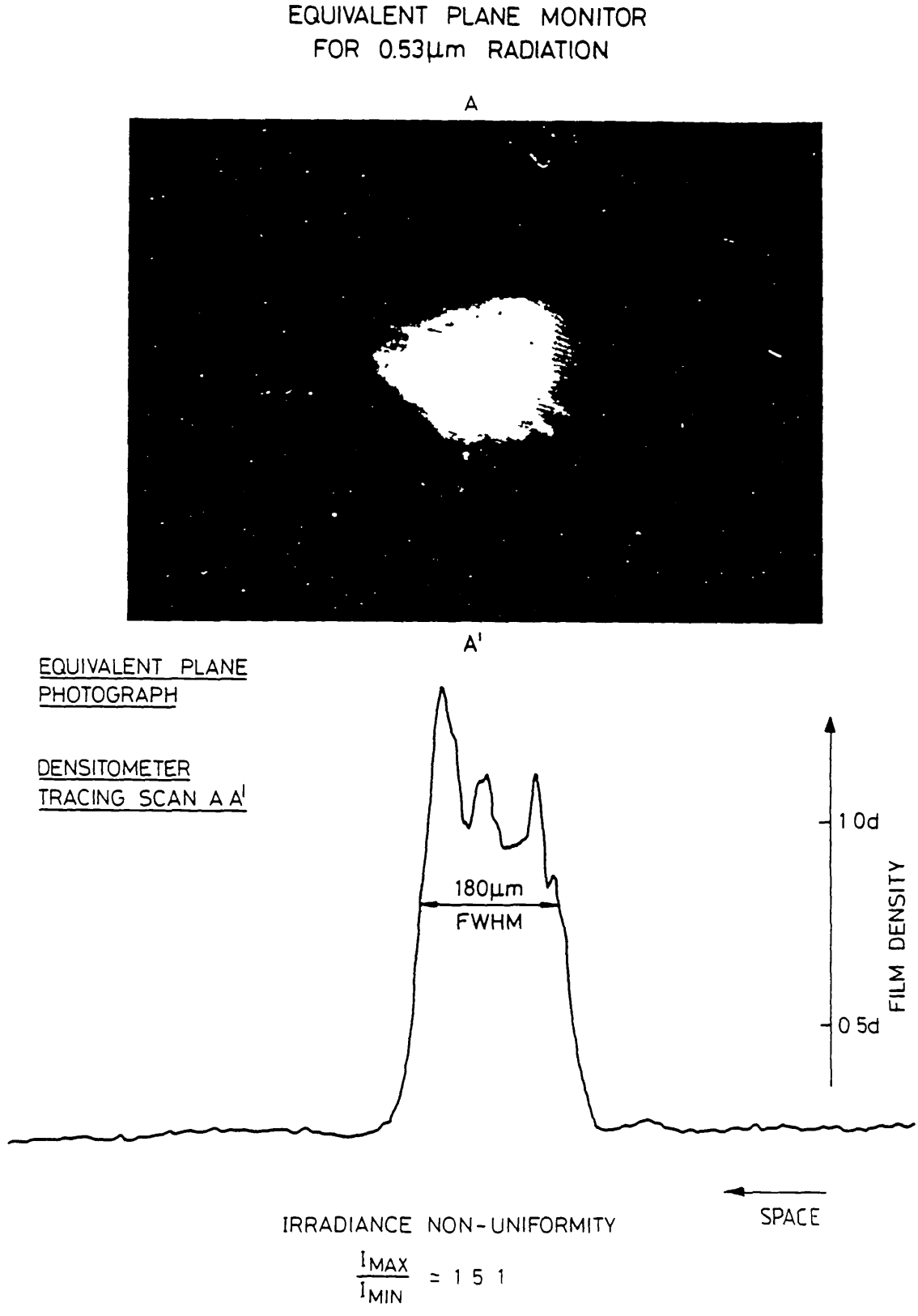

Fig.2.3 An equivalent plane photograph and microdensitometer tracing showing the laser beam profile non-uniformity.

via a separate optical path onto the camera slit to provide a timing fiducial mark.

A timing fiducial calibration was obtained using a low level (mJ) energy shot through the target chamber and empirical adjustment of the relative optical path lengths. Fig.2.2 shows an example with microdensitometer tracings of the main and timing fiducial beams. The laser beam intensity profile was monitored by relaying a fraction of the incident beam through an f50 relay lens onto type 56 Polaroid pos/neg film. A typical photograph and microdensitometer tracing is shown in Fig.2.3.

2.4 Results

An optical streak photograph from the rear of a stepped target is shown in Fig.2.4. Also shown are microdensitometer tracings through the timing fiducial (a), shock breakout from the target base(b), and shock breakout from the target step (c).

The risetime of the shock signal is $\sim$ 50 psec which would infer a shockfront thickness of $\sim$ 1.5 μm. Such a value is in sharp contrast with the idealised single shock thickness of a few molecular mean free paths[2.15]. This effect may be attributed to the distinction between a classical single shockwave and the laser generated shockfront, the dynamics of which have been studied by some authors[2.13]. These simulations predict that a multiple shock or compression wave is propagated into laser irradiated targets and consists of frontal shock portion and a rear 'pile-up' zone with no distinct boundary between them. No data was presented for 0.53 μm radiation but with similar laser conditions at 1.06 μm the

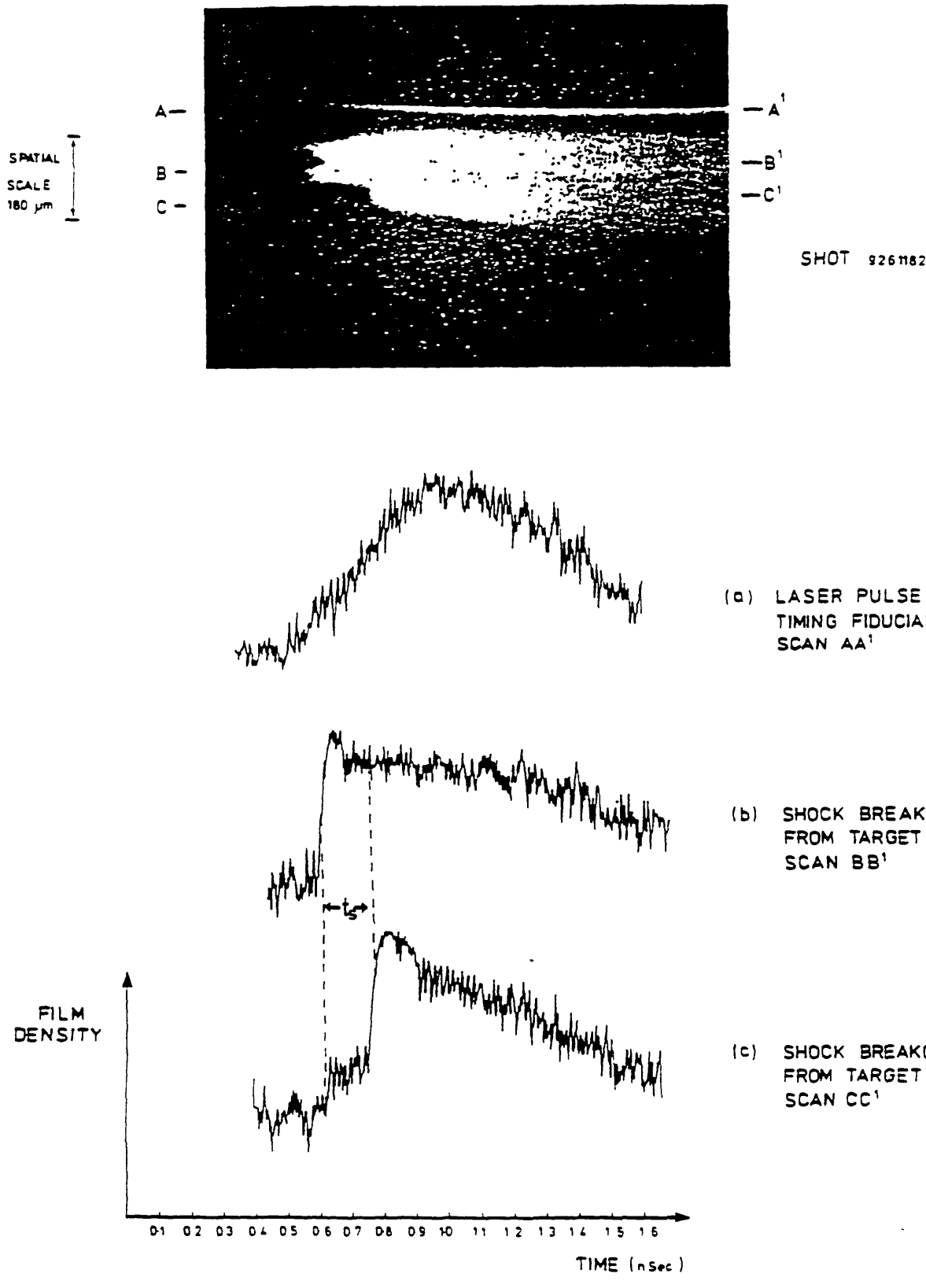

Fig.2.4 Optical streak photograph of a stepped aluminium target with microdensitometer tracings through (a) timing fiducial (b) shock emission from the target base and (c) shock emission from the target step.

thickness of the multi shock front was calculated to be $\sim$ 1-2 μm. Such a figure would be consistent with the signal risetimes recorded here. Some additional temporal broadening may be caused by preheating effects, although no evidence of significant precursor emission is apparent. There is little evidence of significant lateral spreading of the shockfront as it transits the step. The optical streak image sizes are consistent with a high temperature focal spot size of 150 μm, spreading slightly to 160 μm at the end of the laser pulse.

In the example shown some non-uniformity in the shock 'breakout' profile is apparent. This is attributed to gross non-uniformities in the incident laser beam profile. The equivalent plane record for this shot showed particularly severe inhomogeneities, with intensity maxima and minima as high as $I_{max}/I_{min} \approx 4:1$, Such gross non-uniformities corresponded to shots recorded after the laser system had been fired at maximum repetition rate over an extended period, preventing the laser disc amplifiers from cooling sufficiently and delivering severely degraded beam quality.

Simulations on the effect of laser beam non-uniformity have been performed by some workers(2.1). A figure of $\sim$ 25% non-uniformity has been calculated for a 2% uniformity in the shockfront. The worst case transit time non-uniformity recorded here was $\sim$ 5% for an $I_{max}/I_{min} \approx 4:1$.

The stepped target emission profiles recorded are particularly well-defined permitting an accurate measurement of the shockwave velocity over the step. The very low level precursor emission ahead of the main shock breakout infers

TABLE 2.1

0.53 μm DATA

Shot no.	Target (μm)	Base Transit Time (psec)	Step Transit Time (psec)	Shockwave Velocity ($\mu m\ nsec^{-1}$)	Inferred Pressure (MBAR)	Absorbed Irradiance $x10^{13}$ (Wcm^{-2})
% Error	± 6%	± 9%	± 9%	± 18%	± 25%	± 25%
4191182	9+9	611	375	24.0	10.0	9.2
6191182	9+9	512	385	23.4	9.2	8.8
6231182	12.4+5.6	562	196	28.5	14.8	15.2
28231182	12.4+5.6	710	148	37.8	27.0	24.0
6251182	12.4+5.6	572	181	30.9	17.6	13.6
9261182	12.4+5.6	660	180	31.1	17.9	14.4
23251182	10.4+9.2	630	380	24.2	10.1	3.1
3261182	12.4+5.6	650	200	28.0	14.1	7.8
2430982	10.0 (planar)	400	-	-	-	8.0

0.35 μm DATA

815483	10.4+9	440	210	44.0	34.5	17.3
1719483	10.0+10.0	390	185	55.0	47.0	19.5
2826483	10.0+10.0	420	207	43.8	34.0	17.1

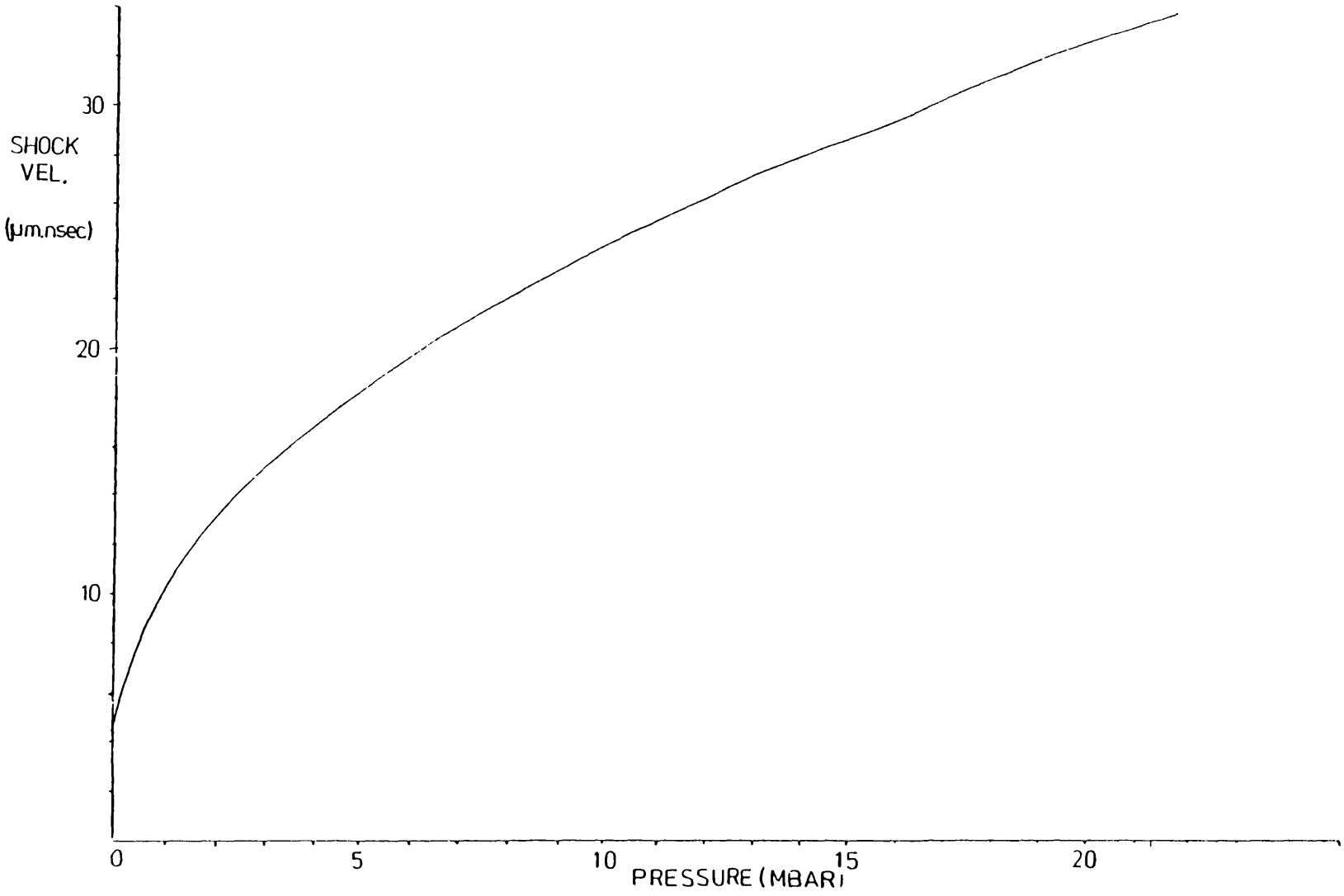

Fig.2.5 Shock Hugoniot for aluminium from ref.(2.18).

maximum levels of target preheating as less than 2%, assuming the rear surface emits as a 'blackbody'(2.16). This is consistent with low level target preheating due to fast electrons (which is dependent on $I\lambda^2$) at this wavelength and irradiance(2.17,2.18). However, based on recent results some evidence of radiative preheating with these target conditions might not be entirely unexpected(2.19).

Table 2.1 lists the target dimensions, shock transit times and laser parameters (absorption fractions as Key et al(2.2)). Average pressures in the targets are inferred from the measured shock velocities using shock Hugoniot data for aluminium(2.18), shown graphically in Fig.2.5. The base transit times have been measured relative to an arbitrarily defined position in the first half of the rising edge of the laser pulse (see section 1.8.1). Pressures inferred from these base transit times are 40% - 80% lower than those measured from the step times, even after accounting for some uncertainty in the shock launch time. This demonstrates the ambiguity introduced when trying to infer an induced shock pressure from a shock transit which is not steadily driven at constant velocity. Some workers(2.13) have predicted that the shock propagation does not achieve a constant velocity until a time $t \sim 0.8\ t_L$, where t_L equals the laser pulse duration. The measurements made here have been at times of $t \simeq 0.6\text{-}0.8\ t_L$ and on that basis would suggest the approximation of constant velocity here is reasonably good.

The values of pressure and laser irradiance are shown graphically in Fig.2.6 for both 0.53 μm and 0.35 μm laser

wavelengths. For the 0.53 μm data the following empirical relationship has been obtained from a least squares fit :

$$P\ [\text{MBAR}] = 3.1 \pm 0.7\ I_{abs}^{0.63\pm0.15}\ [10^{13}/\text{Wcm}^{-2}]$$

In Fig.2.6 two comparisons are made : (a) the mass ablation rate measurements of Key et al[2.2] (for the case of negligible lateral energy transport using a conventional averaged incident irradiance with a FWHM pulse duration),

$$P = 3.5\ I_{abs}^{0.68}\ [10^{13}/\text{Wcm}^{-2}]$$

and (b) 1-d hydrocode simulations, Thompson and Roberts[2.1] which included multi-frequency radiation transport, expressed in terms of averaged irradiance using conventional focal spot radius and FWHM laser pulse duration,

$$P = 3.4\ I_{abs}^{0.62}\ [10^{13}/\text{Wcm}^{-2}]$$

Also shown on the figure is data at 0.35 μm.

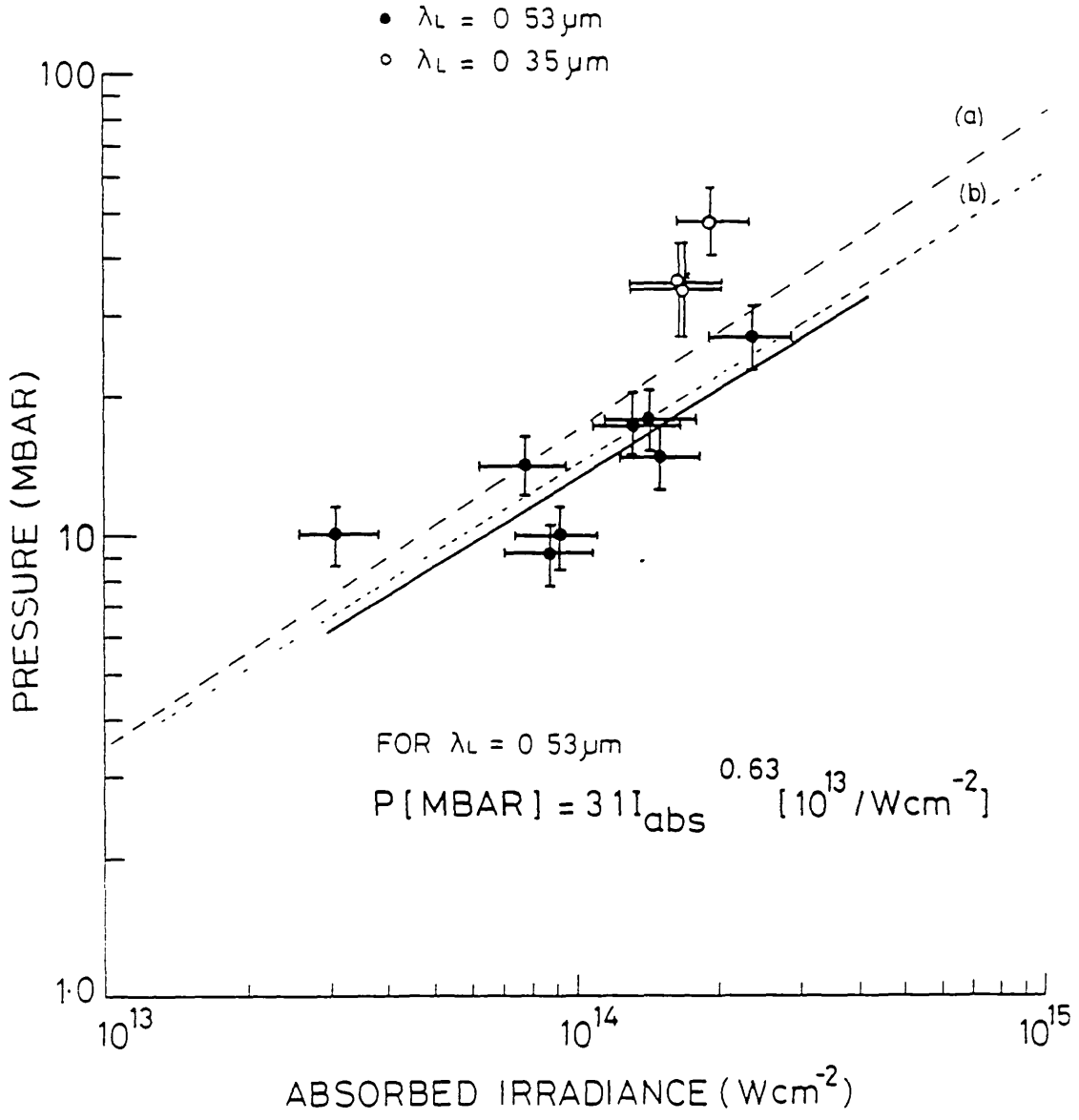

Fig.2.6 The variation in laser induced shock pressure inferred from measured shock velocity as a function of absorbed irradiance at 0.53 μm and 0.35 μm. The experimental data (——) is compared with (a) (---) mass ablation rate pressures from ref.(2.2) and (b) (...) 1-d hydrocode simulations from ref.(2.1).

2.5 Uncertainty in pressure measurements

To make a meaningful measurement of pressure accuracy levels of a few percent are necessary(2.14). The percentage errors quoted in Table 2.1 are worst case values and are likely to be considerably less in the majority of cases. The errors in laser irradiance are an estimate obtained from laser energy calorimeter, focal spot sizes and laser pulse duration. Significant improvements could be made by using larger step dimensions which would reduce the significance of target preparation non-uniformity. The longer transit times would also reduce the significance of the streak camera speed calibration uncertainty although careful choice of laser parameters would be necessary to avoid shockwave attenuation. Some evidence of slight attenuation is evident from the reduction in shock luminosity from the target step microdensitometer tracing.

2.6 Discussion

The scaling of pressure and laser irradiance for 0.53 μm radiance in Fig.2.6 is in good agreement with both the ablation rate derived values and the 1-d hydrocode simulations. The slightly lower values of pressure measured experimentally may be partly due to slight two-dimensional effects due to the size of the laser focal spot. Although simulations by Thompson and Roberts suggest that below irradiances of 5×10^{14} Wcm^{-2} and focal spot radii above 50 μm this effect is unlikely to be significant. As mentioned above shockwave attenuation may also be a contributing factor. In similar laser conditions a factor of approximately 10% has been suggested(2.20) to account for

this. If such a correction is valid for this data, even better agreement would be produced.

The 0.35 μm data demonstrates pressure enhancement due to reduced wavelength caused principally by two factors. Inverse Bremsstrahlung absorption is believed to be the dominant absorption mechanism at short wavelengths which leads to higher absorption factions(2.21). Also higher hydrodynamic efficiencies are expected since the laser energy is deposited at higher densities steepening the temperature gradient in the ablation front and increasing the ablation rate(2.22).

The values of pressure inferred from the 0.35 μm data are significantly higher than those reported recently from shock transit times(2.20) but are more in line with recently reported mass ablation rate derived pressures at 0.35 μm(2.23).

It is unfortunate that insufficient data was recorded to give an accurate scaling law for 0.35 μm data which would have enabled a more general relation between pressure, irradiance and wavelength to have been derived.

2.7 Conclusions

The first systematic experimental measurement of laser induced shock pressure over a wide region of laser irradiance at 0.53 μm has been obtained. The pressures obtained are in good broad agreement with 1-d hydrocode simulations(2.1) using multi-frequency radiation transport. Pressures derived from mass ablation rate measurements assuming negligible lateral energy transport(2.2) are also in agreement within the limits of experimental error.

Data obtained at 0.35 μm has demonstrated significant pressure enhancement although insufficient measurements were made to derive a pressure, irradiance and wavelength scaling relation.

A future study would be enhanced by simultaneous mass ablation rate measurements. This would then resolve a number of questions concerning the pressures measured at the ablation front in contrast to those inferred in the dense cold regions deep in the target.

CHAPTER THREE

THE OBSERVATION OF SHOCKWAVE TRANSIT THROUGH TRANSPARENT MULTILAYER FOIL TARGETS

3.1 Abstract

Multilayer targets consisting of layers of bismuth, mylar, Kcl and CH have been irradiated with 900 psec FWHM pulses of 0.53 μm radiation. The progress of the shockfront during irradiation has been monitored by the abrupt changes in shock heated thermal emission as it crosses the interface between materials of different acoustic impedance. Computer simulations using the 1-d hydrocode MEDUSA have predicted the time at which the shock front crosses the material boundaries and these correspond well with the abrupt changes in shock luminosity. The variation of shock luminosity is consistent with a recent theoretical study by some workers(3.1) who have predicted sharp increases in material compression and temperature at the interface of material boundaries with gross impedance mismatch.

3.2 Introduction

Much work has been performed using shock heated thermal emission to signal the emergence of the laser driven shockfront from the rear of foil targets(3.2-3.7). A disadvantage of this type of 'shock breakout' measurement is the inability to monitor

the progress and spatial shape of the shockfront during transit through the target.

Considerable potential could be envisaged in such a diagnostic measurement both intrinsically, in the study of the phases of shock dynamics and in the non-uniformity of the shockfront in 'thermal' smoothing studies and instability growth experiments.

The work contained in this chapter describes the observation of multiple phases of shock luminosity recorded from the rear of multilayer transparent foil targets. The occurrences of these jumps in shock luminosity are shown to correspond with the shockfront passing over the boundary between materials of different acoustic impedance.

The observation of shock emission from a single layer transparent foil has been reported (although on a ten nsec. timescale) for conditions when the material remained transparent(3.8) and in a separate experiment, after a short period of emission, was rendered opaque(3.9). The proposed mechanism for loss of transparency was temperature and pressure induced effects such as chemical breakdown, change to a semiconductor state, loss of optical inhomogeneity and phase change(3.10).

The temporal emission sequence observed in the results presented here has not, to the knowledge of the author, been reported previously and shows a number of interesting features worth thorough study. Some important aspects of laser driven shock propagation over target interfaces have been reported recently by Salzman et al (3.1,3.11). These computer

simulations predict sharp increases in material compression and temperature at the material interface as the shock crosses into a material of higher acoustic impedance. The laser driven 'shockfront' or compression wave is found to consist of two parts, a shock front zone in the first part of the wave and a rear pile-up zone. The width of this 'compression wave' is found to be of the order of microns and is in contrast to the idealised single shock thickness of a few molecular mean free paths(3.12). A number of features described in this work are in good qualitative agreement with the measurements presented in this chapter.

3.3 Shock propagation over a material interface

The Rankine-Hugoniot equations have been derived in section 1.8 to describe the state of energy, pressure, density, particle and shock velocity in front of and behind a shocked material. When a shockwave passes through a material the conservation of momentum relation (equation 1.10) and the shock velocity define a straight line in the plane of the pressure P and the particle velocity V_p with a slope of $\rho_o V_s$. This quantity $\rho_o V_s$ has been termed the 'impedance' and is different for each material and shock strength. When a shockwave reaches the interface between two materials a shock wave continues into the second material and simultaneously a backward moving wave is generated which reflects back into the first material.

This backward moving wave is either a rarefaction wave for the case of the impedance of the first material being greater than the second, or a shock wave for the second being

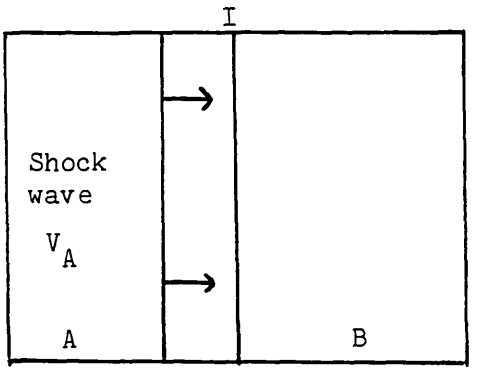

(a)

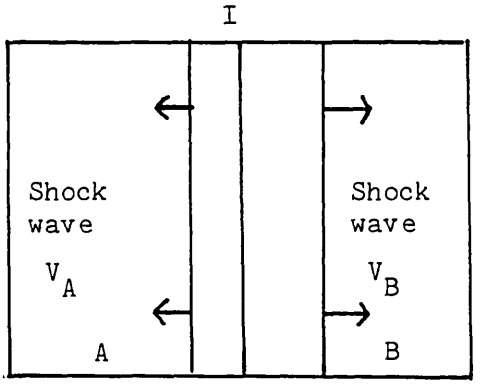

(b) $\rho_A V_A < \rho_B V_B$

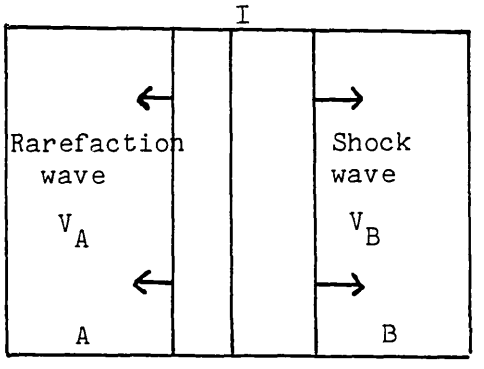

(c) $\rho_A V_A > \rho_B V_B$

Fig.3.1 Shock propagation from material A to material B over an interface I for (a) before shock hits the interface, after shock hits the interface; (b) impedance A < impedance B; and (c) impedance A > impedance B.

greater than the first. Also as this happens the pressure and particle velocity are changed so that both quantities are continuous across the interface. This multiple wave generation at a target boundary is demonstrated schematically in Fig.3.1. Many experiments have been performed (3.13-3.17) utilising these impedance match conditions to determine Hugoniot data for unknown materials by propagating a shock through a 'standard' material and then into an adjacent sample of the material under study.

3.4 Experimental

The experimental arrangement was similar to Chapter 2 as is shown in Fig.3.4 with a single beam of 0.53 μm laser radiation (900 psec FWHM) irradiating the multilayer targets. The focal spot size was $\sim$ 50 μm and the targets were prepared by vacuum depositing layers of bismuth, Kcl and CH onto mylar substrates. The bismuth coatings were $\sim$ 1.0 μm thick while the other materials varied in the range 5 - 25 μm. A timing fiducial and equivalent plane monitoring of the laser beam profile were identical to those described in the previous chapter. The optical streak photographs recording the emission from the multilayer targets suffered from gross over-exposure of the camera recording film (Ilford HP5). The intensity variation from the data was therefore not of great accuracy. Computer digitization and colour enhancement of the images was necessary to reveal the image profiles.

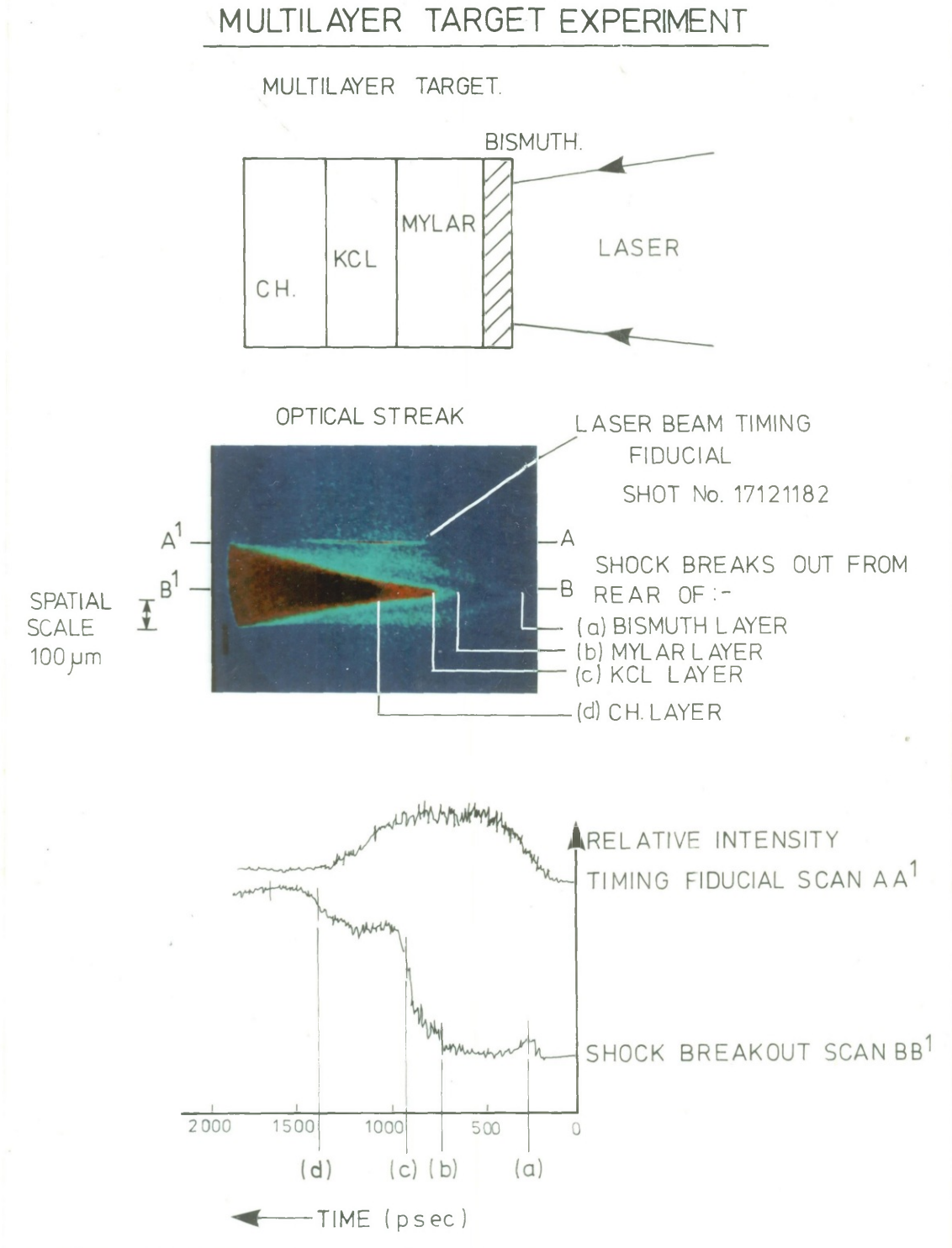

Fig.3.2 A composite figure showing a multi-layer target (relative layer dimensions not accurate), a colour enhanced optical streak record and microdensitometer tracings through the shock breakout revealing abrupt changes in shock luminosity.

3.5 Results

A composite diagram of a typical multilayer target and its constituent layers is shown in Fig.3.2, together with the corresponding optical streak photograph for this target. The black and white film negative has been digitised and different colours assigned to different levels of film density to enable the phases of shock emission to be more clearly distinguished. Microdensitometer tracings of the timing fiducial and rear surface emission are shown indicating the boundaries of the emission phases.

Fig.3.3 shows a selection of four examples of multilayer target emission. (a) is the image shown in Fig.3.2 (shot no.17121182), (b) is an example of a four layer target with a rear surface coating of 0.3 μm of bismuth (shot no.19121182), (c) is a four layer target with similar dimensions to (a) (shot no.15151182), and (d) is a two layer target with a 25 μm second layer (shot no.31111182). The temporal and spatial scales are common to all four images and can be estimated from 3.3(a). Table 3.1 shows the target dimensions for each shot, including transit times measured from the changes in intensity level and laser irradiances.

The results presented in Figs.3.2 and 3.3 show a complex temporal and spatial emission sequence which can be described by a series of changes in shock luminosity as the laser driven shockfront crosses the interface of each of the layer boundaries.

To establish that the emission phases did originate from within the target an opaque layer of $\sim$ 0.3 μm of bismith was

TABLE 3.1

MULTILAYER TARGETS

Shot no.	Absorbed irradiance $\times 10^{14}$ (Wcm^{-2})	Mylar layer		Kcl layer		CH layer	
		Layer Thickness (μm)	Transit Time (psec).	Layer Thickness (μm)	Transit Time (psec)	Layer Thickness (μm)	Transit Time (psec)
24111182	6.5	10	265	5	340	5	450
27111182	1.8	10	600	5	300	5	200
31111182	4.1	25	750	-	-	-	-
11121182	3.8	25	1200	5	150	-	-
13121182	3.2	10	825	5	170	-	-
17121182	3.5	10	520	5	200	5	470
1921182	1.7	10	-	5	-	5 + 300 nm bis.	1300
15151182	4.3	10	600	5	160	5	500

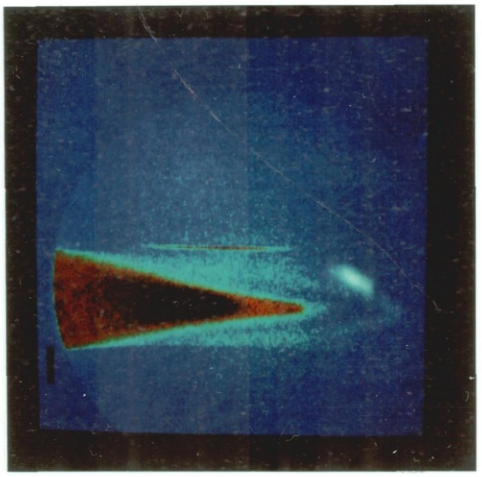

(a)

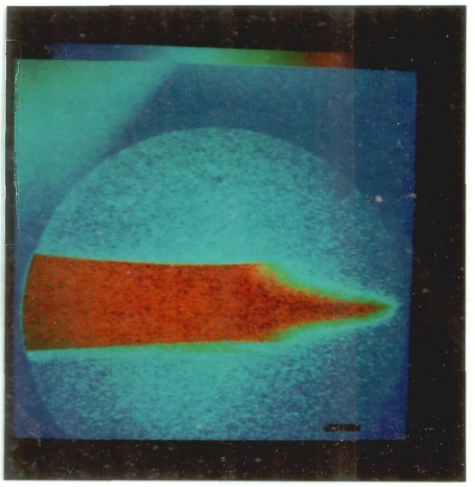

(b)

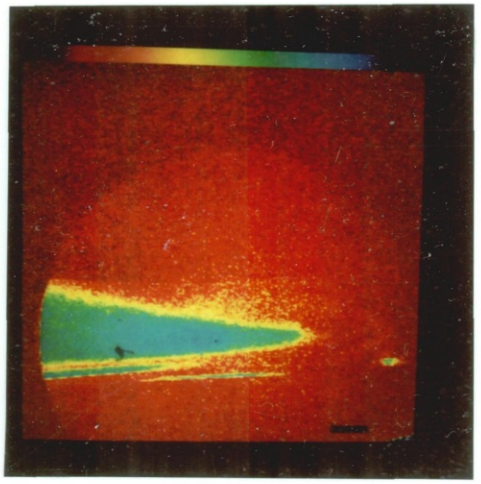

(c)

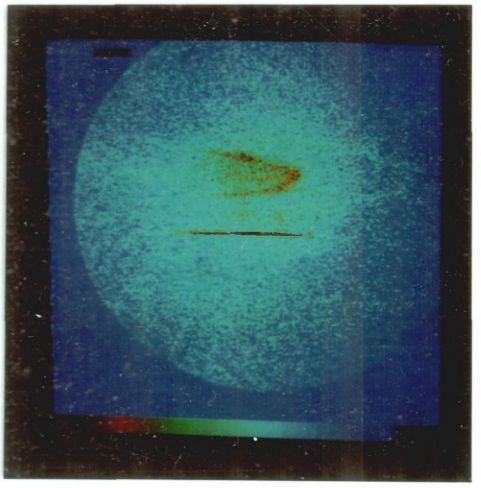

(d)

Fig.3.3 A selection of colour enhanced optical streak records for the case of (a) a four layer target, (b) a four layer target with an opaque layer on the target rear surface, (c) another example of a four layer target, and (d) a two layer target.

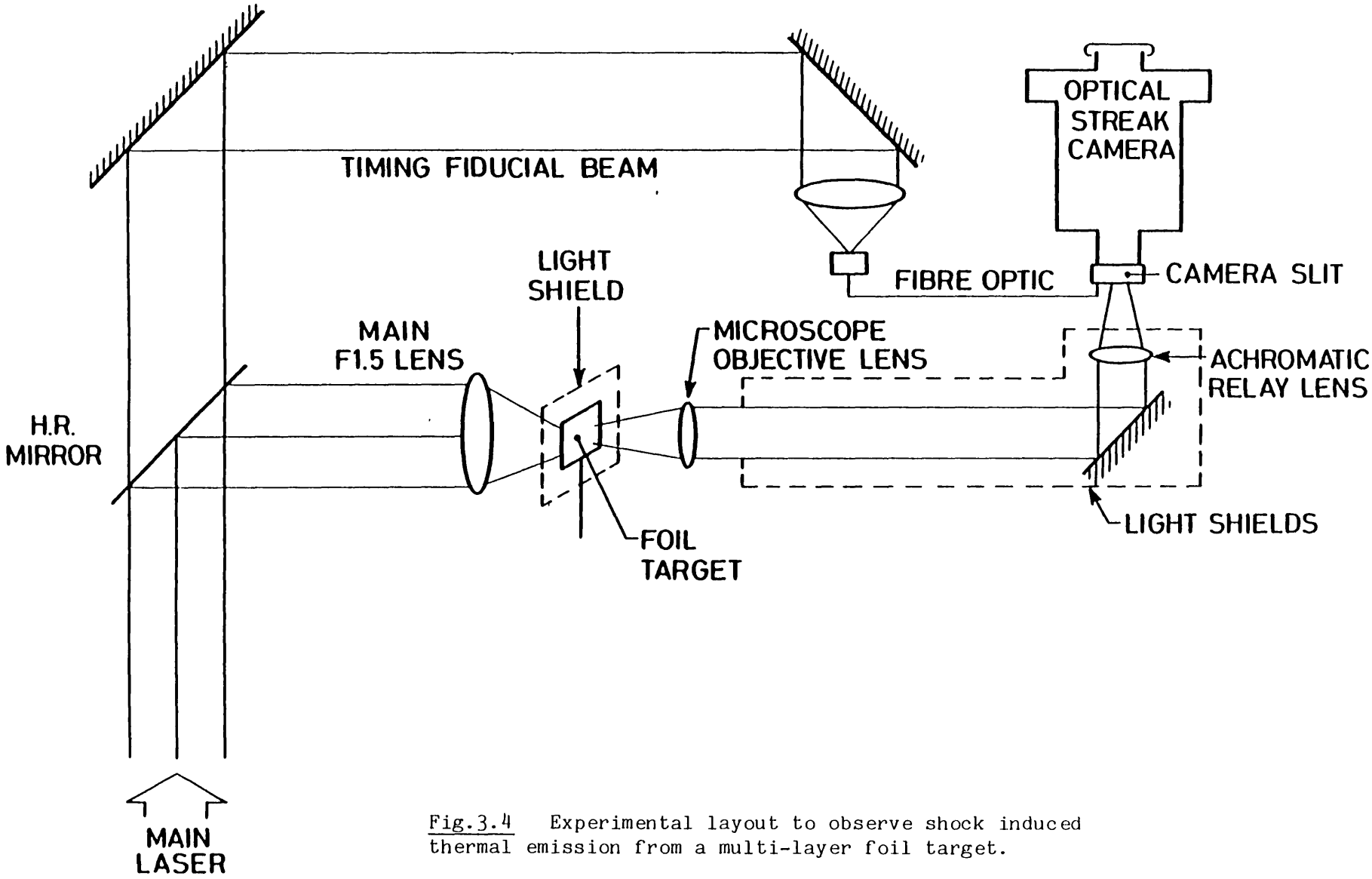

Fig.3.4 Experimental layout to observe shock induced thermal emission from a multi-layer foil target.

deposited on the rear of a multilayer foil. The optical streak record is shown in Fig.3.3(b) and shows a single emission phase occurring late in time, consistent with the time of the final phase of emission from an uncoated multilayer foil.

Further empirical evidence is shown in Fig.3.3(d) where a two layer target shows only a dual phase emission sequence. The increased delay time between the first and second phase is consistent with the increased second layer target thickness.

3.5.1 Emission phases in the multilayer foil

The phases of emission can now be considered in detail with reference to a typical multilayer streak record as shown in Fig.3.2. Three basic factors are likely to control the intensity of emission detected by the streak camera through the foil target. These are :

(1) The strength of the laser generated shock waves, which will be dependent on the temporal profile of the laser pulse.

(2) The degree and type of impedance mismatch between each of the material layers

(3) The opacity and thickness of each layer remaining between the propagating shockfront and the rear of the target.

At the beginning of irradiation no emission is observed until ($\sim$ 50 psec) the shockfront emerges from the bismuth and passes into the mylar layer (Fig.3.2a). A short period of

emission occurs which quickly reduces to a level below the sensitivity of the streak camera. This is consistent with only a faintly luminous shockfront at a time when the laser pulse is still on its rising edge, the remaining layers of material which would further attenuate emission and perhaps most importantly the impedance mismatch of the bismuth-mylar interface. The shock will be crossing from a high to a low impedance material (ρ_0 of bismuth = 9.3 g cm^{-3} c.f. ρ_0 mylar = 1.3 g cm^{-3}) and the back reflective wave will be a rarefaction wave and no sharp rise in compression and temperature would be produced (as demonstrated by Salzman et al[3.1]). There is also likely to be significant X-ray radiative heating from the high z bismuth plasma[3.18] depositing energy in the mylar layer increasing its opacity. The shock continues to propagate through the mylar until it reaches the mylar-Kcl interface. Here emission is abruptly detected as the shock encounters a low impedance-high impedance interface (ρ_0 Kcl = 1.9 g cm^{-3}) and a sharp increase in compression and temperature is caused as the back reflected wave is a shockwave and collides with the 'pile-up' zone of the laser generated compression wave, again consistent with simulations of Salzman et al.

The shockfront continues through the Kcl layer emitting strongly until it reaches the Kcl-CH interface. Here an abrupt increase in emission is observed in the streak record which is greater than might have been expected simply on the basis of the degree of impedance mismatch (ρ_0 for CH = 1.2 g cm^{-3}). For a high to a low impedance interface transition no sharp rise in compression and temperature might be expected. This could be

explained on the basis of the opacity of Kcl being significantly higher and the timing of the transition corresponding to approximately the peak of the laser pulse. The shockfront continues through the plastic layer until it breaks out at the rear of the target into vacuum producing another increase in emission. This temporal emission sequence is repeated in all of the multilayer targets, but due to the film saturation a quantitative comparison is not possible.

3.5.2 Annular ring emission feature

Another interesting feature apparent in the streak records is the annular ring type structure seen early in time in Fig.3.2 and Fig.3.3(c) and also visible later in time in Fig.3.3(d). This type of annular emission structure has been reported by a number of workers[3.19] from opaque targets and has been attributed to an edge rarefaction wave obscuring the rear surface emission as the shock unloads from the free surface[3.12]. Such an explanation would not be valid here since in the case of the early time feature, shockwave unloading is not occurring but would still be valid for the late time annular feature in Fig.3.3(d). An explanation of both features may be the temporal width of the multiple shock or compression wave which is driven by the laser. The persistence time of the sharp temperature rise at the material interface has been predicted to be dependent on the compression wave thickness. The temporal width features are $\sim$ 50 psec and 100 psec for the early and late time features respectively. This would imply (assuming a shock speed $\sim$ 20 μm nsec^{-1}) a thickness of 1 - 2 μm in

reasonable broad agreement with the results of Salzman. Such a mechanism would explain the absence of an annular ring structure in the emission from a propagating shockfront not encountering an interface.

3.5.3 Lateral spreading of the shockfront

Another distinguishable feature in the streak records is the lateral expansion of the region of emission as a function of time. This expansion is repeated at each of the phases of emission at a velocity of the order of $V_{exp} \sim 20$ μm nsec. No significant differences can be seen in the expansion rate between each of the phases of emission in a single shot. However a reduced rate of emission is discernible in Fig.3.3(d) where a larger focal spot size of ~ 90 μm (c.f. 50 μm) was used. This would be consistent with a model of a gross non-planar spherically expanding shockfront caused by a very small focal spot and a low f number lens focussing the laser beam onto the target. Such effects have been predicted and observed by a number of authors(3.20,321).

It may be argued that energy deposition and expansion of the focal spot area as observed by some workers(3.22) due to a number of effects such as fast electrons and lateral thermal transport would produce expansion of the laser induced shockfront. However if this were the cause there would only be a single expansion of the shockfront and not would not be repetitive for each layer of the target present.

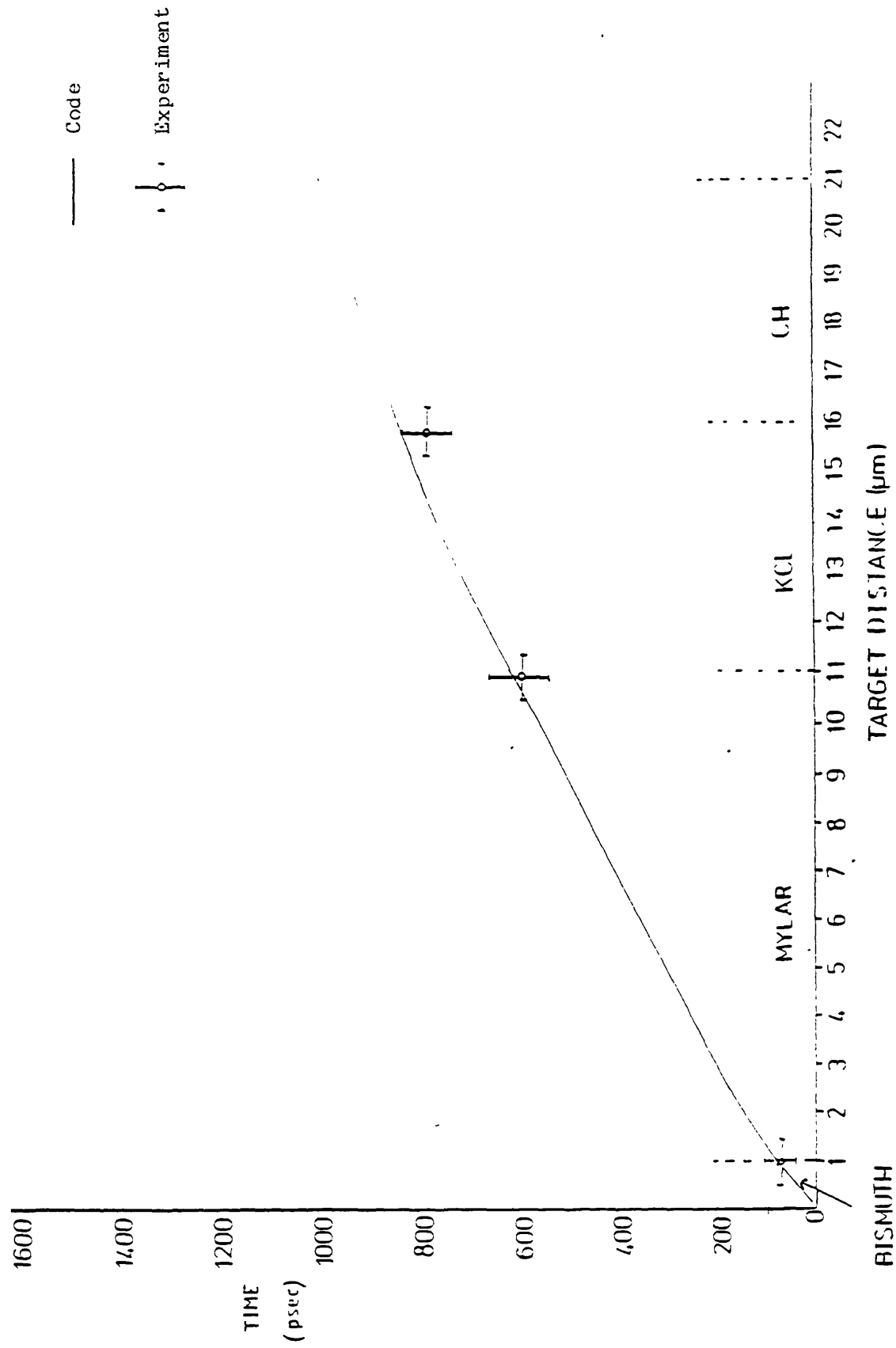

Fig.3.5 A computer simulation using the 1-d hydrocode MEDUSA of the position of the shockfront in a laser irradiated multi-layer target and the experimental occurrences in change of shock luminosity as it crosses the layer boundaries.

3.6 Comparison with code simulations

Computer simulations using the 1-d hydrocode MEDUSA were used to predict the position of the shockfront during irradiation in a multilayer target as used in the experiment. To establish initially that such a code prediction would be realistic, a comparison simulation was performed using a stepped aluminium target with dimensions and laser conditions identical to those used in Chapter Two.

The results of this simulation predicted the time of emergence of the shockfront at the base and step of the target used to be within 2% of the values measured experimentally. This demonstrated that the code could predict accurate shock transit times and a further simulation was performed using a multilayer target with dimensions of 1.0 μm bismuth, 10 μm mylar, 5 μm Kcl, 5 μm CH and a focal spot of 50 μm at an irradiance of 4.4×10^{14} Wcm^{-2} identical to the conditions in shot no.17121182 (i.e. Fig.3.2). The result of the code simulation is shown in Fig.3.5 together with the experimentally inferred positions of the shockfront measured from the changes in shock luminosity.

As can be seen good agreement is found between the code predictions and the experimental values except for the transit time in the CH layer. This could be explained simply on the basis of a greater thickness of CH layer than was intended during target preparation. As will be discussed later the target design, both of material and dimensions, were not able to be varied at will due to a separate experiment being performed in parallel by other workers. There is some considerable likelihood that the CH layers were greater than the figure of 5

TABLE 3.2

	Transit time (psec)		
	Mylar layer	Kcl layer	CH layer
Code	540	240	190
Experiment Shot No.17121182	520 ± 50	200 ± 20	470 ± 50

μm nominated. Microscopic analysis of a selection of the targets not irradiated revealed some deviation in CH layer up to 10 μm. This would be consistent with the transit times recorded which infer anomalously low values of shock velocities for some cases. Table 6.2 compares the transit times as predicted by the code and the experiment.

These simple simulations provide evidence that the times at which the changes in shock luminosity have been observed correspond well with the time at which the shockfront would be expected to cross the material layer interface.

3.7 Conclusions

The results described in this chapter have demonstrated the ability to monitor the progress of laser driven shockfronts in transparent multilayer targets. Abrupt changes in material luminosity caused by the shockfront passing over the interface between materials of gross impedance mismatch diagnose the phases of shock transit in the target.

The experiment has not unfortunately been performed in ideal conditions and what emerges is an interesting but only qualitative study of shock propagation over material boundaries. The results merit a thorough quantitative study with an experiment in which a systematic investigation can be made, beginning with a simple two layer target scheme and using larger focal spot sizes ($\sim$ 200 μm) eliminating the complications of lateral expansion of the shockfront. Also the target materials should not involve high z materials which can produce radiative preheating of the material layers.

A sequence of constant irradiance shots varying target thicknesses would be an important first step.

A point not raised in the main body of this chapter has been the quality of the layer interface in the target. A number of workers(3.23) have predicted the catastrophic effect and ambiguous results from shock propagation over material interfaces which contain imperfections and voids. As discussed earlier the target preparation quality was a factor not under great control and some degree of interface imperfections are likely to have prevailed.

If the multilayer technique could be developed with sufficient confidence a number of unique experiments could be envisaged. Thermal smoothing experiments, as described in Chapter Five, could utilise multilayer targets to measure the evolution of non-uniformities in shock front profile during target irradiation, therefore diagnosing the phases of transient and steady state smoothing. A wavelength shaping experiment as suggested by a number of authors could be envisaged in which phases of 1.06 μm radiation and 0.35 μm radiation would provide a hot smoothing atmosphere and good coupling of energy into the target. The multilayer target technique could be a useful diagnostic to monitor these phases of irradiation.

An instability growth mechanism which is currently under increasing attention is the so-called Richtmeyer Meshkov instability. This instability causes growth of irregularities on a material interface due to shock acceleration. A multilayer target experiment could be envisaged to measure the growth of spatial non-uniformities if sufficient spatial resolution could

be achieved and there was a careful choice of material layers.

CHAPTER FOUR

TIME RESOLVED TEMPERATURE MEASUREMENTS USING A DUAL CHANNEL PREHEAT DIAGNOSTIC

4.1 Abstract

Time resolved temperature measurements have been made using the 'thermal' continuum emission from the rear surface of Aluminium foil targets irradiated with 300 psec FWHM pulses of 1.06 μm radiation. A purpose built dual channel optical diagnostic (coupled to a streak camera) has recorded shock temperatures up to 1.5 eV with precursor emission inferring levels of target preheat in the range 0.1 - 0.5 eV. An f2.5 flat field grating spectrograph (also coupled to an optical streak camera) has inferred temperatures consistent with the dual channel values. Emission from a stepped foil has given a self consistent calibration through shockwave velocity-shockwave temperature, inferred from equation of state data for Aluminium.

4.2 Introduction

It is well appreciated in current laser fusion studies that target preheat of only a few electron volts can significantly change the isentropic path along which fuel is

compressed for high density target designs, thus producing a significant reduction in compression and pellet yield(4.1).

Equation of state experiments suffer severe complications since the material ahead of the shockfront becomes preheated rendering the initial cold states unknown. Preheat mechanisms have been attributed to suprathermal or fast electron production(4.2), X-ray radiation(4.3) and shock wave heating(4.4). Considerable effort has therefore been invested in measuring levels of target preheating; such time resolved studies have included X-ray spectroscopy using K_α measurements(4.5) and at a lower level, optical pyrometery using photomultiplier tubes and monochromators(4.6,4.7). In particular, low level (few eV) subnsec. temperature diagnosis has been restricted to optical streak photography using a 'colour' temperature measurement(4.8).

This chapter describes the use of such a dual channel optical diagnostic to record the continuum emission from the rear surface of laser irradiated targets. Temperatures inferred from this technique can have good accuracy (few %) in the 0-2 eV range coupled with high time resolution inherent with streak camera use (< 10 psec). Such an approach is particularly amenable to the measurement of low levels of target preheating.

These experiments assume the rear surface of the irradiated target emits as a blackbody, consistent with results obtained by some workers(4.9). It was intended that this assumption could be verified on each laser shot with the use of a simultaneous recording of the spectrum by the 'streak'

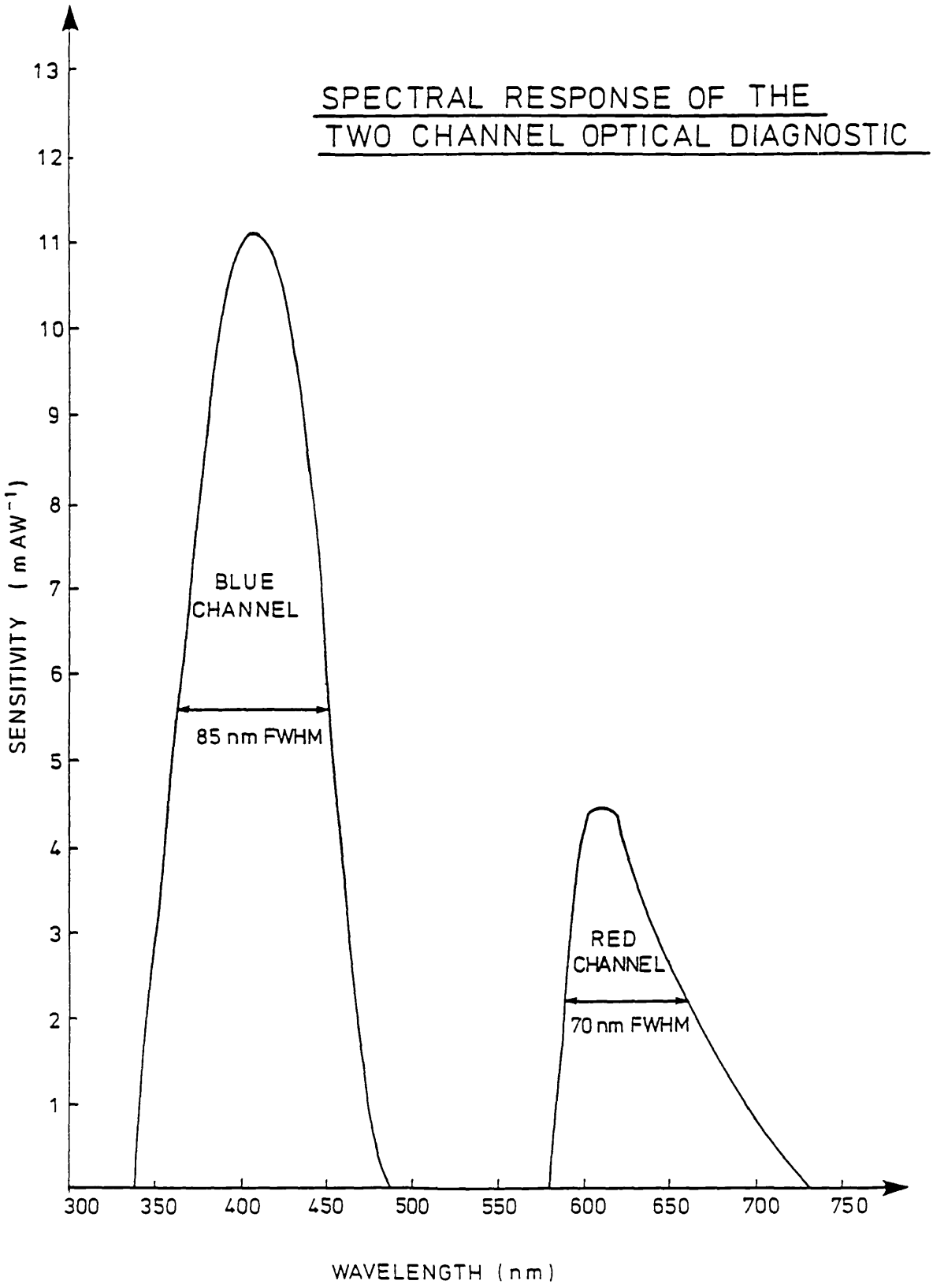

Fig.4.1 The spectral response of the two channel optical diagnostic.

spectrograph[4.10]. It should be stated that the work described here constitutes the commissioning experiment for the two channel diagnostic. The quality of available targets was not high and as such the main objective of this experiment was the establishment of the correct operation of the diagnostic rather than the accurate measurement of target preheating levels under well defined laser irradiance conditions.

4.3 The dual channel optical diagnostic

The dual channel optical diagnostic has been designed to be coupled to a conventional optical streak camera, using the relative intensity of continuum emission in two spectral bands in the 'visible' region of the spectrum to infer a value for the temperature of the rear surface of the targets.

The diagnostic contains an achromatic relay lens and a spectral/spatial beamsplitter which splits the emission from the target to relay two separate images of different spectral content along different optical paths onto the slit of the streak camera. Each of the two channels has additional independent spectral filtering with colour glass filters which, in these experiments were BG12 for the blue channel and OG590[4.11] for the red channel. The spectral response of the complete system from target plane to streak camera film plane has been calculated by convolving the spectral responses of all the elements in the system (including camera photocathode response). This spectral response function is shown in Fig.4.1. The channels are centred at 410 nm and 620 nm with bandwidths of 87 nm FWHM and 70 nm FWHM respectively. The choice of position

Fig.4.2 The spectral response of the S20 photocathode employed in the optical streak camera.

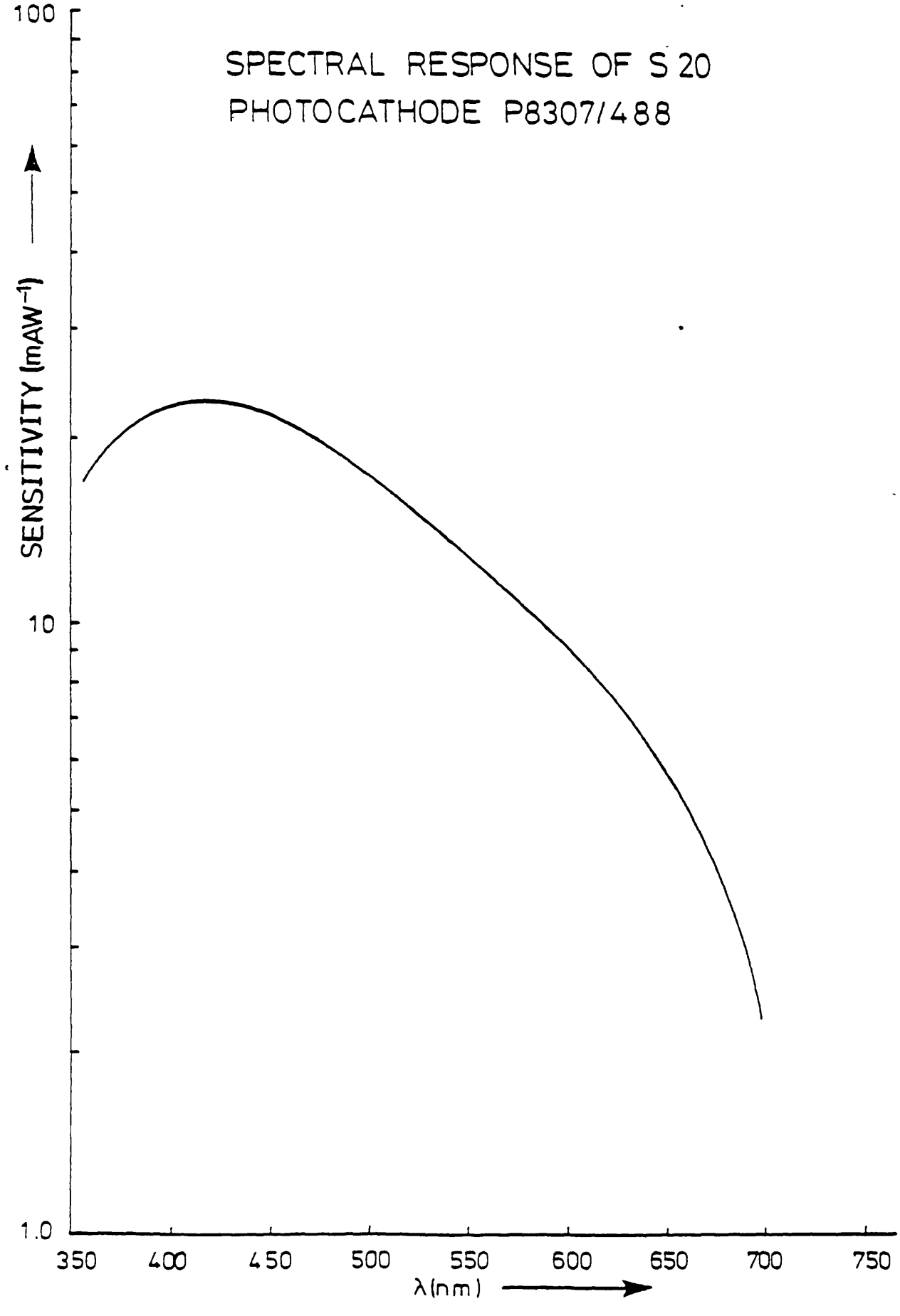

and width of each channel is discussed in section 4.4, but the practical constraints are governed primarily by the fall off in sensitivity of the conventional streak camera S20 photocathode as shown in Fig.4.2 and the low level transmission of conventional optics to ultraviolet radiation. Other practical limitations included the matching of the relay lens f number with mirror geometry to ensure each channel emission was within the acceptance cone of the streak camera relay optics situated behind the camera slit.

The image magnification was chosen to be compatible with a region of emission in the target plane of the order of 200 μm and the usable length of the streak camera slit of $\sim$ 7 mm.

4.4 Calculation of foil temperature

The emission of electromagnetic radiation from a body at a specific wavelength can be used to infer a temperature of the body if an intensity distribution function for wavelength and temperature is known or assumed. Absolute experimental measurement of a single spectral intensity is difficult due to the complex calibration of the detection system. It is more convenient to measure the intensity at two wavelengths and use the ratio to infer a value for the temperature.

The spectral intensity of emission of a 'blackbody' is well known from Planck's formula and can be expressed as :

$$I(\lambda,t) = \frac{2hc^2}{\lambda^5} \frac{1}{e^{hc/\lambda kT} - 1} d\lambda \qquad 4.1$$

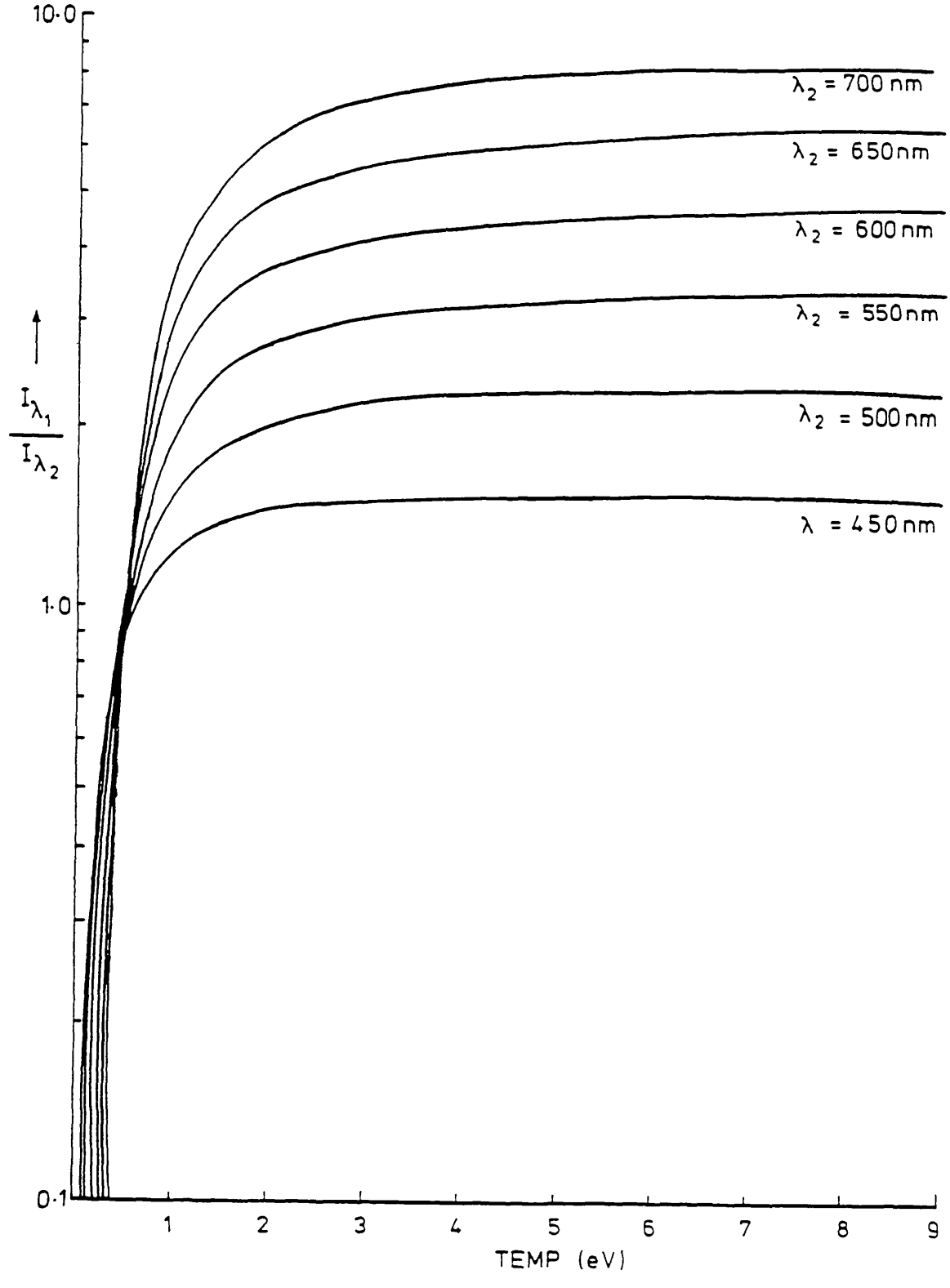

Fig.4.3 The variation of ratio of spectral intensity $(I_{\lambda_1}/I_{\lambda_2})$ at wavelength bands λ_1 = 400 nm and λ_2 = 450-700 nm as a function of temperature.

where I is the flux of radiation emitted in a waveband of $d\lambda$, from a surface of unit area into unit solid angle. h is Planck's constant, k is Boltzman's constant, c is the velocity of light, λ is the wavelength of emission and t is the temperature of the emitting body.

For unit wavelength bandwidth, the ratio of intensity for wavelengths λ_1 and λ_2 can be expressed as :

$$\frac{I_{\lambda 1}(t)}{I_{\lambda 2}(t)} = \left(\frac{\lambda_2}{\lambda_1}\right)^5 \frac{e^{hc/\lambda_2 kT} - 1}{e^{hc/\lambda_1 kT} - 1} \qquad 4.2$$

If the emission from the rear surface of a laser irradiated foil can be expressed by equations 4.1 and 4.2, the accuracy of the measurement of the foil temperature is governed by the sensitivity of the intensity ratio to change in source temperature. Maximisation of the sensitivity over, and extension of, the useful temperature range can be achieved by careful choice of wavelength bands.

To investigate the sensitivity over a given temperature range equation 4.2 has been used to calculate the ratio as a function of temperature in the region 0-10 eV for wavelength bands of λ_1 = 400 nm and λ_2 in the range 450-700 nm. This is shown graphically in Fig.4.3.

If the source temperature decreases by δt, the change in intensity ratio can be expressed as :

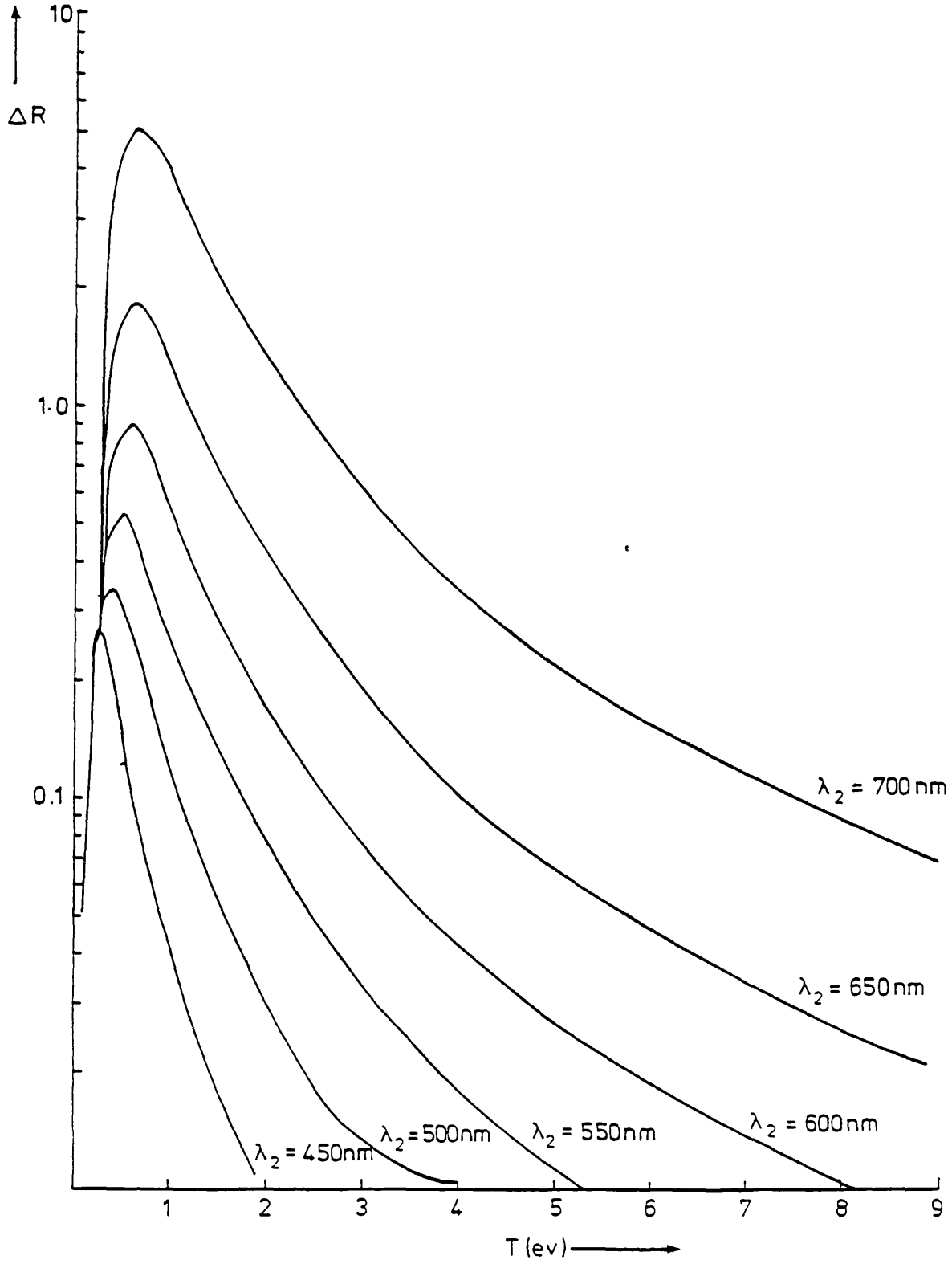

Fig. 4.4 The change in spectral intensity ratio ΔR for a change in temperature of 0.1 eV for wavelength bands of λ_1 = 400 nm and λ_2 = 450-700 nm.

$$\Delta R = \frac{I_{\lambda 1}(t)}{I_{\lambda 2}(t)} - \frac{I_{\lambda 1}}{I_{\lambda 2}} \frac{(t - \delta t)}{(t - \delta t)} \qquad 4.3$$

To illustrate the sensitivity of the intensity ratio to a small change in source temperature, equation 4.3 has been used to calculate ΔR for δt = 0.1 eV. The results are shown graphically in Fig.4.4. This figure shows that the ratio of emission varies sharply with temperature up to $\sim$ 1.5 eV thereafter becoming relatively insensitive to temperature change depending on choice of the second wavelength channel.

Both Fig.4.3 and 4.4 demonstrate that maximum sensitivity and greatest usable temperature range is achieved with the widest separation of channels.

The practical constraints of photocathode response, conventional optics and the use of infra red blocking filters (necessary for the protection from scattered 1.06 μm laser light) result in an initial experimental positioning of the channel at 410 nm and 620 nm. The channel widths have been chosen purely on a pragmatic basis using conventional glass filters. These are 85 nm FWHM for the blue channel and 70 nm FWHM for the red channel. It is intended that experimental results will guide the optimisation of these parameters for future work.

A calibration graph for the dual channel diagnostic can now be derived by convolving the intensity of blackbody emission with the system spectral response for each wavelength, i.e. if $S(\lambda)$ describes the spectral response at each wavelength

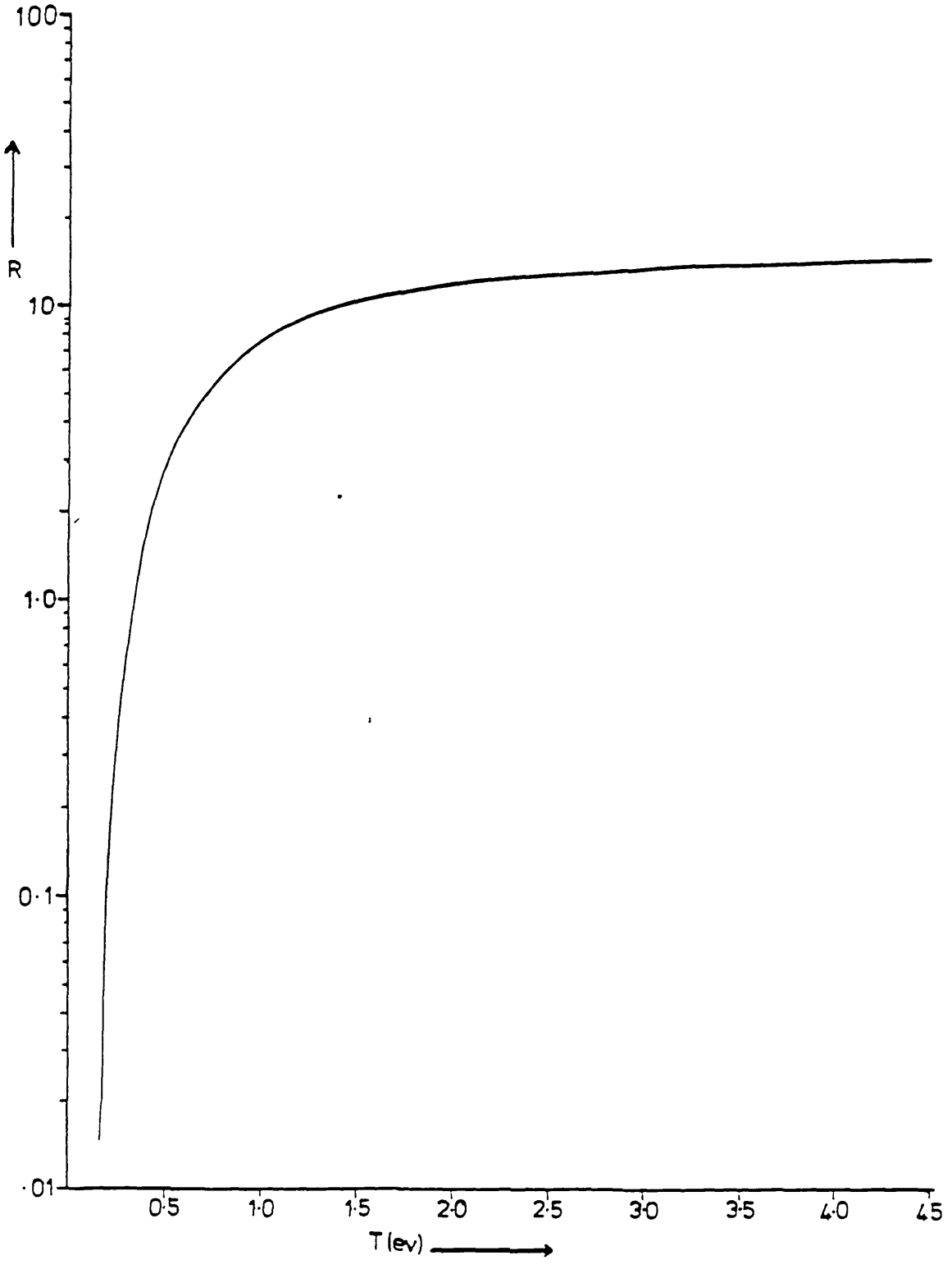

Fig.4.5 The variation of experimentally measured intensity ratio R as a function of temperature T (eV).

(Fig.4.1) the emission recorded by the system should be

$$I(\lambda,t) \times S(\lambda)$$

If λ_1 and λ_2 represent the limits of response in the 'blue' channel and λ_3 and λ_4 are the limits in the red channel then total emission in the blue channel for a fixed temperature t is :

$$I_B(t) = \sum_{\lambda=\lambda_1}^{\lambda=\lambda_2} I_\lambda(t)\ S(\lambda)$$

and for the red channel

$$I_R(t) = \sum_{\lambda=\lambda_3}^{\lambda=\lambda_4} I_\lambda(t)\ S(\lambda)$$

therefore the recorded ratio of emission

$$R(t) = \frac{I_B(t)}{I_R(t)} \qquad 4.4$$

Equation 4.4 has been calculated for a range of temperatures up to 5.0 eV and is shown graphically in Fig.4.5.

This calibration graph can now be used to infer temperatures from the diagnostic from the experimentally recorded ratios of emission intensity.

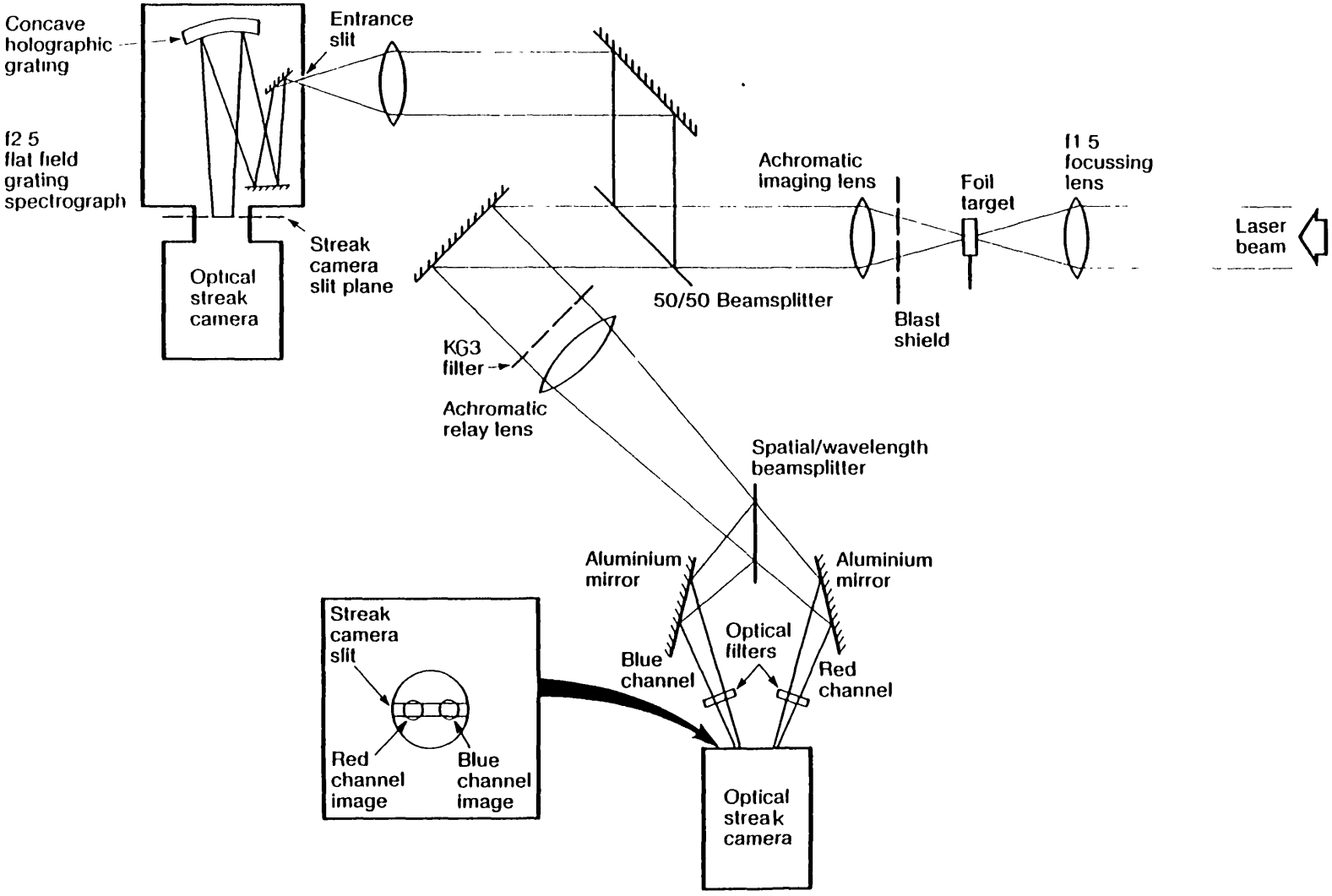

Fig.4.6 Experimental arrangement to record the emission from a laser irradiated foil with the dual channel diagnostic or a 'streak' spectrograph.

4.5 Experimental

The single beam of the AWRE Aldermaston 'MERLIN' laser system[4.12] was used to irradiate aluminium foils (some stepped) with 300 psec FWHM pulses of 1.06 μm laser irradiation. Fig.4.6 shows the experimental layout where the 6.4 cm beam was focussed down using an f4.5 aspheric lens to produce 200 μm FWHM focal spots onto foil targets. The foils were both planar and stepped and were typically 5-15 μm thick and cm in lateral extent. This measure was taken to prevent anomalous energy transport around the target as reported recently by some workers[4.13]. Laser energy in the range 2-15 J gave incident laser irradiances in the region $2.6 \times 10^{13} - 1.1 \times 10^{14}$ Wcm^{-2}.

The rear surface of the targets was viewed with an f1.5 5 cm achromatic camera lens protected from incident laser light by KG3 IR absorbing filters and from rear surface target spallation by remote mylar blast shields. A rear surface illumination system located the image of the target step through the two channel diagnostic onto a 100 μm wide streak camera slit orientated transversely to the step plane. The Hadlands 675 Imacon streak camera was equipped with an S20 photocathode (Fig.4.2). Nominal temporal and spatial resolutions are estimated at 10 psec and 10 μm respectively.

As the shockfront approaches the rear surface of the target the material is promptly heated and emits radiation in the 'visible' region. As described in section 2.3 the use of stepped targets allows the average shock velocity to be inferred from the transit time across the step.

In the latter part of the experiment a fraction of the

Fig.4.7 A streak photograph from 1 6.7 μm Al foil (Shot 765) and microdensitometer tracings through (a) blue channel and (b) red channel.

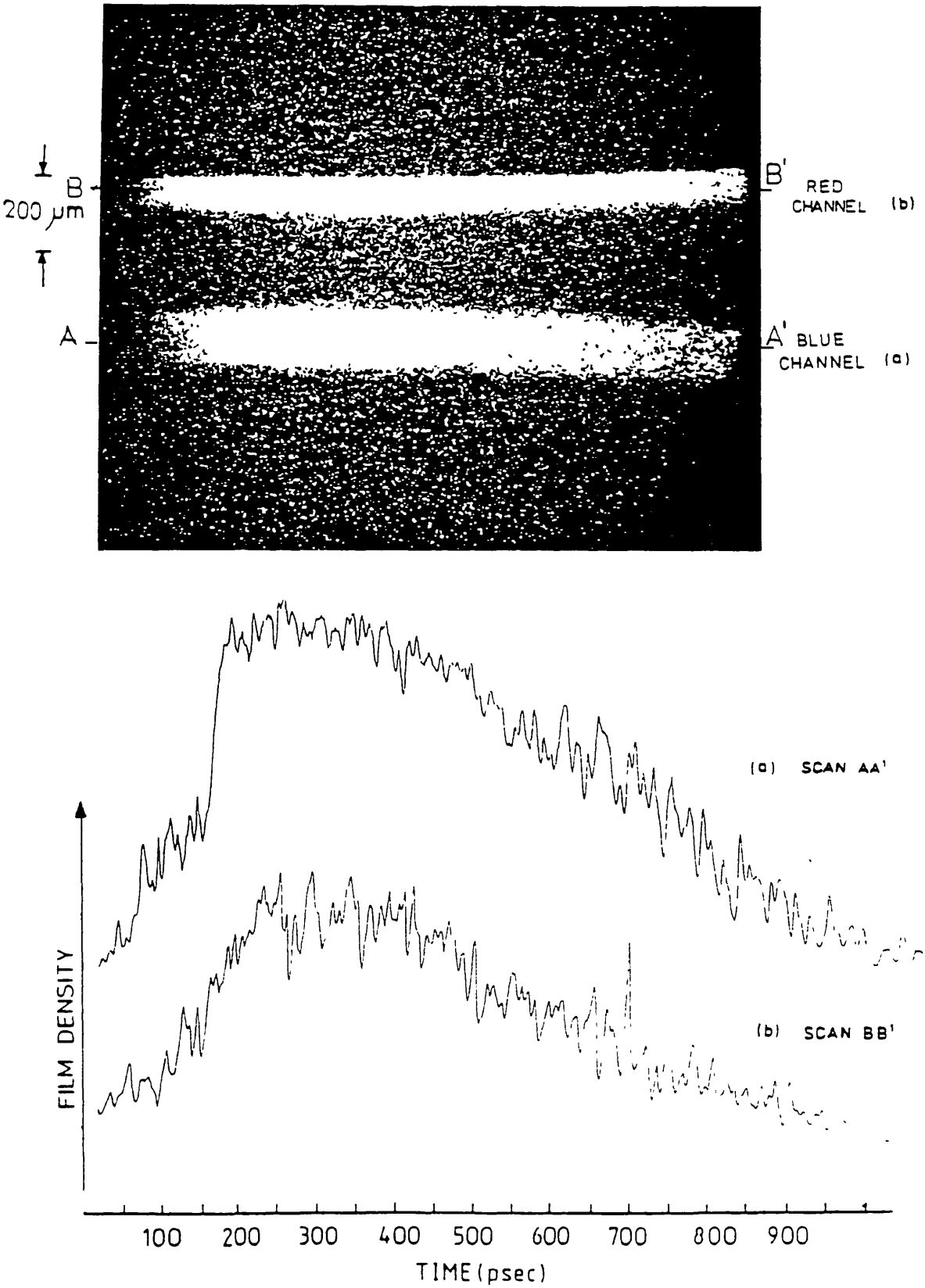

rear surface emission was split off with a cubic beamsplitter and relayed onto an f2.5 flat field grating spectrograph(4.10) also coupled to an identical streak camera. The spectral range covered was 360 nm to 640 nm with a mean linear reciprocal dispersion of 150 A mm^{-1}.

4.6 Results

An optical streak photograph from the two channel system for a 6.7 μm aluminium foil is shown in Fig. 4.7(a). Microdensitometer tracings through each of the channels is shown in Fig.4.7(b) and (c). The time 'zero' is set relative to the onset of emission as no absolute timing fiducial (as employed in Chapters Two and Three) was available.

A selection of four further examples of the dual channel streaks are shown in Fig.4.9. The streak images have been colour-enhanced assigning different colours to different levels of film density (as shown by the colour scale wedge on each photograph). Precursor emission ahead of the main shock is evident in all four cases, the temporal and spatial scale are common to all of the images.

Microdensitometer tracings have been taken for each channel in each of the images and deconvolved from the recording film (Ilford HP5) 'gamma' curve(4.14). The ratio of emission intensity has then been used together with the diagnostic calibration graph Fig.4.5 to produce a value for the rear side temperature as a function of time. An example of this is shown in Fig.4.8 for shot no.765.

Referring to Fig.4.8 it is apparent that there is a

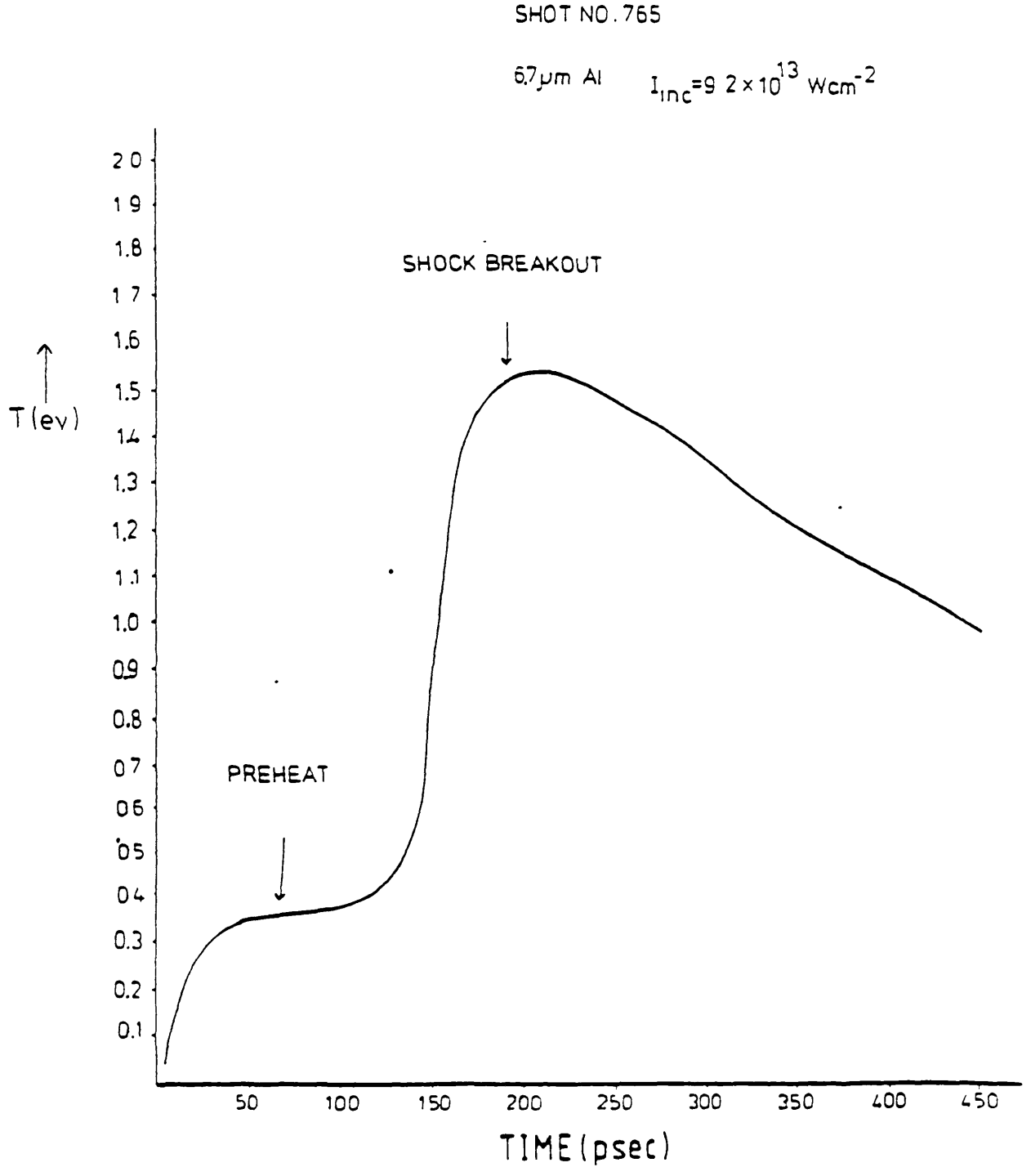

Fig.4.8 The temporal history of the rear surface temperature of a 6.7 μm Al foil I_{inc} = 9.2 x 10^{13} w cm^{-2}.

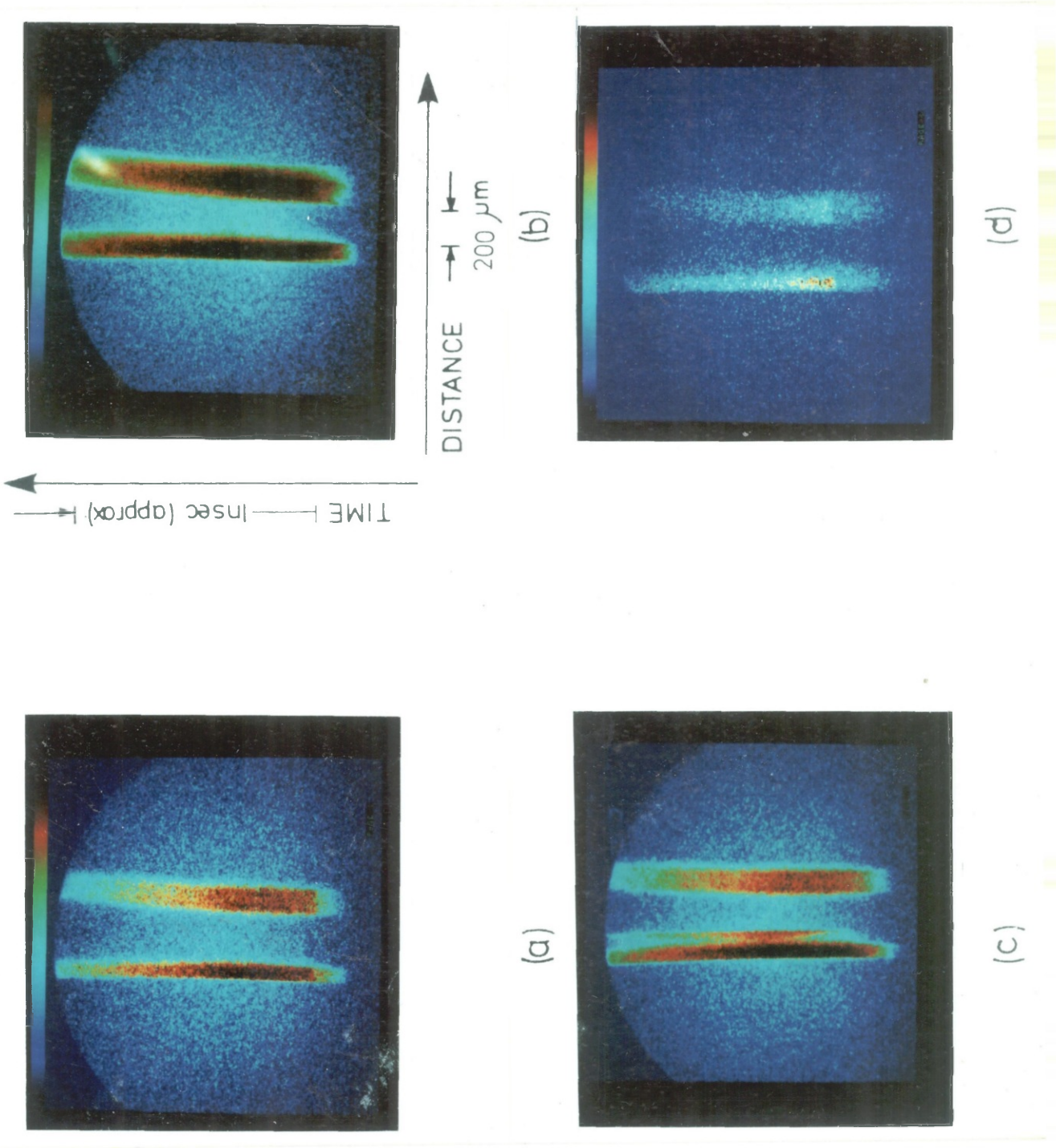

Fig.4.9 A selection of four colour enhanced optical streak records for (a) Shot no.721, (b) Shot no.765, (c) Shot no.720, and (d) Shot no.534.

Fig.4.10 The temporal history of the rear surface temperature for (a) 5 μm Al foil and (b) 10 μm Al foil at I_{inc} 6.6 x 10^{13} w cm^{-2}.

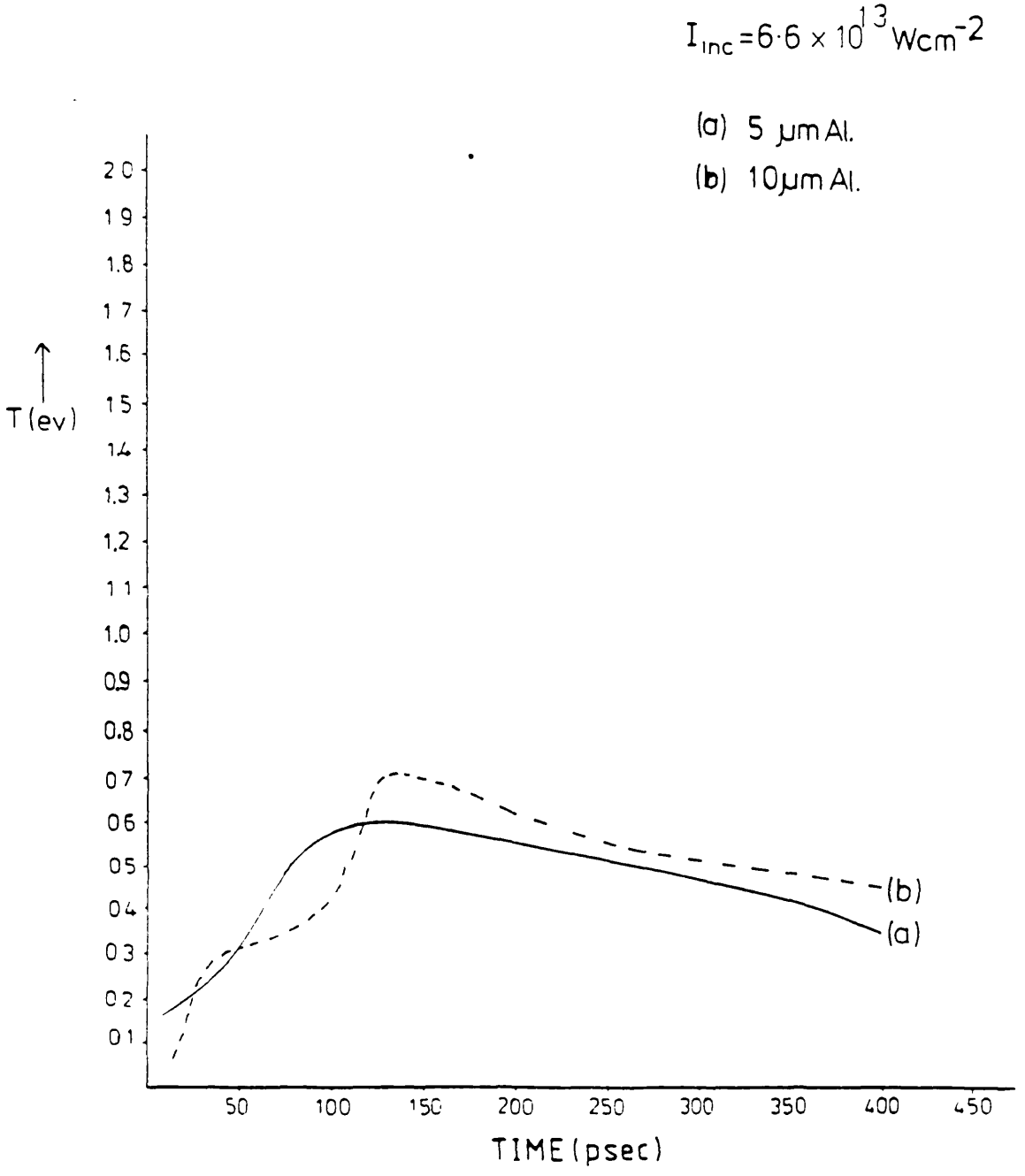

region of low level precursor emission - preheat, of the order of 0.35 eV - for a short period ∿150 psec before the main shockfront emerges promptly heating the rear side to ∿ 1.5 eV. The source of the target preheating under these laser conditions could be either fast electrons or X-ray radiative heating(4.15).

An example of shots from targets of different thicknesses, (i.e. 5 μm and 10 μm aluminium) at approximately the same laser irradiance is shown in Fig.4.10. It can be seen that the main shock signal is delayed by ∿ 50 psec for the 10 μm foil compared with the 5 μm case. It would however not be sensible to estimate an average shock velocity from the difference in transit times since the relative timings are not well defined. The peak temperatures reached for each target are similar with a merging of the preheat main shock signs to form a longer risetime signal in the 5 μm foil case. The thicker 10 μm foil emission profile is consistent with shot 765 in Fig.4.9.

All the results are tabulated in Table 4.1, showing the target dimensions, laser irradiances, inferred preheat and peak shock temperatures.

An example of a streaked spectrum recorded by Carter(4.16) is shown in Fig.4.11, for shot no. 770. Unfortunately a stepped streak image was not recorded by the two channel diagnostic, however a tentative cross calibration is possible. In Fig.4.11 the time resolved spectrum is shown in (1), a tracing at 500 nm (DD^1)(2) shows a double intensity feature which could sensibly be explained by emission from the target base and step. The time difference between these

TABLE 4.1

Shot no.	Target (μm) [Aluminium]	Incident Irradiance (10^{13}/Wcm^{-2})	Preheat Temperature (eV)	Shock Temperature (eV)	Spectrograph Shock Temperature (eV)
% Error	± 30%	± 30%	± 15%	± 15%	± 10%
721	10.0	4.1	0.3	0.75	-
534	3.0	2.6	0.2	0.45	-
711	10.0	11.1	0.1	0.97	-
765	6.7	9.2	0.35	1.55	-
730	10.0	6.6	0.32	0.65	-
811	5.0	6.6	0.25	0.63	-
532	3.0	12.2	0.35	2.5	-
770	5.0+5.0 (stepped)	10.0	0.32	0.50	0.45

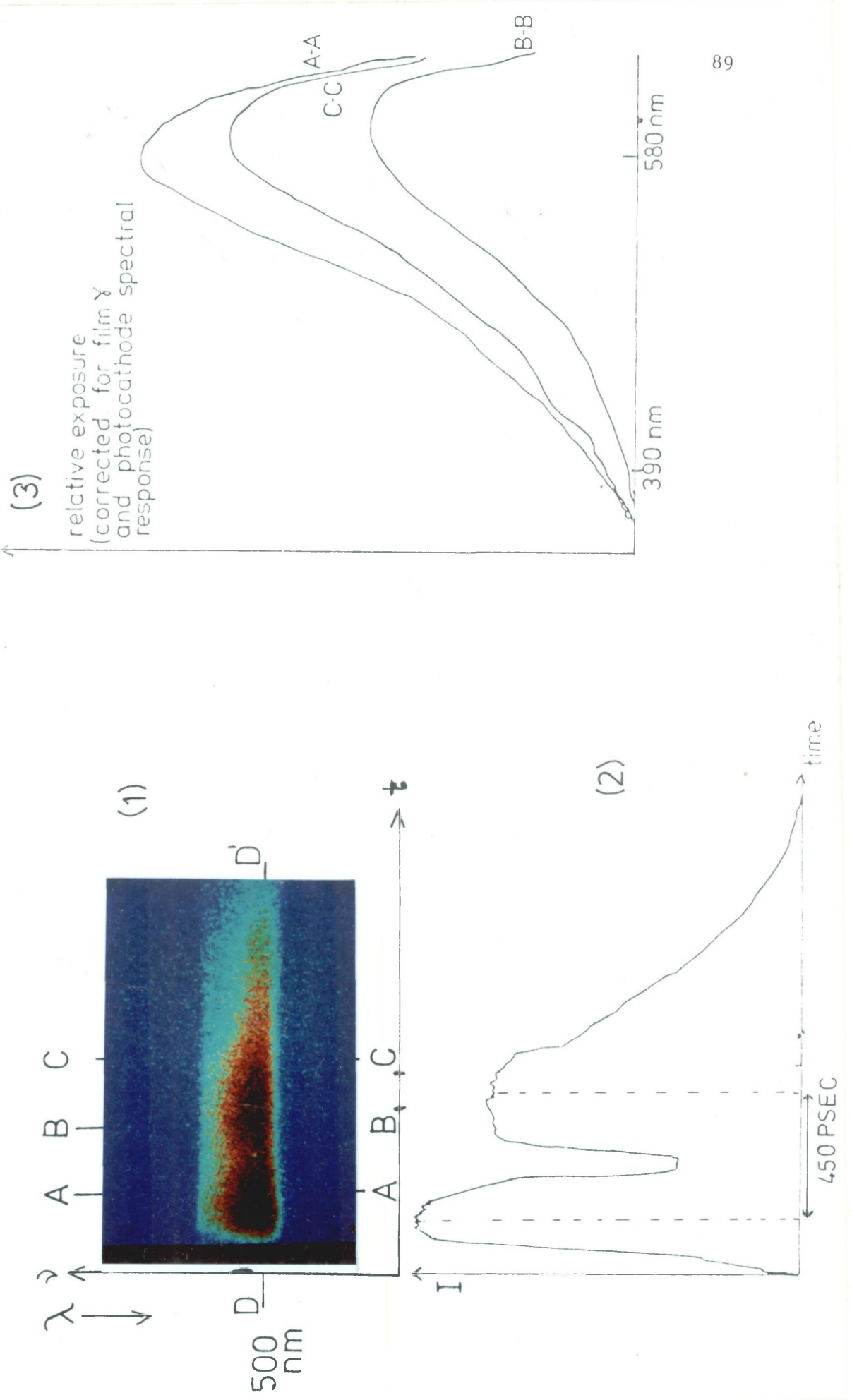

Fig.4.11 An example of a 'streaked' spectrum from Shot 770 (1) optical streak photograph, (2) microdensitometer tracing SCAN DD', and (3) the spectra at three different times of emission from ref.(4.10).

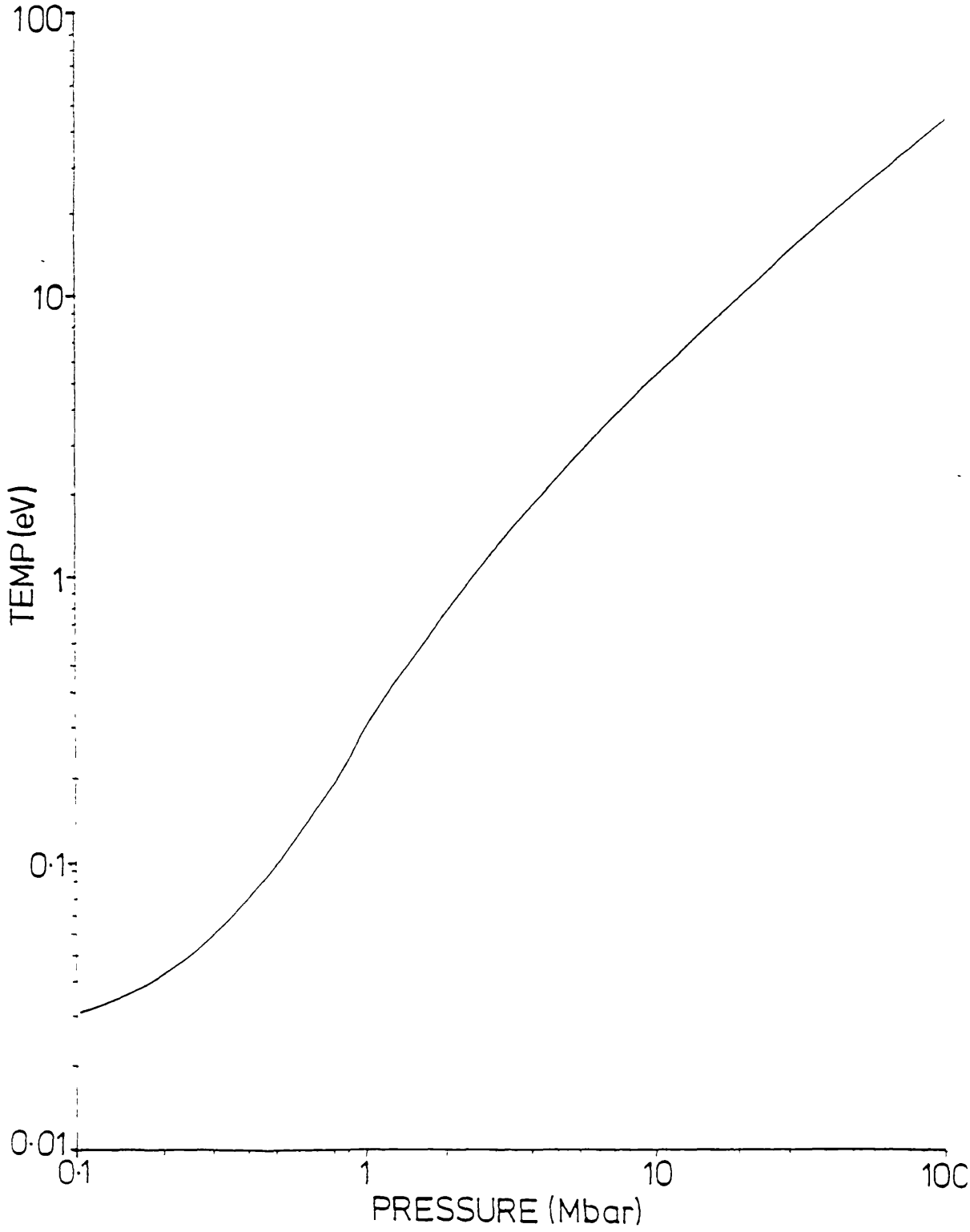

Fig.4.12 The variation of shock temperature as a function of shock pressure for aluminium from ref.(4.17).

out. Furthermore an extension of the usable temperature range could be effected by movement of one of the channels to the far UV wavelength. An X-ray streak camera could then be used e.g. CsBr photocathode to detect the emission. Cross calibration of both channels could be obtained by stepped target emission providing a powerful diagnostic tool for future experimental studies.

CHAPTER FIVE

COMPARATIVE MEASUREMENTS OF THE SMOOTHING OF IMPOSED LASER BEAM INHOMOGENEITIES

5.1 Abstract

Experiments using single beams of 1.06 and 0.35 μm radiation with imposed non-uniformities are described. Evidence of the 'smoothing out' of the inhomogeneities due principally to thermal diffusion between the absorption region and the ablation front is found. Smoothing rates from two different techniques are compared. Results suggest a modulated shockwave transit approach avoids contributions from hydrodynamic effects which were inherent with measurements made using a double 'colliding foil' technique. The first systematic study of smoothing as a function of laser irradiance at 0.35 μm is presented. The degrees of smoothing, measured from modulated shock transit times, are significantly lower than those reported previously[5.1] and are in good agreement with computer simulations[5.2,5.9] and a revised analytical model[5.3,5.8].

5.2 Introduction

There has recently been a considerable amount of experimental and theoretical effort to investigate uniformity of laser irradiation. Inertial confinement fusion studies demand

high illumination uniformity sufficient to yield spherical implosion symmetry of a few percent(5.4). Equation of State experiments also require high quality laser beam profiles to maintain a high degree of shockwave planarity during target propagation(5.5). Indeed, the majority of all laser-irradiation experiments such as filamentation, stimulated Raman and Brillioun scattering, Rayleigh Taylor Instabilities, ablation rate measurements and EXAFS, suffer complications from poor beam quality. These uniformity requirements are unlikely to be met by hardware in high power laser systems(5.6); it is essential therefore to find ways of improving the quality of laser beam presented to the target. A naturally occurring process in the laser plasma has been termed the 'cloudy day' effect and acts to smooth out the transient maximum and minimum in the laser beam profile. It is this process which is the subject of this chapter.

The principal mechanism for the smoothing effects in the plasma is thermal diffusion of energy from areas of high laser irradiance to those of low laser irradiance during transport across the interspace between the critical density surface (absorption region) and the ablation front. This process is shown schematically in Fig.5.2. The interspace (stand-off distance) which governs the degree of diffusion and therefore smoothing, has a time dependent behaviour described by transient and steady-state phases(5.7). More importantly, for laser experiments it is dependent both on the laser wavelength and irradiance(5.8,5.28). A potential Inertial Confinement Fusion scheme will inevitably involve a trade-off between laser

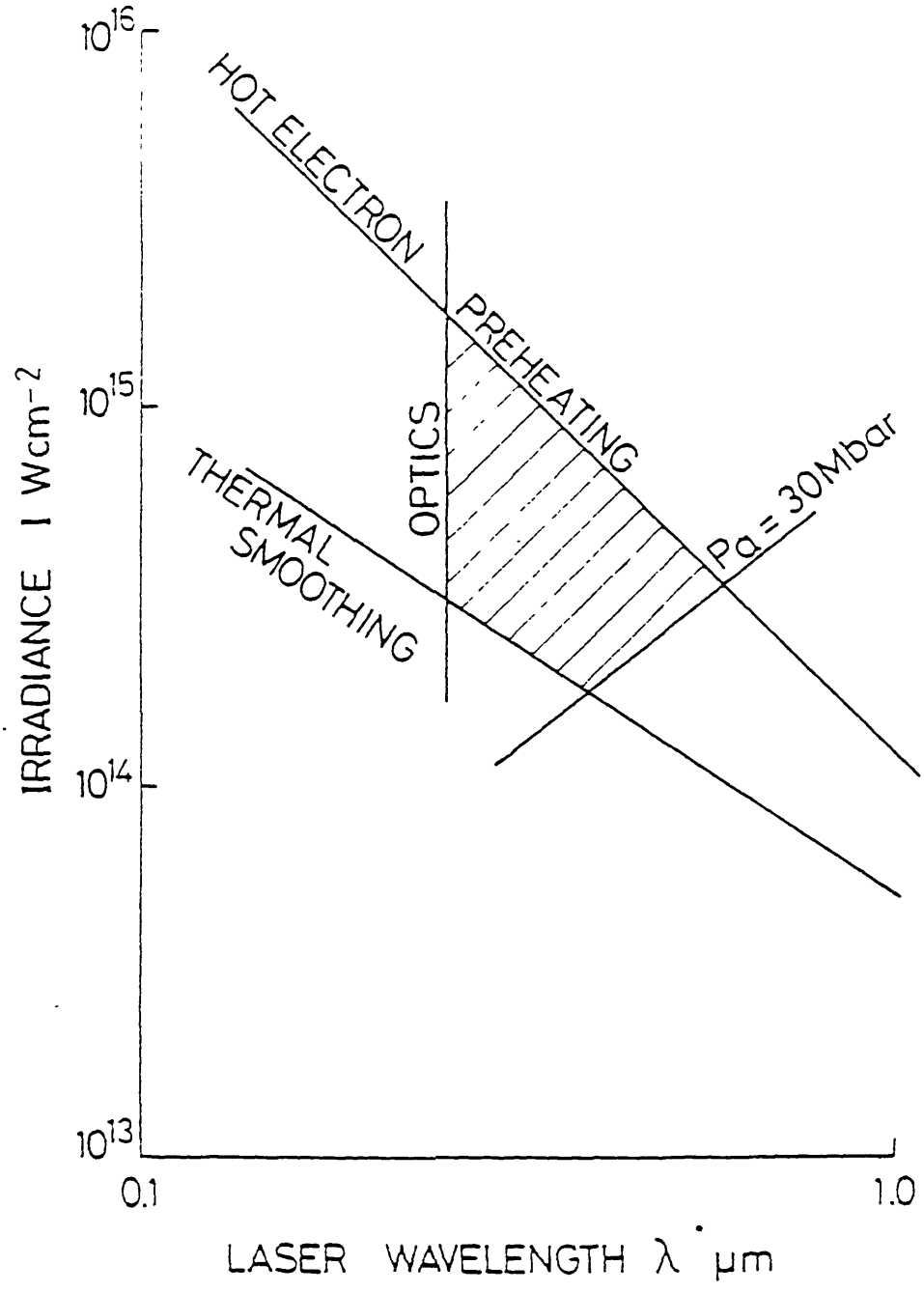

Fig.5.1 A 'parameter' window for a possible I.C.F. scheme demonstrating the importance of thermal smoothing scaling from ref.(5.8).

Fig.5.2 A schematic diagram of thermal diffusion smoothing a laser beam inhomogeneity during transport of energy from the absorption region to the ablation front.

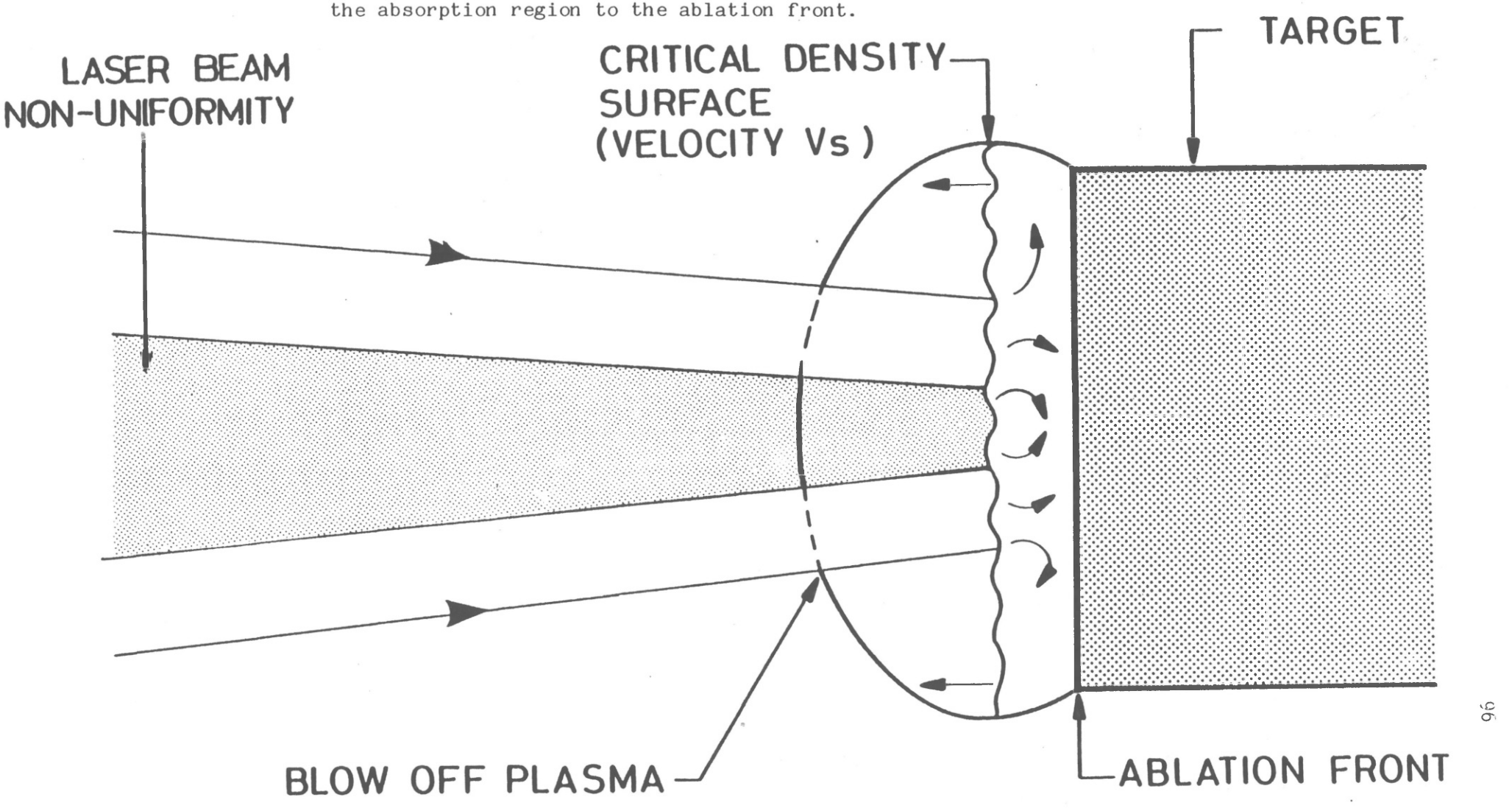

wavelength and irradiance to optimise levels of target preheating, plasma instabilities, high coupling efficiency of laser energy into the target and plasma smoothing. It is important therefore to have a clear understanding of the smoothing mechanism and the degree of smoothing which can be expected under different laser conditions. To illustrate the importance of thermal smoothing in an Inertial Confinement Fusion scheme Fig.5.1 shows a proposed parameter window(5.9) where limits on drive pressure, preheating, optical components and thermal smoothing define the size and indeed existence of this window.

This chapter describes two experiments to measure plasma smoothing effects, the first is an investigatory study at a laser wavelength of 1.06 μm comparing results from both a 'double' foil approach and a modulated shockwave transit technique. The conclusions from this work guide the choice of technique used in the second experiment at 0.35 μm where accurate quantitative results are presented and discussed. Finally some general conclusions and caveats are considered.

5.3 Previous work on smoothing

The first observation of the smoothing of non-uniformly irradiated targets was by Obenschain et al(5.10), who used a doppler shift technique to observe foil velocity non-uniformity. A subsequent study, again by Obenschain et al(5.11) used a more sensitive approach of double colliding foils (described in section 5.5) to measure accelerated foil non-uniformity for different values of laser irradiance. Intuitive reduction in

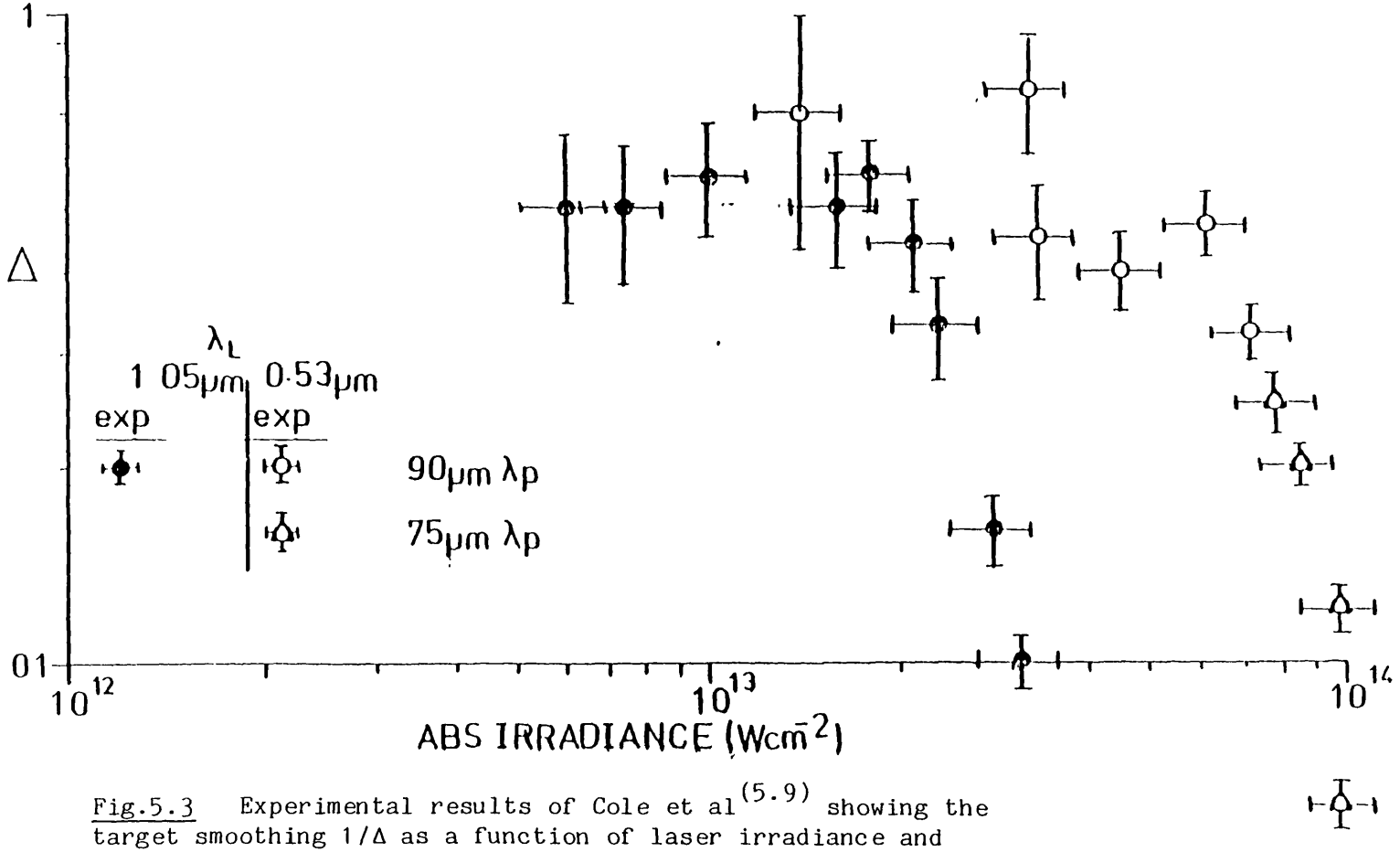

Fig.5.3 Experimental results of Cole et al[5.9] showing the target smoothing $1/\Delta$ as a function of laser irradiance and wavelength for a fixed period (λ_p) of modulation varying as $1/\Delta \propto (I_a \lambda_L^2)^3$.

velocity non-uniformity (increase in smoothing) for increased irradiance (and therefore increased stand-off distance) was observed. Code simulations have been performed by Gardner and Bodner[5.2] and Emery et al[5.12] to predict the scaling of stand off distance and pressure with laser conditions. A simple analytical model based on previous work has been developed by Key[5.3] to describe the phases of transient and steady state smoothing. The only attempt to measure the degree of smoothing present as a function of irradiance and wavelength was by Cole et al[5.1,5.13]. These experiments were performed at 1.06 and 0.53 μm and used X-ray showgraphy to monitor the degree of non-uniformity in an accelerated foil for a constant time. Simulations by Cole[5.1] and others[5.12] show that the measurements made to date inevitably include some contribution from effects associated with bulk target motion such as hydrodynamic decompression and target flow. Fig.5.3 shows the smoothing measurements of Cole for two different wavelengths (some degree of decompression and buckling was conceded).

Some workers have investigated methods of improving illumination uniformity by external means. An Induced Spatial Incoherence technique has been used by Lehmberg et al[5.14]. The author has also performed some recent experiments where spatial incoherence has been used to improve irradiation uniformity[5.15]. Recent experiments using high z layers on targets to radiatively smooth non-uniformities have also been reported[5.16].

A technique which avoids the target acceleration complications is that of a modulated shockwave transit time.

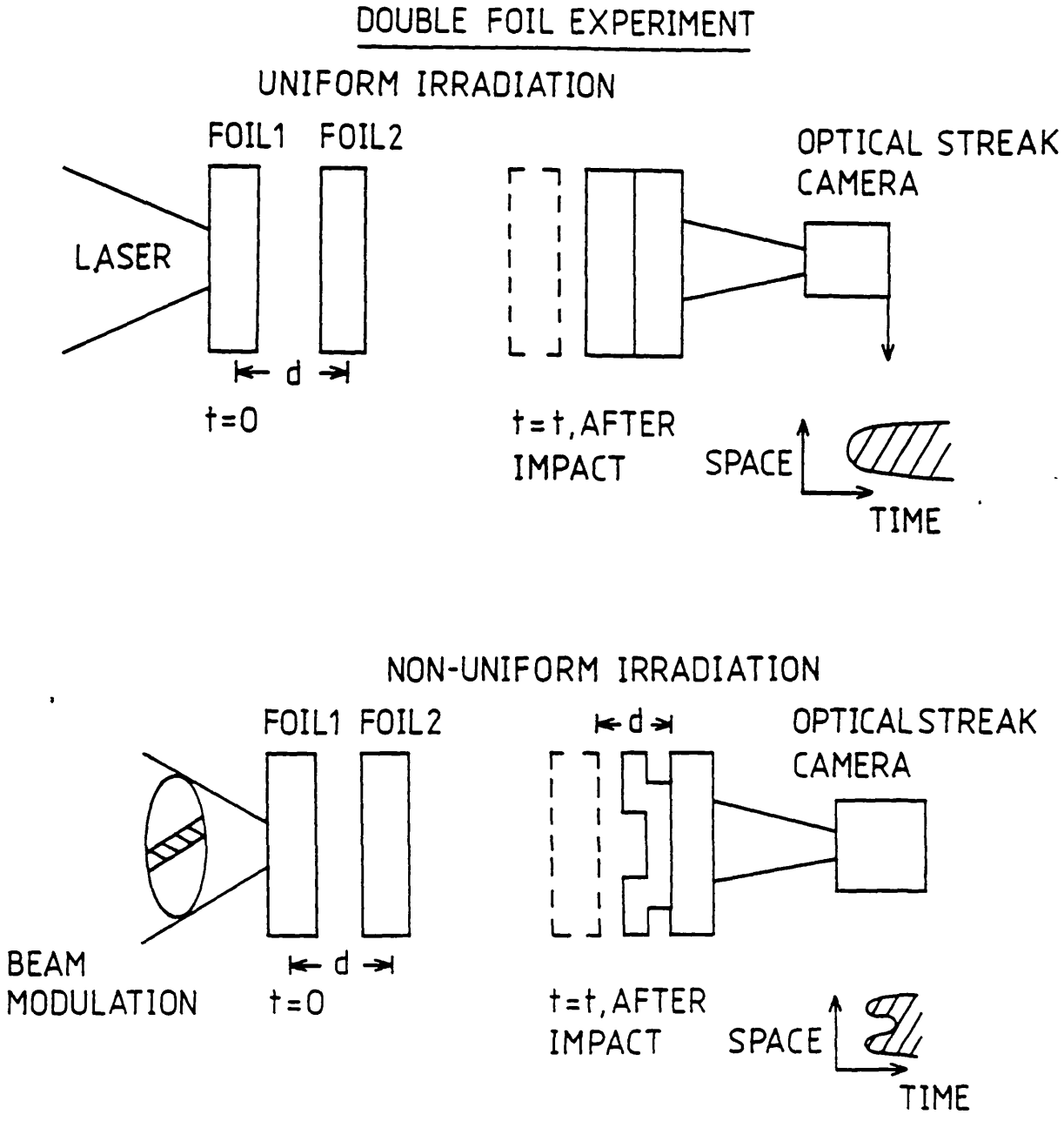

Fig.5.4 Schematic representation of a double 'colliding' foil experiment to measure 'smoothing' of imposed beam inhomogeneities.

Such an approach has hitherto not been used and may be unique in being able to measure plasma smoothing effects selectively without significant contributions from other sources.

5.4 Techniques of measurement of smoothing

As described in section 5.3 experimental measurement of the degree of smoothing of imposed laser beam inhomogeneities has been made using two basic diagnostic techniques. A brief outline of the principles of each is described below :

(a) X-ray shadowgraphy

An auxillary laser beam creates a short pulse of X-rays from a backlighting plasma which shadows the trajectory of a non-uniformly accelerated target. The degree of smoothing is expressed in terms of the ratio of the maximum and minimum distances travelled by the foil at a constant moment in time.

(b) Colliding foil measurement

A double foil target arrangement is non-uniformly irradiated accelerating a first 'flyer' foil into a second static foil. On impact, high and low accelerated regions drive shockwaves of different strength into the static foil. The non-uniformity in shock transit time measured by an optical streak camera describes a foil velocity non-uniformity which is interpreted as a degree of smoothing. This is illustrated schematically in Fig.5.4.

Both of these approaches attempt to diagnose indirectly the depth of pressure modulation on the ablation front which remains after the non-uniformity in laser intensity has been

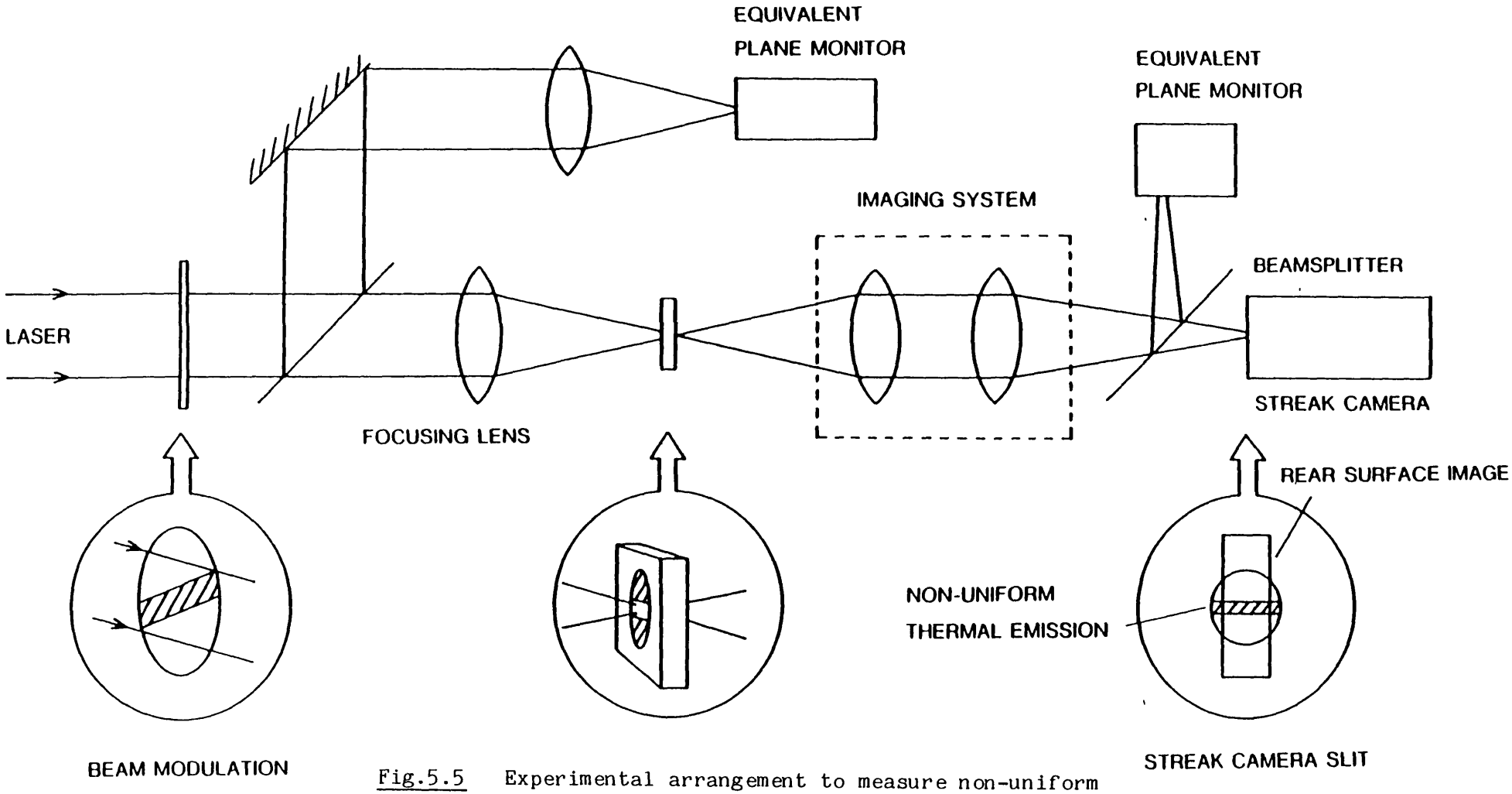

Fig.5.5 Experimental arrangement to measure non-uniform shock breakout emission from the rear of laser irradiated targets.

smoothed out. An inevitable complication of using ablative acceleration of a foil is hydrodynamic effects which contribute an unknown amount to the plasma smoothing.

A technique which does not rely on the gross acceleration of a target utilises the strength of shockwaves driven into the target by non-uniform irradiation.

(c) Modulated shockwave transit time

If a single foil target is non-uniformly irradiated, the pressure non-uniformity drives shocks of different strengths and therefore different transit times through the target. The ratio of maximum and minimum transit times can be used to describe a degree of smoothing.

All three approaches have been used by the author to measure smoothing parameters under different laser conditions. The colliding foil and shock transit time measurements are described in sections 5.6 and 5.9 of this chapter and the X-ray shadowgraphy measurements in Chapter Six.

5.5 Double and single foil smoothing experiments at 1.06 μm

A single beam of the VULCAN Nd glass laser[5.17] was used to irradiate targets with up to 80J in a pulse of 1.5 nsec FWHM. The incident irradiance was varied in range of 10^{13}-10^{15} Wcm^{-2} by variation of the incident laser energy with a constant focal spot size. The experimental arrangement is shown in Fig.5.5. An f1 lens was positioned 200 μm inside focus to give a nominal 200 μm FWHM focal spot size. The two types of target used were: single aluminium foils 25 μm thick, and double foils

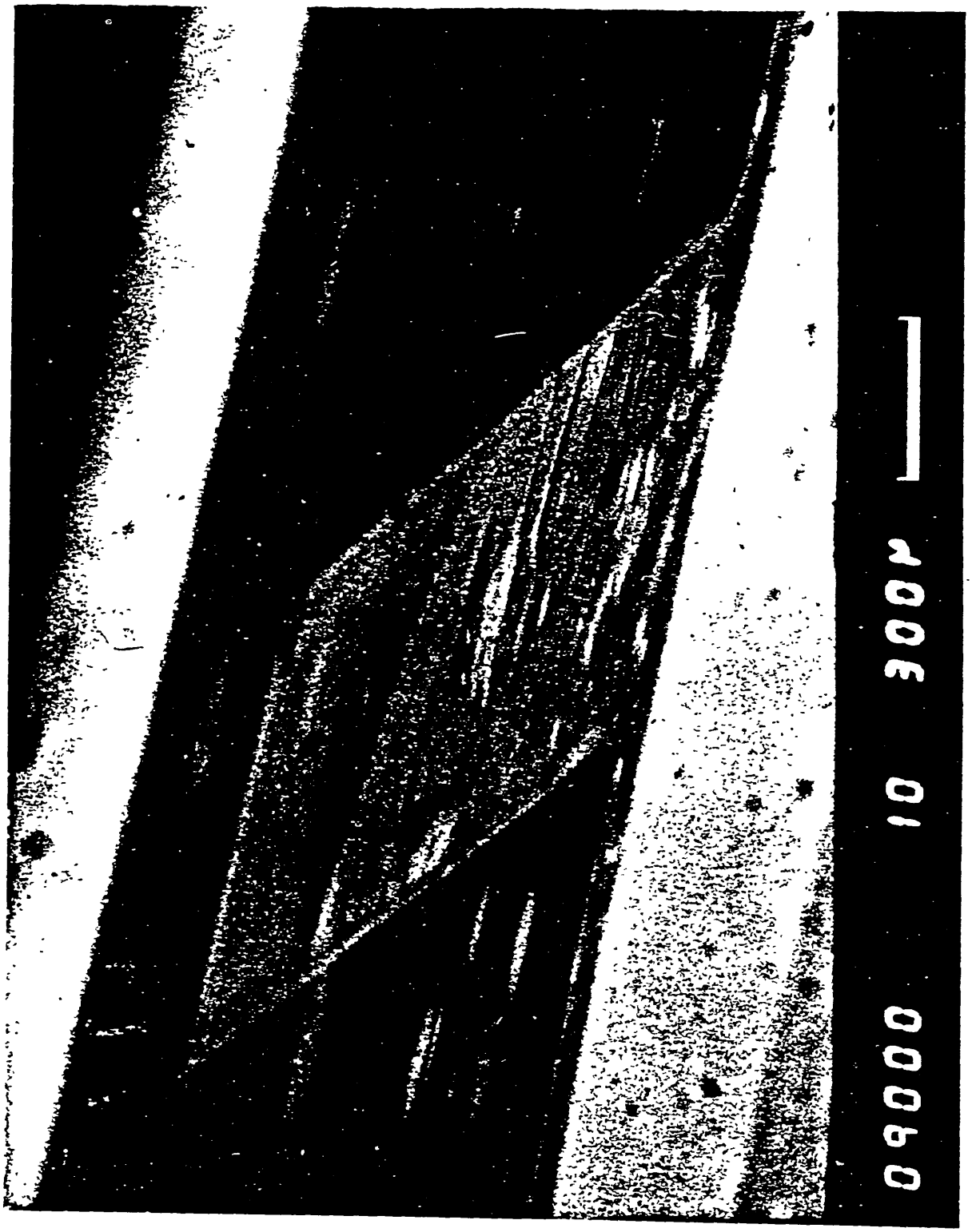

Fig.5.6 A scanning electron microscope photograph showing a double foil target (the second foil will be laid over the target 'well').

consisting of a first foil of 6 μm mylar followed by a second foil of 1.5 μm Al separated by distances in the range 10-50 μm. Fig.5.6 shows a scanning electron microscope photograph of a typical double foil target.

The rear surface of the targets, placed in an evacuated vessel, were imaged by a 25 mm 0.15 NA microscope objective relayed by an f1.5 Dalmeyer achromatic camera lens onto the 100 μm wide streak camera slit of a HADLANDS IMACON 675[5.18] streak camera. Mylar blast shields protected the microscope objective from material ablation damage and infra red KG3 blocking filters protected the camera, equipped with an S20 photocathode, from scattered laser light.

To provide a temporal reference point on the streak photographs a 0.53 μm timing fiducial was incorporated as in previous chapters. Comparative timing of the beams was achieved with the use of a KDP* crystal placed in front of the target chamber window to produce a burst of 0.53 μm radiation within the sensitivity range of the S20 photocathode response.

Focus mode operation of the camera gave the target to camera magnification as 25 and a static spatial resolution of 10 μm. Dynamic resolution was estimated at 10 psec with the streak rates used. The incident laser beam intensity profile was monitored by filtering off part of the main beam and re-imaging with an f50 5 metre lens onto type 55 polaroid pos/neg film. In this experiment the second EPM shown in Fig.5.5 was not available.

The near field of the laser beam was modulated with 2 cm wide strips of Eastman Kodak gelatin filters orientated

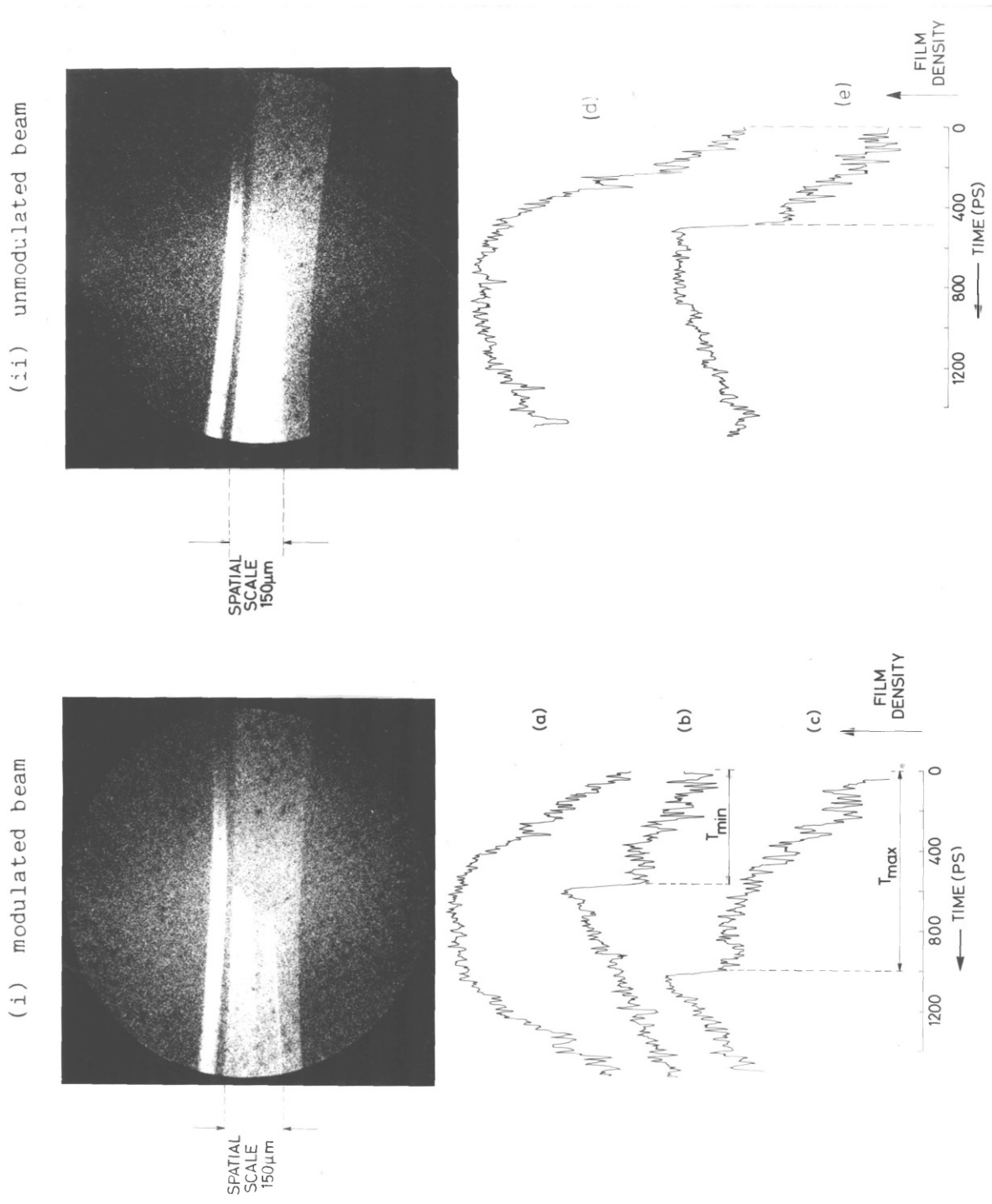

Fig.5.7 Optical streak photographs from a laser irradiated target for (i) modulated beam (ii) unmodulated beam. Microdensitometer tracings through the timing fiducial (a) and (d), minimum and maximum shock breakout times (b) and (c) respectively..

THERMAL SMOOTHING RESULTS AT 1.06 μm

TABLE 5.1 SINGLE FOILS

Shot no.	Target (μm)	T_{min} (psec)	T_{max} (psec)	$T_{max}/T_{min} - 1$	Focal Spot (μm)	Energy (J)	Absorbed Irradiance /10^{13} Wcm^{-2}
% Error	± 10	± 9	± 10	± 20	± 10	± 10	± 30
0622482	25	900	1530	0.7	200	71.4	7.5
1322482	25	900	1620	0.8	200	63.0	6.7
1522482	25	990	2070	1.09	200	26.0	3.3

THERMAL SMOOTHING RESULTS AT 1.06 μm

TABLE 5.2 DOUBLE FOILS

Shot no.	Target (μm)	T_{min} (psec)	T_{max} (psec)	$T_{max}/T_{min} - 1$	Focal Spot (μm)	Energy (J)	Absorbed Irradiance /10^{13} Wcm^{-2}
% Error	± 10	± 9	± 10	± 20	± 10	± 10	± 30
2522482	12.5,50,1.5	2880		UNMODULATED		56.0	6.0
0827482	6,50,1.5	1350	1620	0.20	200	31.0	4.0
0628482	6,50,1.5	3600	4230	0.175	200	29.2	3.7
1128482	6,50,1.5	4250	5290	0.24	200	8.6	1.3
1129482	3.5,50,1.5	2890	3910	0.35	200	7.0	1.0
428482	6,50,1.5	2880	3820	0.33	200	19.4	2.5

transversely to the streak camera slit.

The value of neutral density filter used was adjusted to give an intensity modulation ratio of ≈ 4:1 and a peak to peak period of λ_p = 90 μm in the target plane.

5.6 Results

Examples of optical streak photographs recorded from the rear of targets for the case of (i) modulated beam and (ii) unmodulated beam are shown in Fig.5.7.

A clear modulation in the transit time is produced in the case of the non-uniform beam. Microdensitometry through the 'peak' and 'trough' of the shock breakout profile (b) and (c) respectively define the quantities T_{min} and T_{max}, using the fiducial (a), subject to the uncertainty in time zero for shock propagation as discussed in section 1.8.1. The streak images for both single and double foils were almost identical except that in the latter case the transit times were much larger. Tables 5.1 and 5.2 list the values for each shot together with incident laser energy (corrected for the effect of the beam modulation on target area calorimetry), focal spot size, absorbed irradiances and calculated values of the smoothing parameter δ, where

$$\delta = \frac{\text{Maximum shock transit time}}{\text{Minimum shock transit time}} = \frac{T_{max}}{T_{min}} - 1$$

Absorbed irradiances have been calculated using absorption fractions as per Key et al(5.19). Typical densitometer tracings

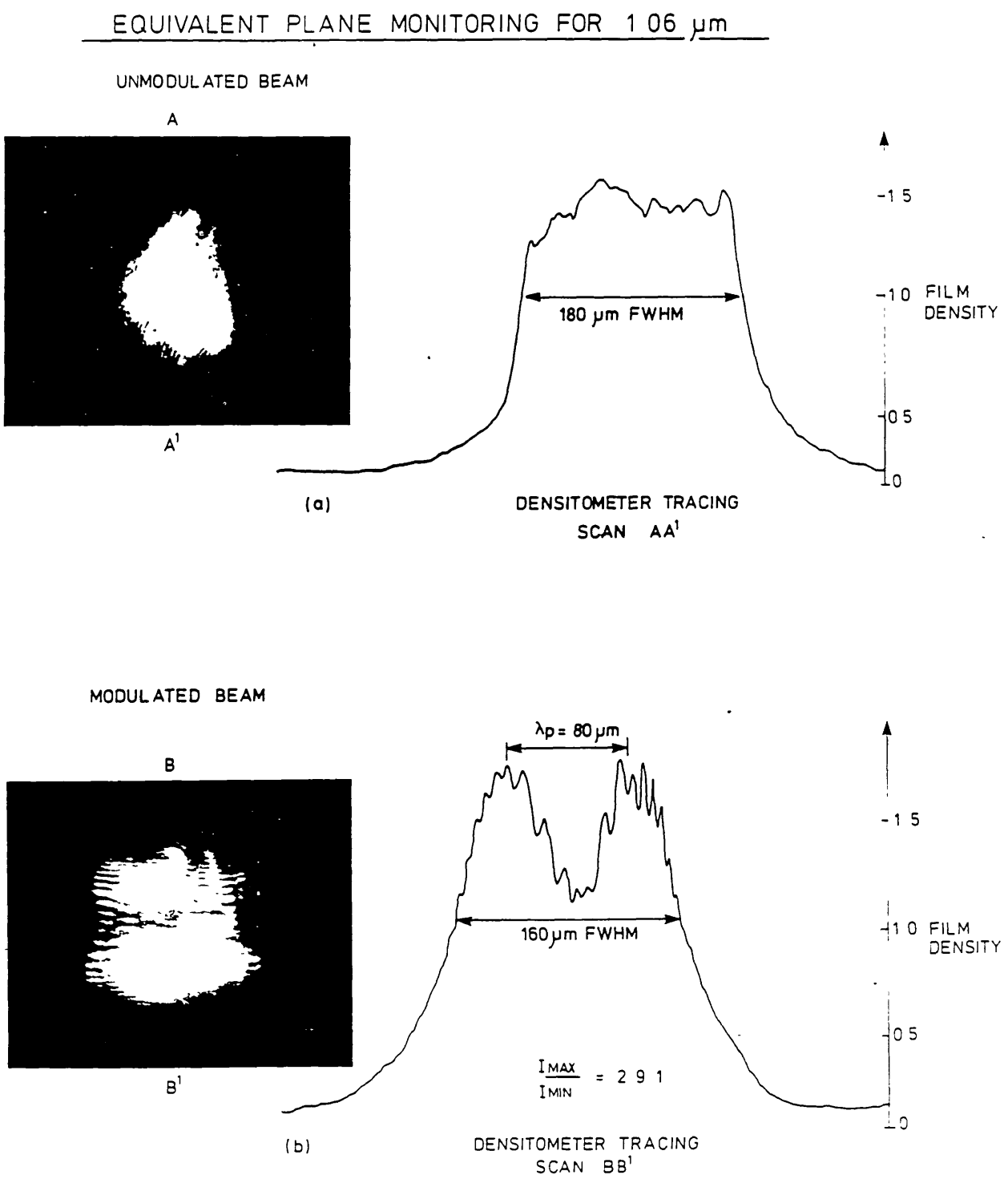

Fig.5.8 Equivalent plane monitor showing (a) unmodulated laser beam profile and (b) modulated laser beam profile (modulation orientated horizontally in the photograph).

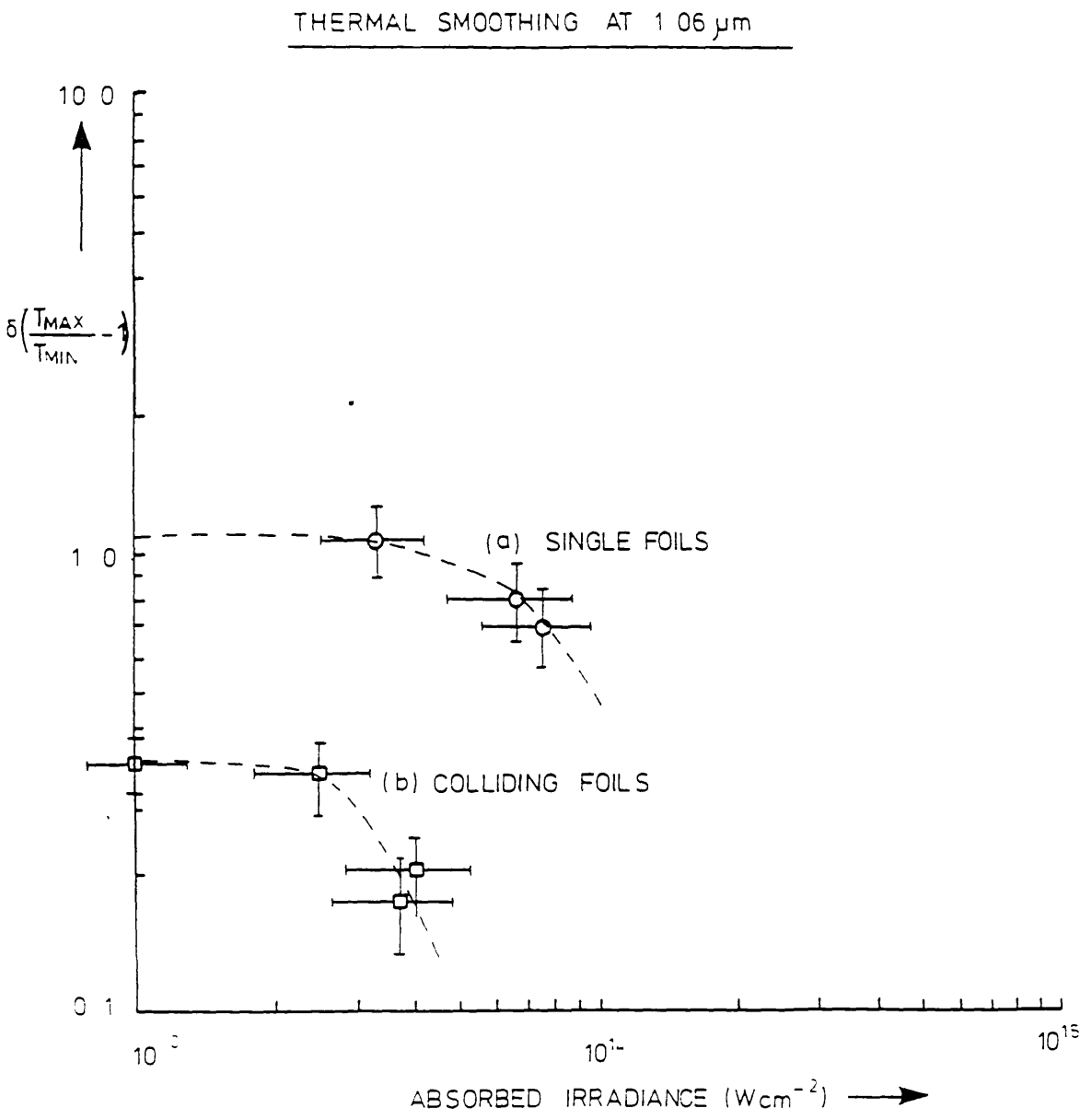

Fig.5.9 Variation of $\delta = (T_{max}/T_{min} - 1)$ at different absorbed irradiances for the case of (a) single foils - modulated shock transit technique and (b) double foils - modulated foil velocity.

of equivalent plane photographs for the case of (a) unmodulated and (b) modulated beam are shown in Fig.5.8. The peak to peak modulation period and intensity modulation being measured as :

$$\lambda_p = 90\ \mu m \quad \text{and} \quad I_{max}/I_{min} = 4.3:1$$

The values of the smoothing parameter δ for different absorbed irradiances are plotted in Fig.5.9 for both the single and double foil targets.

5.7 Discussion

If no smoothing were taking place the depth of modulation in transit time, T, would be dependent on the scaling of irradiance, I, and pressure, P. If

$$P \propto I^{0.7} \quad (5.5,5.20)$$

In the case of the single foil targets, the absolute values of pressure derived from simple planar transit times has shown gross inaccuracy in section 2.4. The scaling of base transit time and pressure (as measured from step transit time) in that section followed an approximate relationship of

$$P \propto 1/T^2$$

This is also the relation for pressure and shock transit time for the double foil targets, if one neglects the shock transit time in the second foil (foil thickness $\sim 1\ \mu m$) and assumes the

first foil is under constant acceleration (see equation 5.1). For an irradiance non-uniformity of 4:1, this gives a zero 'smoothing' limit of ≈ 0.6. As can be seen in Fig.5.9. the single foil low irradiance limits are ≈ 1.0 and 0.4 respectively.

The low value of zero smoothing for the double foils could be accounted for by hydrodynamic smoothing contributions due to target decompression during a 'coasting' phase smoothing out the imposed target uniformity even when no plasma smoothing effects are significant.

The high value of zero smoothing for the single foils may be due to a combination of effects.

(i) The imposed irradiance uniformity in the target plane may be much greater than the EPM value of 4:1. To produce the observed zero smoothing the intensity modulation would have to be $\sim$ 6:1. Whilst some increase in non-uniformity due to focussing lens aberrations might be expected it would be unlikely to increase by > 50%.

(ii) The scaling of shock transit time, pressure and irradiance may not be as described above. The experimental data in Chapter 2 suggests a $P \propto 1/T^2$ and a $T \propto I^{0.6}$ relationship although this is for a different set of laser conditions. If these were valid a reduced scaling of $P \propto I^{0.5}$ would be necessary to yield the observed zero smoothing limit.

Despite the uncertainties in the zero smoothing limits a number of trends are apparent from the data :

(1) Both types of target show little/no smoothing

at low irradiance (less than 3×10^{13} Wcm^{-2}) and smoothing increases (δ reduces) for increase in irradiance.

(2) The values for δ are much smaller, i.e. larger smoothing for the double foil targets than for the single foils and the smoothing increases as a function of laser irradiance more rapidly than for the single foils.

Tentative trajectories for the smoothing rates are indicated by dotted lines in Fig.5.9. (1) is interpreted as evidence of lateral spreading of energy occurring in the stand-off distance. (2) would be consistent with hydrodynamic decompression effects in the accelerated foil. Such effects have been observed and predicted by code simulations by other workers(5.13). The foil is not constantly driven by the laser before it collides with the impact foil. When the laser power drops it enters a coasting phase and suffers decompression and buckling. Here mass flows between the high and low accelerated regions of the target, inevitably smoothing the profile of the first foil. The degree of smoothing inferred from the emission at the rear of the impact foil will therefore be a combination of plasma smoothing and hydrodynamic effects.

It is possible to calculate the likely coasting time of the first foil with some simple approximations : if there is negligible mass lost by material ablation; and the ratio of the first foil can be described by a constant acceleration, a, during the laser pulse duration, t_L, then

$$P = a \rho \Delta x \qquad 5.1$$

where ρ and Δx are the density and thickness of the acceleration foil respectively, the distance travelled S is given by

$$S = \rho a t_L 2 + a t_L \tau \qquad 5.2$$

where τ is the coasting time.

For a 6 μm foil with a 50 μm separation, $t_L \approx 1.5$ nsec, a laser irradiance of $I = 4 \times 10^{13}$ implies $P \approx 3$ Mbar(5.5) giving

$$\tau = 0.5 \text{ nsec}$$

This gives a total transit time (ignoring shock propagation time in 1.5 μm second foil) of ~ 2 nsec - broadly consistent with some of the minimum transit times in Table 5.2. This implies that 25% of the foil motion was spent in a coasting phase, adequate time for hydro-smoothing effects to occur.

The contribution of coasting could be reduced with a reduction in foil separation but such a reduction would introduce the possibility of significant preheating of the second foil as observed by some workers(5.21,5.22).

To screen the preheat from the second foil the first foil could be increased in thickness, but then increased irradiance would be required to accelerate the foil. For an accurate measurement the distance traversed by the first foil must be >> than the target thickness.

In this experiment target preparation techniques made it difficult to accurately reduce target separations. So the effect of target separation could not be investigated satisfactorily. Clearly further experiments are warranted, but the evidence from this comparative study suggests results using the colliding foil technique are not concomitant with a simple accurate measurement of plasma smoothing rates.

5.8 Conclusions

It is unequivocal that the double foil technique has shown evidence of hydrodynamic contributions to the smoothing rates measured. Under identical laser conditions a modulated shockwave transit technique has inferred significantly reduced degrees of smoothing. Such a technique would then seem better placed to measure plasma smoothing effects in a subsequent quantitative study.

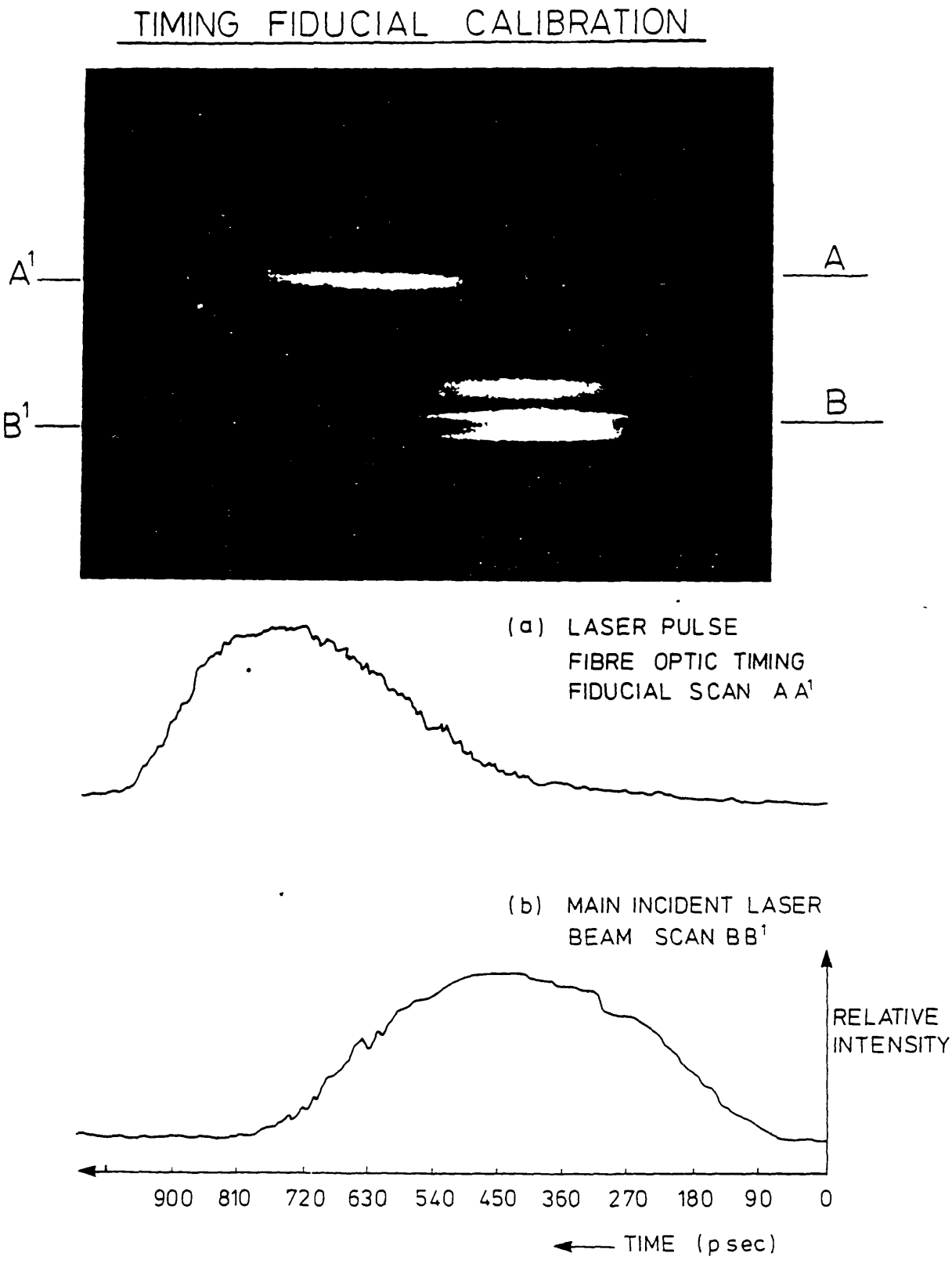

Fig.5.10 Optical streak photograph and microdensitometer tracings showing the calibration of the laser beam fiducial.

5.9 Single foil smoothing measurements at 0.35 μm

Two further experiments were performed using a single beam of the VULCAN system, frequency tripled by KDP* crystals to produce up to 24 J of 0.35 μm radiation in a pulse of either 500 psec or 700 psec FWHM duration. The experimental arrangement was identical to the previous experiment (fig.5.5) but using an f1.5 aspheric doublet to give a 150 μm focal spot on target. The targets were 20-25 μm thick aluminium vacuum deposited onto kcl substrates and then washed off and mounted on rectangular mounts mms in extent. Improved imaging efficiency of the targets was achieved with an f1.2 achromatic 50 mm camera lens positioned in its focal plane. Re-imaging was with an 167 cm air spaced achromat lens onto a 200 μm wide streak camera slit of a Hadlands 675 IMACON streak camera. Protection of the S20 photocathode from scattered laser light was with GG375(5.23) blue blocking absorption filters. The latter experiment also utilised a lens mounted light exclusion cone to avoid the significant intra-chamber spurious reflections. A temporal reference was again imaged via a fibre optic, but its source was a fraction of the incident 0.35 μm pulse. An example is shown in Fig.5.10. The target to image plane magnification was accurately measured using a glass microballoon of known size and the streak camera in focus mode of operation (see Fig.5.11). This gave the camera a field of view of 200 μm in the target plane. The static spatial resolution was estimated at 10 μm and the dynamic resolution at 10 psec.

As in the previous experiment the beam modulations were 2 cm wide strips of neutral density filter chosen to give an

Fig.5.11 A static optical streak photograph of a glass microballoon showing the spatial resolution and magnification calibration of the streak camera.

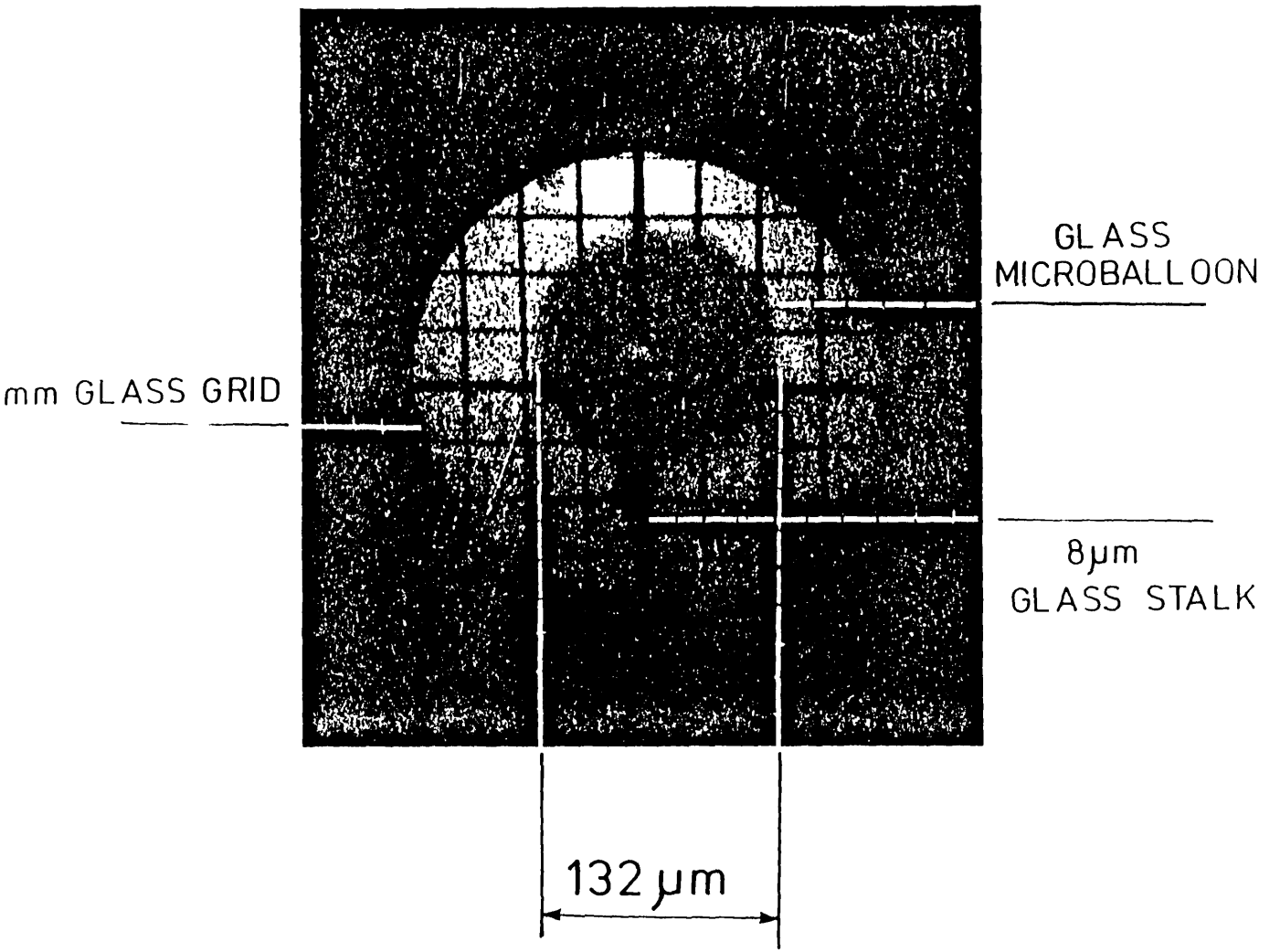

THERMAL SMOOTHING RESULTS AT 0.35 μm

TABLE 5.3

Shot no.	T_{min} (psec)	T_{max} (psec)	$T_{max}/T_{min} - 1$	Focal Spot (μm)	Energy (J)	Absorbed Irradiance $/10^{13}$ Wcm^{-2}
% Error	± 6	± 7	± 13	± 15	± 10	± 40
0220483	340	590	0.74	120	10.7	17.1
0420483	420	650	0.55	120	21.0	33.3
0720483	495	720	0.45	120	21.0	33.3
1020483	375	780	1.08	120	12.0	19.1
1127483	510	780	0.53	150	16.5	16.8
1327483	480	UNMODULATED		120	13.8	22.0
1727483	550	790	0.44	150	19.5	19.9
1827483	490	840	0.71	130	14.8	20.0
0328483	490	740	0.51	130	13.7	18.5
0628483	360	630	0.75	130	14.4	19.5
0820483	510	780	0.53	120	12.0	19.1
0928483	390	640	0.64	120	9.0	14.3
1528483	390	740	0.90	150	12.6	12.8
2228483	370	610	0.65	120	13.3	21.1
2428483	260	540	1.07	120	10.0	15.9
0229483	270	440	0.63	110	16.5	31.2
0429483	360	520	0.44	120	20.0	31.9
0529483	380	690	0.81	120	14.9	23.7
0729483	315	540	0.71	130	15.0	20.3
0829483	350	575	0.64	130	16.2	22.0

THERMAL SMOOTHING RESULTS AT 0.35 μm

TABLE 5.4

Shot no.	T_{min} (psec)	T_{max} (psec)	$T_{max}/T_{min} - 1$	Focal Spot (μm)	Energy (J)	Absorbed Irradiance $/10^{13}$ Wcm^{-2}
% Error	± 6	± 7	± 13	± 15	± 10	± 30
0511082	460	780	0.69	150	23.0	16.7
0711082	300	UNMODULATED		150	22.0	16.0
0811082	430	905	1.10	150	21.0	15.2
1011082	350	730	1.09	150	17.0	12.3
1111082	550	1045	0.90	150	19.0	13.9
12111082	350	730	1.08	150	12.0	8.7
14111082	440	820	0.87	150	18.0	13.0
18111082	395	890	1.25	150	8.0	5.8
1428982	215	530	1.40	150	12.0	8.7

approximate intensity modulation of I_{max}/I_{min} 4:1 and spatial period of $\sim$90 μm.

Improved monitoring of the laser beam intensity profile was achieved with an additional equivalent plane monitor (EPM). EPM1 was obtained by splitting off a fraction of the incident beam before it reached the main focussing lens. EPM2 was obtained by placing a 50/50 cube beam splitter in the optical path 10 cm before the streak camera slit plane. Low power (mJ) laser shots were then fired through the target chamber (as on a timing fiducial shot) and the intensity pattern compared with EPM1 and the corresponding streak record. As in the previous experiment the laser irradiance was varied with a constant focal spot size and the modulation in shockwave transit time used to infer a degree of smoothing.

5.10 Results

Optical streak photographs of the rear surface of the targets for unmodulated and modulated beams were similar to those recorded previously, as shown in Fig.5.7. The values of maximum and minimum shock transit times recorded are shown in Tables 5.3 and 5.4. Also tabulated are the shot numbers, laser energy and focal spot size and the smoothing parameter δ, as defined previously, i.e.

$$\delta = \frac{T_{max}}{T_{min}} - 1$$

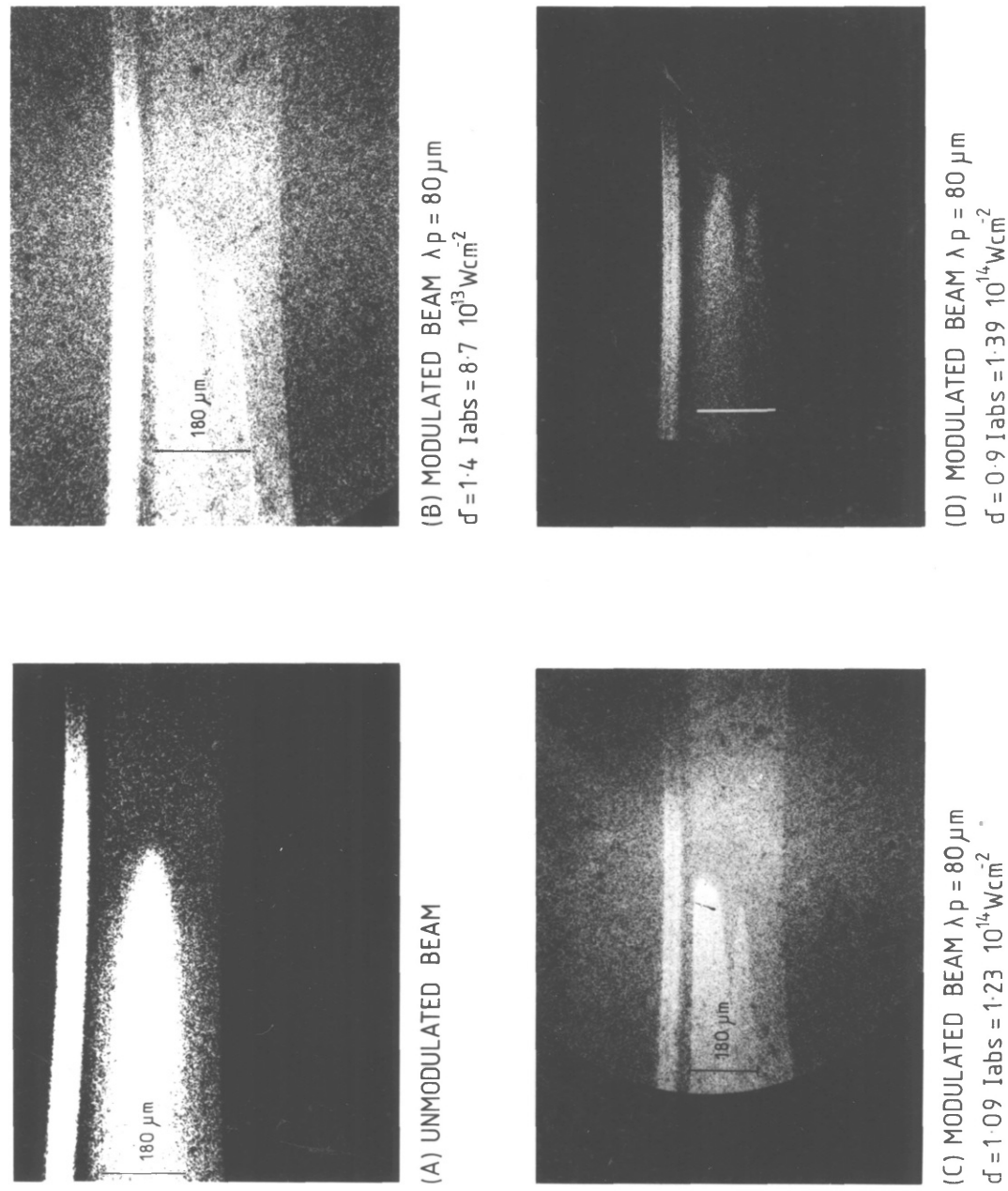

Fig.5.12 A selection of four optical streak photographs from the rear of a 25 µm aluminium foil for the case of (a) unmodulated beam, (b), (c), and (d) modulated beam (λ_p = 80 µm).

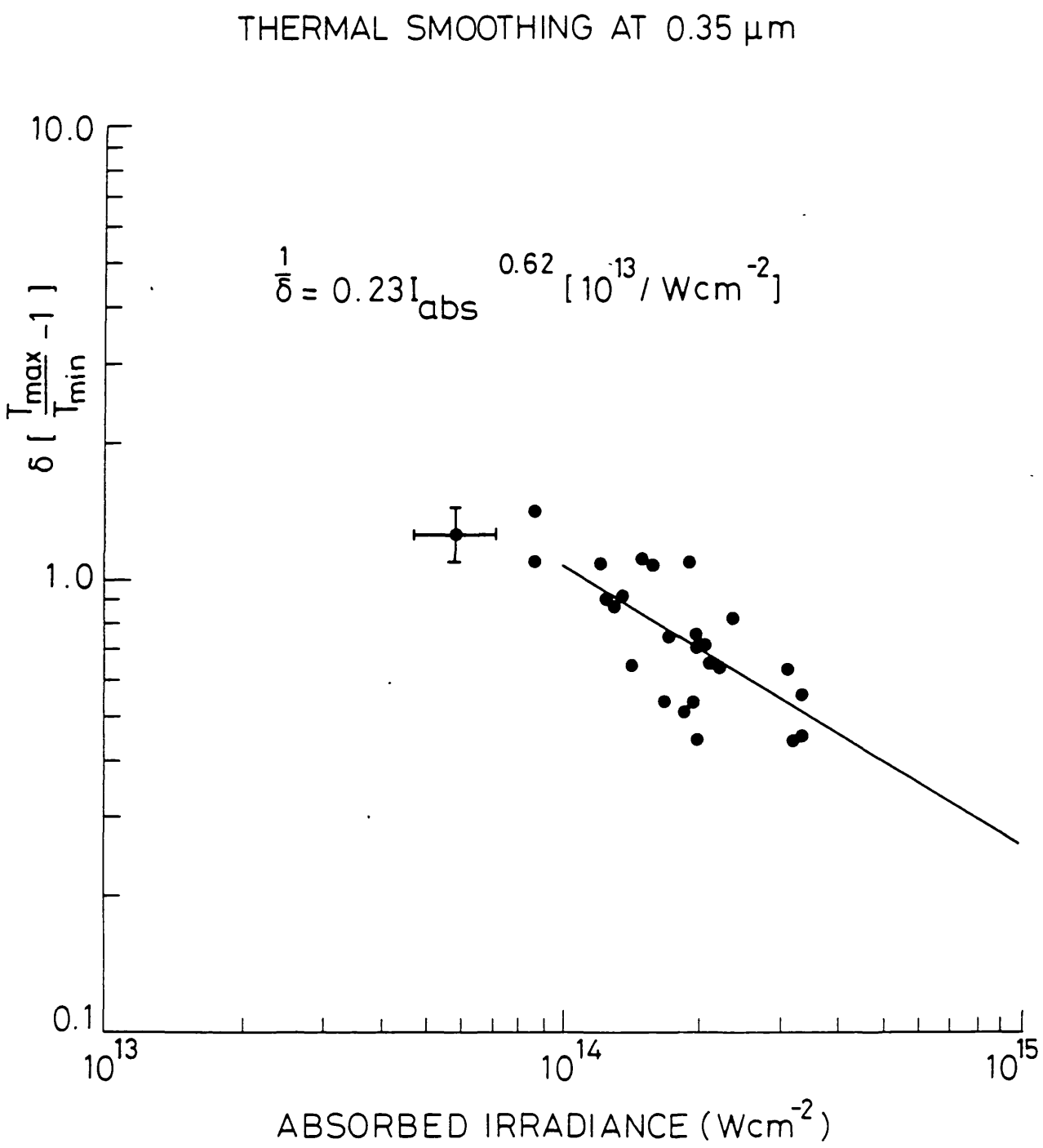

Fig.5.13 The variation of δ (= T_{max}/T_{min} - 1) as a function of absorbed irradiance at a laser wavelength of 0.35 µm.

The sizes of the images in the optical streaks are consistent with the focal spot sizes and target to film plane magnification. A selection of four optical streaks for an unmodulated beam case and modulated beam (period λ_p = 80 μm, I_{max}/I_{min} = 4:1) at three different irradiances are shown in Fig.5.12. The degree of smoothing (1/δ) increases in the series (b) to (d) as the absorbed irradiance increases. The temporal scales in this figure can be estimated by comparing images (a) and (b) with Fig.5.11 (ii) and (i) respectively (the same shots).

The variation in δ and absorbed irradiance has been plotted in Fig.5.13. Sample error bars are indicated for one of the data points. The data gives the following empirical relationship :

$$\frac{1}{\delta} = 0.23 \pm 0.06 \quad I_{abs}^{0.62 \pm 0.14} \quad [/10^{13} \text{ Wcm}^{-2}]$$

There is little smoothing of the imposed beam modulation below 10^{14} Wcm^{-2} but increases slowly thereafter.

5.10.1 Equivalent plane monitoring

Diagnosis of the inhomogeneities present across the laser beam profile is conveniently made by splitting off a fraction of the incident beam and re-imaging through an auxilliary lens. This may be grossly inaccurate since the

F1.5 FOCUSSING LENS NON-UNIFORMITY SIGNATURE

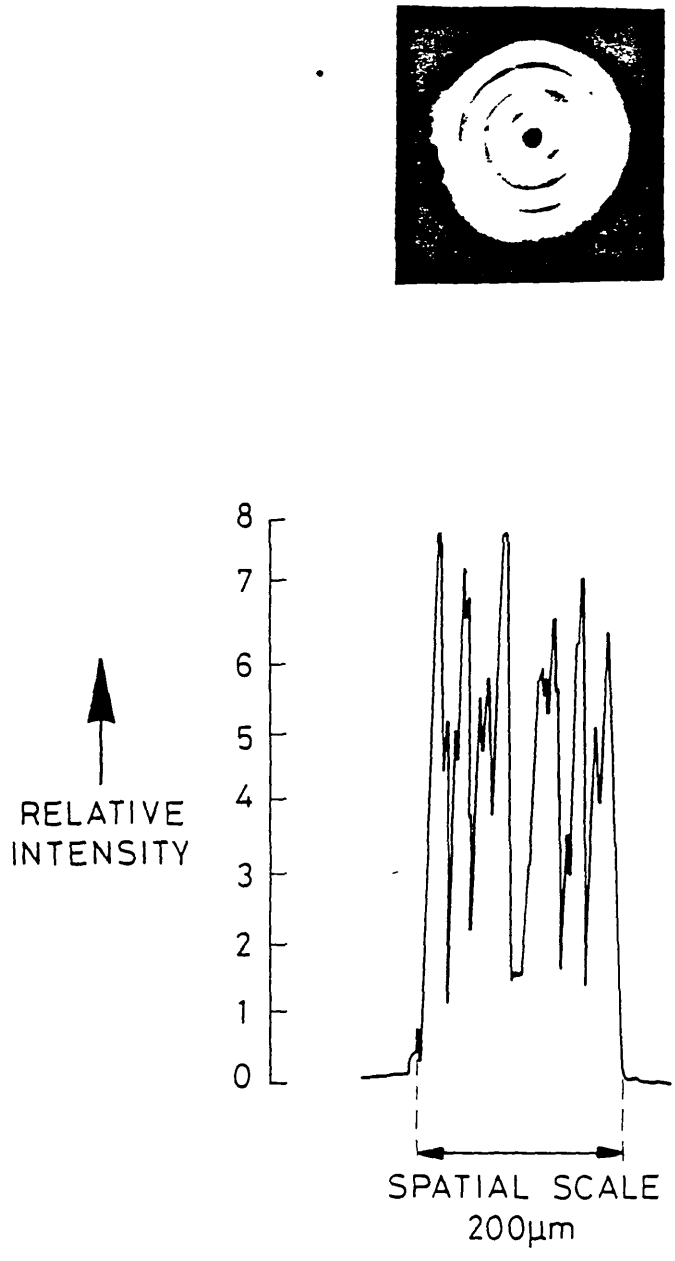

Fig.5.14 The non-uniformity signature of the main focussing lens from ref.(5.24).

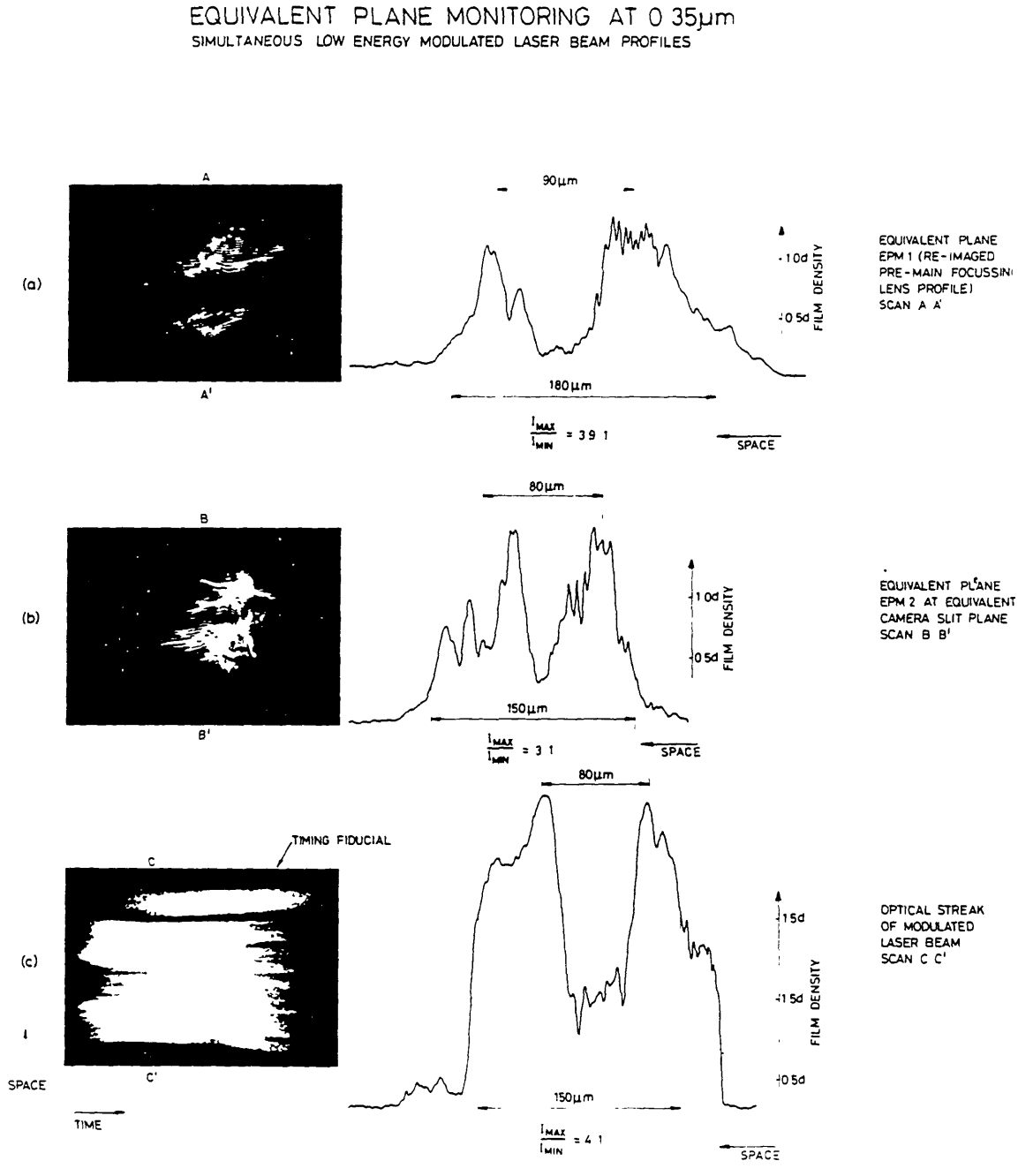

Fig.5.15 Examples of equivalent plane monitor records on the same low energy laser shot with an imposed beam inhomogeneity.

non-uniformities introduced by the main focussing lens are not included while the aberrations of the auxilliary lens are convolved in the equivalent plane image. The main focussing lens used in this experiment has been studied by some workers(5.24) and is shown in Fig.5.14. To ascertain the validity of a re-imaging EPM technique, two images, before the main focussing lens, and in the equivalent streak camera slit plane were recorded on a low energy laser shot.

In Fig.5.15, three images are shown for (a) before the main focussing lens (as normally recorded on a high energy data shot), (b) in the equivalent streak camera slit plane, and (c) optical streak image. The period of modulation is consistent through the three images with only a small deviation of intensity ratio. On high energy shots it is not possible to record the same series of EPMs due to the danger of component damage. Such shots would have additional beam non-uniformity due to disc amplifier ring patterns(5.25) - no vacuum spatial filters were used in the VULCAN system at this time.

The low power shots demonstrate that both the maximum and minimum beam intensity and the spatial scalelengths measured in the re-imaged EPM offer a reasonable representation of those presented to the target plane, although only an accurate record of target plane non-uniformity on every shot would give complete confidence.

5.11 Discussion

As with the single foil results at λ_L = 1.06 μm in section 5.7, the observed low irradiance smoothing limit is

anomalously high at $\sim$ 1.2. Again this is likely to be caused by a combination of pressure, irradiance and transit time scaling as discussed previously.

There is considerable scatter apparent in the data in Fig.5.13. It is tempting to partly attribute this to the slight difference in laser pulse length and target thickness (700 and 500 psec FWHM and 21-25 μm Al) but this is not borne out by the respective values which show no systematic differences.

Some of the data did suffer from an increased uncertainty (an additional 10%) in laser irradiance due to target area laser problems[5.26] which may go some way to account for the high degree of scatter.

5.12 Comparison with previous results, simulations and analytical models

As discussed in section 5.2 the degree of smoothing is dependent on the stand off distance D(t) which is itself a complicated time dependent function and varies for laser wavelength and irradiance I. Simulations[5.7] have shown that if a constant laser irradiance is applied at t = 0 the separation D(t) is initially described by :

$$D(t) = v_s t \qquad 5.3$$

where v_s is the velocity of separation. This transient value of D saturates at a steady state value which is given by Gardner and Bodner[5.2] as :

$$D_\infty \propto (I/10^{13}\ \mathrm{Wcm^{-2}}\ \lambda\ \mu m^{3.8})0.7 \qquad 5.4$$

As described by Key(5.7) the dynamics of the critical density surface motion can be divided into the transient and steady state phases by a transient fraction ε where for a laser pulse duration τ,

$$D = v_s\, t \qquad \text{where } 0 < t < \varepsilon\tau$$

and

$$D = D_\infty \qquad \text{where } \varepsilon t < t < \tau$$

To compare values for smoothing rates it is important therefore to know whether the measurements were made during a transient phase or when a largely steady state separation of critical density and ablation surface had been achieved. A convenient relation from Key(5.7) combines the Gardner and Bodner steady state value and velocity of separation to give the duration of the transient phase as

$$T_s = \frac{D_\infty}{V_s} = 4.7 \times 10^{-9}\, I^{0.37}(/10^{13}\ \mathrm{Wcm^{-2}})\lambda^2\ (/\mu m)\frac{R_{mm}}{R_m+1} \qquad 5.5$$

Inserting the values for these measurements, R = 75 μm, λ = 0.35 μm, and values of irradiance as 10^{14} - 3 10^{14} $\mathrm{Wcm^{-2}}$ suggests the duration of the transient phase varied from

T_s = 90 psec - 140 psec

The measurements made by shock transit time inherently describe a time integrated smoothing process which acts from t = 0 to the minimum and maximum shock transit times. The shock transit times were typically $\sim$ 300 psec and therefore suggest that a steady state smoothing situation had been achieved.

The measurements of Cole (see Fig.5.3) which were thought to be in a largely steady state phase but were suspected to include significant hydro smoothing contributions gave

$$\frac{1}{\Delta} = 0.37 \, (I_a \, \lambda_L^2)^3 \quad .$$

It is not possible to comment on the wavelength scaling since no accurate data at other wavelengths has been recorded here. However the scaling from Cole suggests levels of smoothing much higher than those measured here with the shock transit time. Some decompression and buckling effects were conceded in the work which would account for the higher smoothing rates.

The 2-d simulations of Cole gave a scaling of smoothing when expressed in terms of the non-uniform target motion as :

$$\frac{1}{\Delta} = 2.7 \, I_a^{0.9} \, \lambda_L^{1.8}$$

This is a little stronger than the measurements obtained with the shock transit time. However, some simulations were performed in an attempt to infer levels of smoothing at early times before target acceleration effects became significant. These simulations were made at 200 psec and were expressed in the form of the non-uniformity in pressure caused by the non-uniform irradiation.

$$\left(\frac{P_{max}}{P_{min}} - 1\right)^{-1} \propto I^{0.67}\ \lambda^{1.4} \qquad 5.6$$

Since the distance travelled by the target is proportional to the pressure this suggests that the smoothing also scales as

$$\frac{1}{\Delta} \propto I^{0.67}\ \lambda^{1.4}$$

which compares with the shock transit time measurement (also taken at earlier times before target motion can contribute) as

$$\frac{1}{\Delta} \propto I^{0.62}$$

Here the agreement is good and suggests that if valid X-ray shadowgraphy measurements were able to have been made early in time good agreement between the degree of smoothing inferred from target non-uniformity and shock transit time non-uniformity may have been found.

Further agreement of the power of 0.6 - 0.7 is found with the previously mentioned Gardner and Bodner simulation of the steady state separations D_∞ (equation 5.4)

$$D_\infty \propto I_a^{0.7} \lambda^{3.8}$$

A useful analytical model has been used(5.2) which describes the non-uniformity in the pressure and irradiance and a smoothing factor f by

$$\frac{\Delta p}{p} = f \frac{\Delta I}{I}$$

for simple diffusion

$$f = \exp\left(\frac{-2\pi D}{L_p}\right)$$

TABLE 5.5

Target (μm)	Shot no.	V_{min} (μmns^{-1})	V_{max} (μmns^{-1})	P_{min} (Mbar)	P_{max} (Mbar)	$P_{max}/P_{min} - 1$	Absorbed Irradiance $/10^{13}$ Wcm^{-2}
Aluminium	% Error	± 25	± 25	± 25	± 25	± 50	± 30
10	0220483	17	30	4.2	16.5	2.9	17.1
20	0420483	31	48	17.0	40.3	1.4	33.3
20	0720483	28	40	14.1	29.6	1.1	33.3
20	1020483	26	53	11.9	47.0	2.9	19.1
20	1127483	27	41	13.0	31.0	1.4	16.8
21	1327482	UNMODULATED	44	-	35.0	-	22.0
21	1727483	27	38	13.0	26.9	1.07	19.9
21	1827483	25	43	10.9	33.6	2.08	20.0
21	0328483	28	43	14.1	33.6	1.38	18.5
21	0628483	33	58	20.5	53.6	1.61	19.5
21	0828483	27	41	13.0	31.0	1.38	19.1
21	0928483	33	54	20.5	48.3	1.35	14.3
21	1528483	28	54	14.1	48.3	2.4	12.8
25	2228483	46	68	37.6	67.0	0.78	21.1
21	2428483	39	80	28.4	82.9	1.9	15.9
21	0229483	40	78	29.3	80.3	1.74	31.2
25	0429483	48	69	40.3	68.3	0.69	31.9
25	0529483	36	66	24.4	64.3	1.63	23.7
25	0729483	46	79	37.6	81.6	1.67	20.3
25	0829483	43	71	33.5	70.9	1.11	22.0

TABLE 5.6

Target (μm)	Shot no.	V_{min} (μmns^{-1})	V_{max} (μmns^{-1})	P_{min} (Mbar)	P_{max} (Mbar)	$P_{max}/P_{min} - 1$	Absorbed Irradiance /10^{13} Wcm^{-2}
Aluminium	% Error	± 25	± 25	± 25	± 25	± 50	± 30
25	0511082	32	54	19.0	48	1.5	16.7
25	0711082	UNMODULATED	71				16.0
25	0811082	27	58	13	52	3.0	15.2
25	1011082	34	71	22	71	2.2	12.3
25	1111082	24	45	8	36	3.5	13.9
25	1211082	34	71	22	71	2.2	8.7
25	1411082	30	57	16	53	2.3	13.0
25	1811082	28	63	14	60	3.3	5.8
20	1428982	38	93	27	100	2.7	8.7

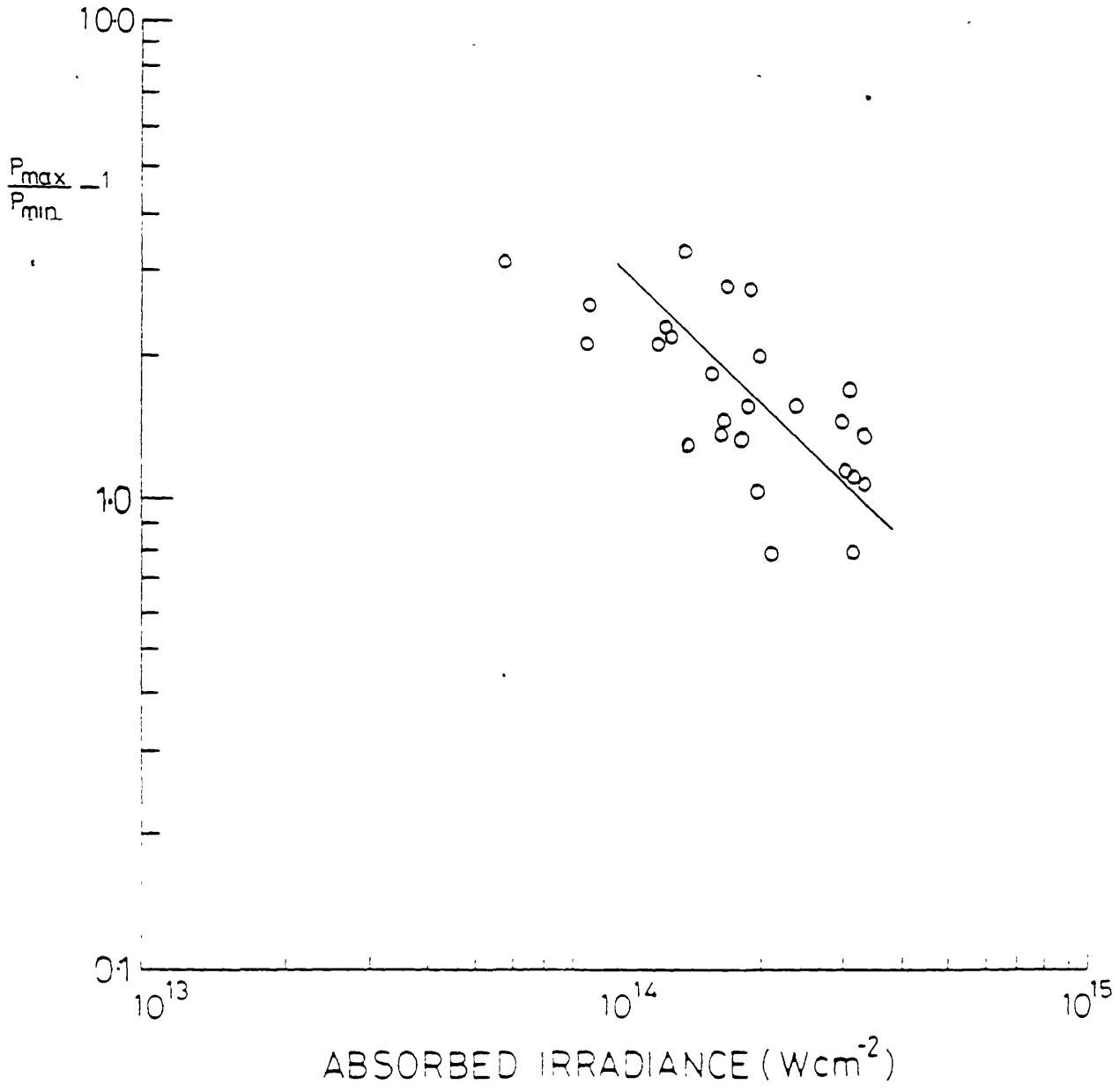

Fig.5.16 The variation of $P_{max}/P_{min} - 1$ inferred from shock transit times as a function of absorbed irradiance.

where L_p is the wavelength of the modulation. This value is now thought to be invalid(5.3,5.8) and recent more detailed work(5.8) has suggested that a larger smoothing exponent of $(-4\pi D/L_p)$ is more accurate. It is interesting therefore to investigate tentatively the values of pressure and the pressure non-uniformity inferred from the maximum and minimum shock transit times and EOS data for aluminium.

As discussued earlier there will be considerable inaccuracy when inferring values of pressure from the planar transit times, however, the values and scaling of the pressure non-uniformity $P_{max}/P_{min} - 1$ may still yield valid conclusions. Tables 5.5 and 5.6 tabulate the values of shock velocity inferred from the transit time, shock pressures from EOS, data for aluminium(5.27) and pressure non-uniformity ratio $P_{max}/P_{min} - 1$. In Fig.5.16 the variation of $P_{max}/P_{min} - 1$ is plotted as a function of absorbed irradiance.

Large scatter is again evident, however the data fits an approximate empirical relationship of:

$$\frac{P_{max}}{P_{min}} - 1 \propto I_{abs}^{0.98}$$

The degree of smoothing f inferred from the pressure non-uniformity and the fixed irradiance non-uniformity (using the measured $I_{max}/I_{min} = 4:1$) gives values of

$f = 0.65$ at 10^{14} Wcm^{-2} at the onset of smoothing

TABLE 5.7

A COMPARISON OF THE EXPERIMENTAL SMOOTHING FRACTION $f = \frac{\Delta P_1}{P} / \frac{\Delta I}{I}$ WITH AN ANALYTICAL MODEL USING A SIMPLE DIFFUSION AND AN ENHANCED SMOOTHING EXPONENT

Absorbed Irradiance (Wcm^{-2})	$f = \frac{\Delta P}{P} / \frac{\Delta I}{I}$ Experiment	$f_1 = \exp(-\frac{2\pi D_\infty}{LP})$ Model 1	$f_2 = (-\frac{4\pi D_\infty}{LP})$ Model 2
1×10^{14}	0.65	0.83	0.63
3×10^{14}	0.33	0.62	0.36

to

$$f = 0.33 \quad \text{at} \quad 3 \times 10^4 \ \text{Wcm}^{-2}$$

This can be compared with the values inferred from the function

$$f_{\text{mod 1}} = \exp\left(\frac{-2\pi D}{L_p}\right) \quad \text{and} \quad f_{\text{mod 2}} = \exp\left(\frac{-4\pi D}{L_p}\right)$$

If a steady state value of D_∞ is assumed using equation 5.4 and putting L_p = 80 μm, this gives values of

$$f = 0.65 \quad \text{at} \sim 10^{14} \ \text{Wcm}^{-2} \ \text{at the onset of smoothing}$$

to

$$f = 0.33 \quad \text{at} \sim 3 \times 10^{14} \ \text{Wcm}^{-2}$$

Table 5.7 tabulates the values of the smoothing function f from the experiment and from the analytical model with both the simple diffusion exponent and the enhanced smoothing exponent for the two values of laser irradiance. As can be seen from the table, if a steady state saturation has been achieved the shock transit time smoothing measurements made here tend to

favour the revised analytical smoothing model exponent of $(-4\pi D/L_p)$.

5.13 Conclusions of Chapter Five

Comparative measurements of the degree of smoothing of imposed laser beam inhomogeneities at 1.06 μm using a colliding foil and a modulated shock transit time technique have been made. These results suggested that the modulated shockwave transit technique is able to make measurements of smoothing processes which occur early in time (sub nsec) before target acceleration effects can contribute. The first systematic measurements of the smoothing of imposed laser beam inhomogeneities as a function of laser irradiance at a wavelength of 0.35 μm have been presented. The degrees of smoothing are possibly the first measurements which accurately reflect the degree of 'plasma' smoothing as distinct from those due to target acceleration effects.

Good agreement is found with both 1-d simulations of the scaling of the steady state critical density to absorption region separation and with 2-d simulations if the degree of smoothing is measured before target acceleration effects contribute. Furthermore agreement is reached with an analytical model of smoothing which uses an enhanced smoothing factor described by $\exp(-4\pi D_\infty/L_p)$ where D_∞ is the steady state separation of critical to ablation surface from Gardner and Bodner(5.2).

Clearly much work is required to make confident

predictions as to the degree of non-uniformities which can be smoothed by the 'plasma' effects between the absorption and ablation regions. The type of further studies required will be discussed in Chapter Six, however with respect to 0.35 μm radiation, future experiments are likely to be able to measure higher degrees of smoothing with much greater accuracy. The results recorded here were fraught with uncertainties with the modest laser irradiances available. The new upgraded VULCAN system with the greatly increased laser power is well placed to embark on smoothing measurements employing 0.35 μm radiation.

CHAPTER SIX

SMOOTHING MEASUREMENTS AT 0.35 μm USING X-RAY SHADOWGRAPHY

6.1 Abstract

Measurements of the smoothing of imposed laser beam inhomogeneities are described using short pulse X-ray shadowgraphy. The degree of smoothing has been calculated from the trajectories of non-uniformly accelerated 12.5 and 25.0 μm thick mylar microdiscs, driven by 500 psec FWHM pulses of 0.35 μm radiation. Uncertainties in the focussing conditions have made the smoothing-irradiance scaling tentative, but some evidence of significant smoothing with a reduced wavelength (λ_p = 50 μm) of modulation is found. A critical comparison of the smoothing data obtained at 1.06, 0.53 and 0.35 μm to date[6.1-6.5] is undertaken.

6.2 Introduction

Experiments to measure smoothing of imposed beam inhomogeneities have been described in Chapter Five. Short pulse X-ray shadowgraphy studies have only been performed at 1.06 and 0.53 μm[6.2,6.3], although the technique has been used at 0.35 μm to observe the effect of a high z radiative heating

layer on non-uniformly irradiated targets(6.6). The purpose of this experiment was to measure the degree of smoothing as a function of laser irradiance at 0.35 μm, using beam non-uniformities of shorter wavelength than previous studies. Since the degree of smoothing under steady state conditions is dependent on a factor $\exp(-4\pi D_\infty/\lambda_p)$ (see section 5.12) a reduced λ_p allows experiments to probe a regime in which significant smoothing might be expected to occur. Measurement of these higher degrees of smoothing with larger λ_ps being prevented by the much higher irradiance required (to achieve the same degree of smoothing) which at λ_L = 0.35 μm, has not been attainable with the VULCAN laser system. The data obtained would also serve as a comparison with the modulated shock transit measurements obtained in Chapter Five. The conditions of target thickness, material and laser parameters have been chosen to reduce the contribution from target acceleration effects which were a feature of previous shadowgraphy measurements.

6.3 Experimental

In this experiment two beams of the VULCAN Nd. glass laser were utilised, a main drive beam of 0.35 μm radiation (500 psec FWHM duration) to irradiate a microdisc target, with a second 1.06 μm beam (100 psec FWHM duration) to provide a source for short pulse X-ray shadowgraphy, diagnosing the motion of the target. The basic arrangement is shown in Fig.6.1.

The 10 cm diameter drive beam was focussed down with an f1.5 aspheric doublet lens to produce 130 μm FWHM focal spots onto mylar microdisc targets. The microdiscs, mounted on 10 μm

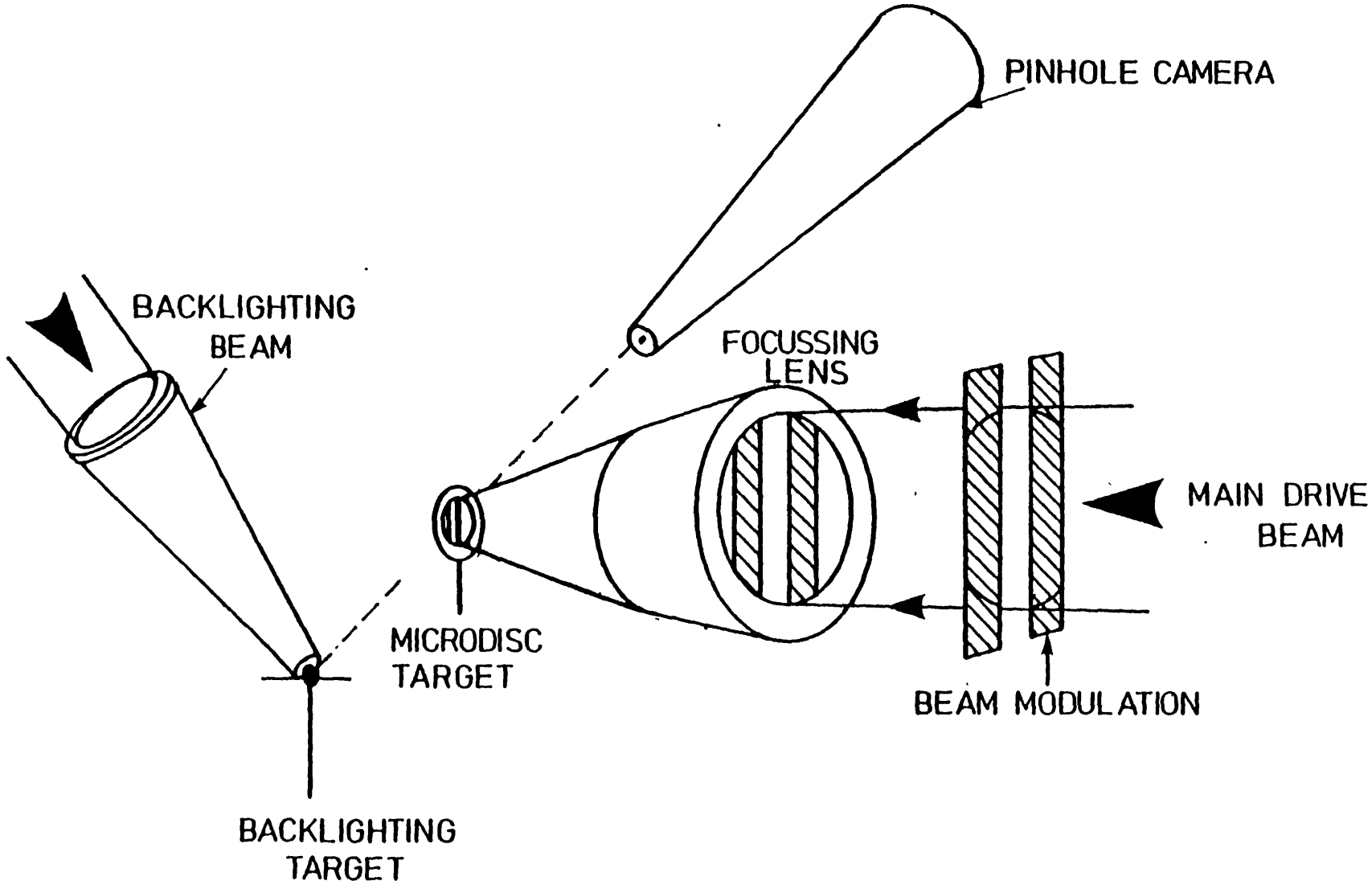

Fig.6.1 Experimental arrangement to measure the smoothing of imposed beam non-uniformities on accelerated microdiscs using short pulse X-ray shadowgraphy.

carbon fibre stalks were 270 μm in diameter and 12.5 or 25 μm thick. A typical target is shown in Fig.6.2.

Mylar was chosen as the target material to minimise the amount of X-ray self emission produced by the ablation plasma during irradiation by the drive laser pulse. (The efficiency of X-rays produced by Bremsstrahlung increases with target material atomic number(6.7)).

The targets were viewed side on by an X-ray recording pinhole camera(6.8) equipped with a 5 μm platinum pinhole filtered with 3 μm aluminised mylar giving a 1/e cut off of 1.2 keV and nominal spatial resolution of 8 μm. The camera consisted of the pinhole arrangement with a P11 phosphor to detect the $\sim$ 1 keV X-rays relayed to a Hadlands 50/40 image intensifier onto Ilford HP5(6.9) fast recording film.

The motion of the accelerated targets was shadowed by backlighting the microdiscs with a short pulse of X-rays produced by irradiating a separate bismuth target with a 100 psec FWHM pulse of 1.06 μm radiation.

The backlighting targets were prepared by vacuum depositing a 1 μm layer of bismuth onto 25 μm mylar substrates.

X-ray emission from the backlighting target was observed with an X-ray streak camera and found to have a FWHM of 100 psec. Using an optical streak camera the main and backlighting beams were timed to be coincident. A 200 psec delay (with respect to the peak of the drive pulse) was imposed on the backlighting beam so that the targets were shadowed approximately at the end of the laser pulse. This insured that the observations were made during the steady state phase and

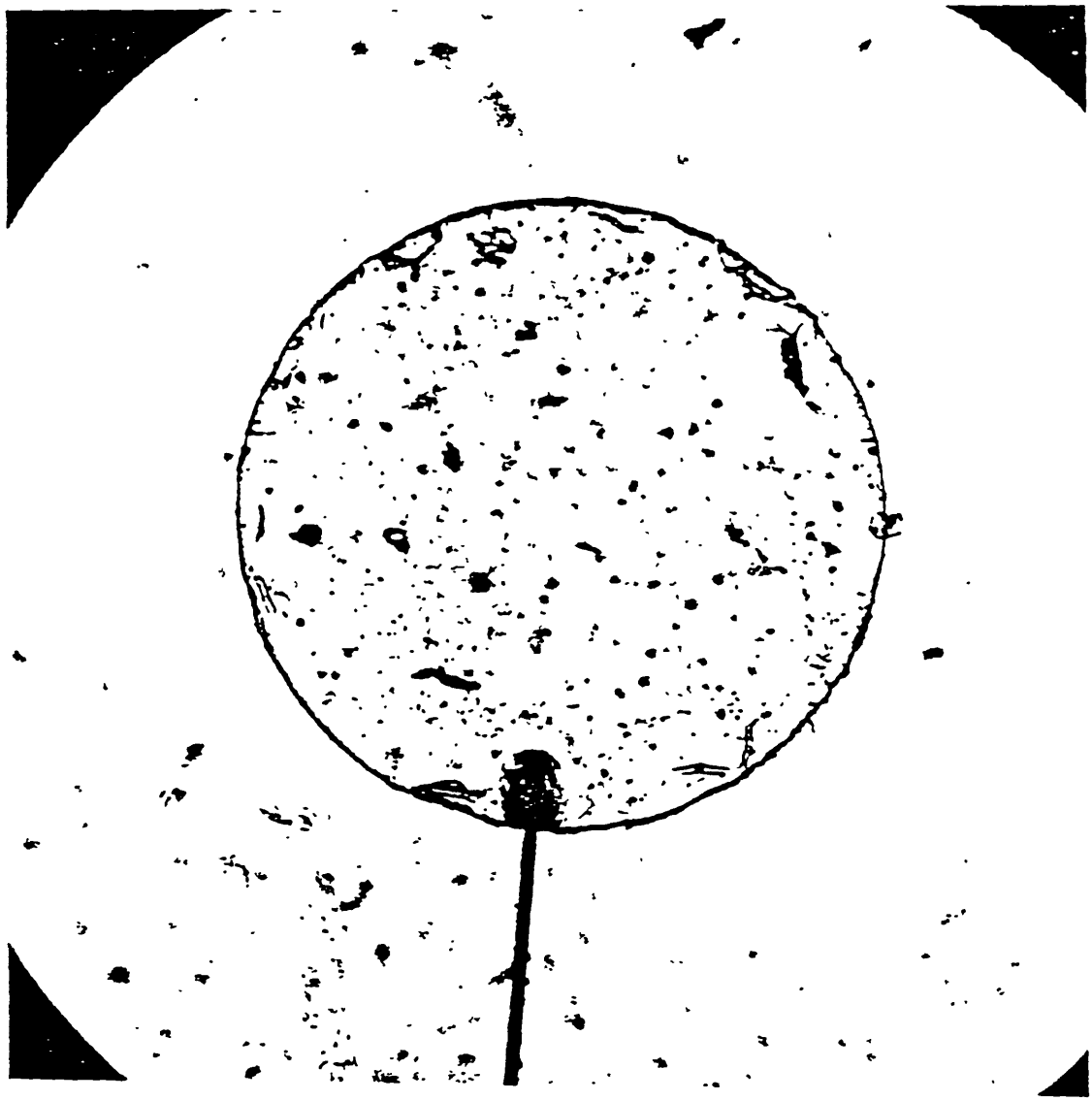

Fig.6.2 Microscope photograph of a typical mylar microdisc target.

before the end of the irradiation while the target was still being driven.

When viewed side-on the 270 μm diameter targets were opaque to the 1.2 keV probing X-rays, which have an attenuation length of 30 μm in cold (unirradiated) mylar[6.10]. In Fig.6.3(a) a shadowgram of an unirradiated disc is shown with a 25 μm FWHM shadow consistent with the microdisc thickness. Shots of irradiated discs with no backlighting beam showed emission from the mylar of much lower intensity and present only on the irradiated side of the target.

The near field of the drive laser beam was modulated by inserting strips of 10 mm wide neutral density filter in the 108 mm diameter beam. The spatial fill factor of the beam (the fraction of the beam area within which 90% of the energy is contained) was measured from near field pictures of the beam to be ≈ 0.5. The filters (Eastman Kodak gelatin substrate type) were chosen to give an intensity modulation ratio of $\approx 3:1$ and a spatial wavelength of ~ 50 μm (consistent with the conditions for significant smoothing at 0.35 μm at mid. 10^{14} Wcm^{-2}[6.11]). Equivalent plane photographs were taken using an f50 lens to relay a fraction of the incident beam onto type 56 positive/negative Polaroid film. Using the density-exposure calibration curve for the film[6.12] microdensitometer tracings measured the intensity modulation ratio and periodicity.

Fig.6.4 shows an equivalent plane photograph and densitometer tracing showing the measured intensity modulation and spatial period.

The targets were shadowed at a constant backlighting

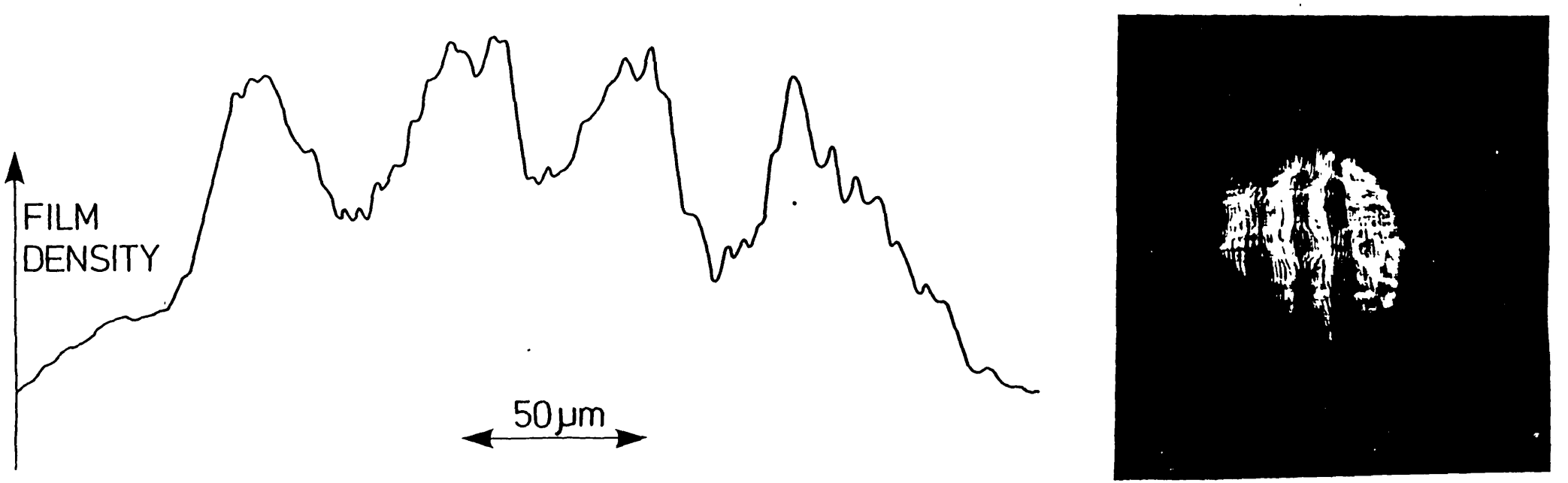

Fig.6.4 Equivalent plane photograph and microdensitometer tracing across the beam of a modulated laser beam profile (modulations orientated vertically in the photo) showing a period and intensity modulation of λp = 50 μm and I_{max}/I_{min} = 3:1 respectively.

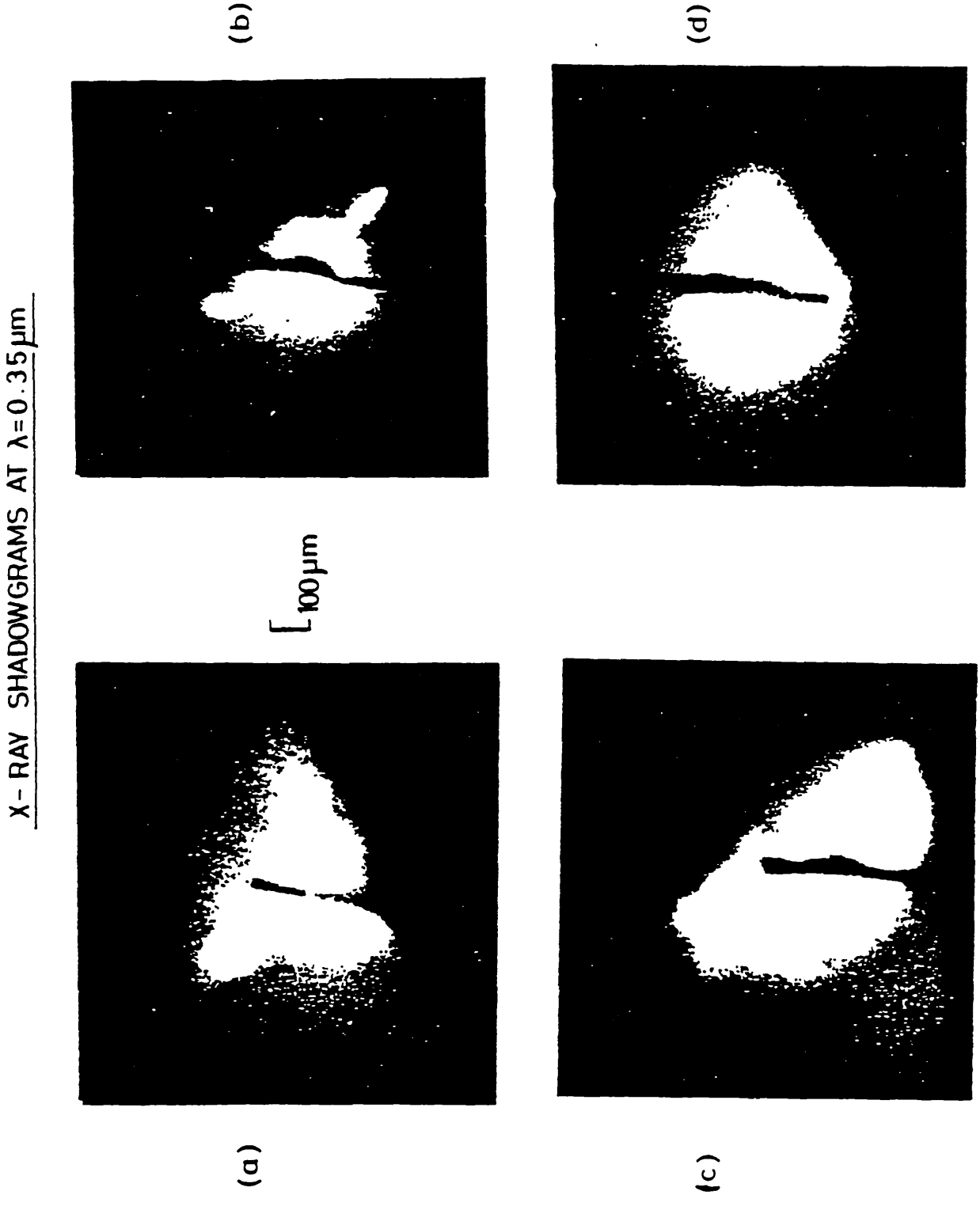

Fig.6.3 A selection of four X-ray shadowgraphs of a non-uniformly accelerated microdisc shadowed at a constant time.
(a) unirradiated target
(b) $\Delta = 1.2$ $I_{abs} = 8.2 \times 10^{13}$
(c) $\Delta = 0.6$ $I_{abs} = 9.2 \times 10^{13}$
(d) $\Delta = 0.43$ $I_{abs} = 1.1 \times 10^{14}$ Wcm^{-2}

delay time for a range of laser irradiances, obtained by varying the laser energy with a constant focal spot size.

6.4 Results

X-ray shadowgrams for four different shots are shown in Fig.6.3. (a) is an unirradiated target, (b), (c), and (d) are examples of different values of laser irradiance. The degree of smoothing is inferred from microdensitometry across the high and low drive regions of the target., In the case of there being a number of driven regions an average value was taken.

The distance modulation parameter is defined by

$$\Delta = \frac{\text{maximum distance travelled}}{\text{minimum distance travelled}} - 1 = \frac{Z_{max}}{Z_{min}} - 1$$

The results are tabulated in Table 6.1. The laser energy values have been corrected to compensate for beam modulation absorption in target area calorimetry (consistent with previous shadowgraphy results where a separate beam was used to obtain equivalent plane monitoring). Absorption fractions were used as Key et al[6.13]. The variation of Δ as a function of absorbed irradiance is plotted in Fig.6.5 for the two target thicknesses 12.5 μm and 25 μm mylar. If no smoothing were present the target modulation would depend only on the depth of pressure modulation on the ablation front. As in Chapter Five, if the pressure and irradiance scale as

TABLE 6.1

X-RAY SHADOWGRAPHY SMOOTHING MEASUREMENTS AT λ_L = 0.35 μm

Shot no.	Target (μm)	Focal Spot (μm)	Energy (J)	Z_{max} (μm)	Z_{min} (μm)	$Z_{max}/Z_{min} - 1$	$I_{abs}/10^{13}$ (Wcm^{-2})
% Error	± 5	± 20	± 10	± 10	± 10	± 20	± 30
111584	25	75	5.6	9.0	5.6	1.6	3.2
082584	25	100	6.0	12.5	5.6	1.2	8.2
092584	25	100	6.7	9.0	5.6	0.6	9.2
102584	12.0	100	6.4	110.2	83.0	0.33	8.6
063584	25	100	7.2	5.6	2.3	1.4	9.7
073584	25	100	8.2	22.7	15.9	0.43	11.2
163584	12.5	100	4.1	55.6	48.7	0.27	5.6
173584	12.5	100	4.5	62.5	108.9	0.28	6.1
193584	12.5	100	4.2	31.8	11.5	1.76	5.7
203584	12.5	100	4.8	35.2	19.9	0.77	6.6

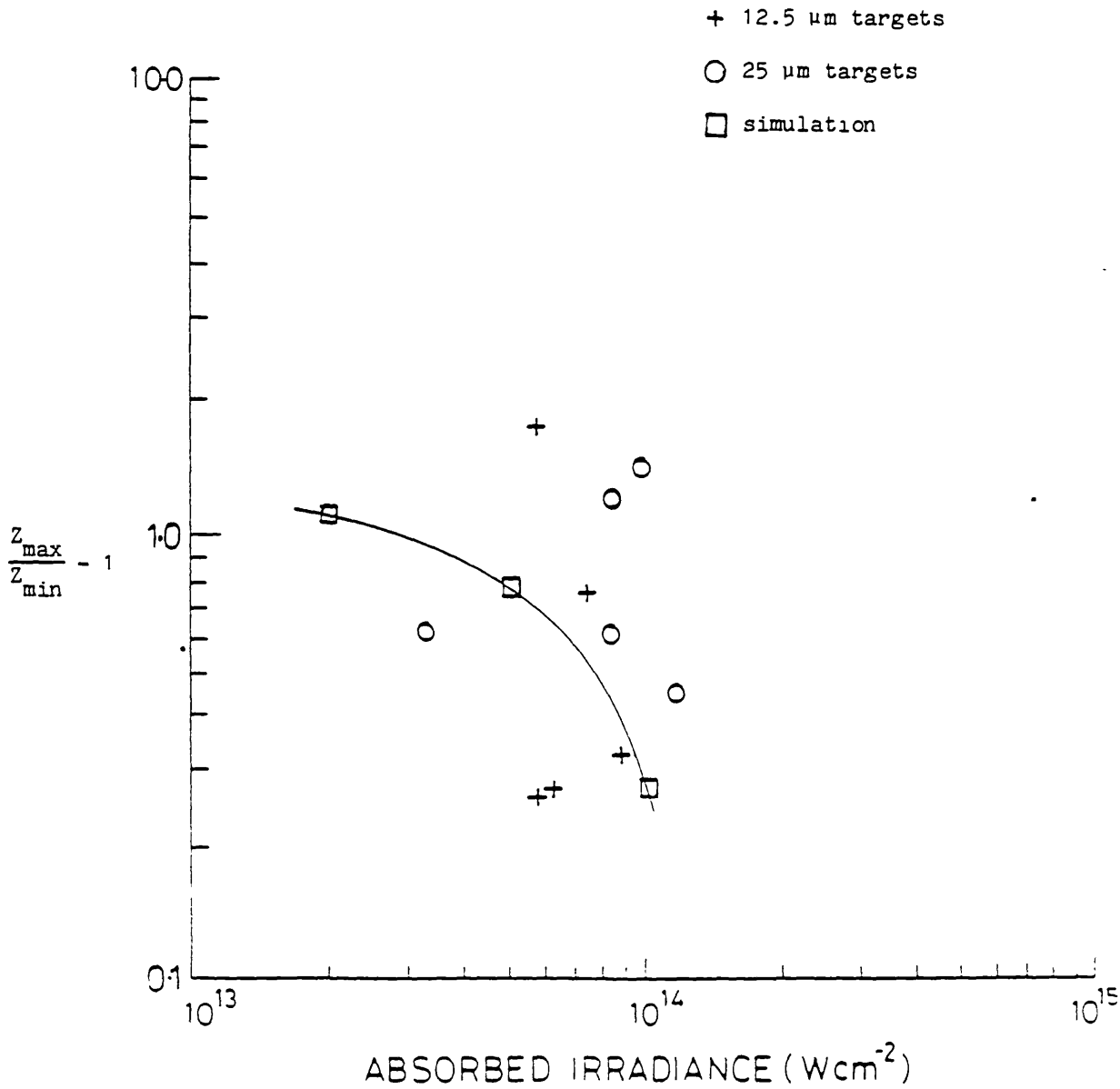

Fig.6.5 The variation of $Z_{max}/Z_{min} - 1$ as a function of absorbed irradiance for a beam modulation of $\lambda_p \simeq 50$ μm and $I_{max}/I_{min} \simeq 3:1$.

$$P \propto I^{0.7}$$

also if $P \propto Z$ (distance moved by the target) see equation 5.1. Then for a 3:1 irradiance non-uniformity if no smoothing were present

$$\Delta \simeq 1.1$$

which is consistent with the maximum values of Δ observed experimentally.

A large degree of scatter is evident from the data. This is probably caused by the significant uncertainty in exact focussing conditions in the experiment. Axial position of the target with respect to the lens focal plane was not known to better than ~ 50 μm. This positioning error varied from shot to shot and in some cases causes the calculated irradiances possibly being out by as much as a factor of two. A second consequence is a variation in the exact wavelength of modulation λ_p imposed on the target.

From Fig.6.5 it is not possible to calculate an accurate scaling relationship, but it is interesting to compare the results with the predicted degree of smoothing from 2-d simulations. These results are shown in Fig.6.5 and are an analytical scaling of the simulations performed at 1.05 and 0.53 μm(6.14) corrected for the different λ_p and I_{max}/I_{min} used in this experiment from those used previously(6.15). As can be

seen the irradiance regime investigated in this experiment is exactly where significant smoothing effects would be expected to occur. The fact that experimentally some shots do show a significant reduction in Δ from that expected for an unsmoothed drive pressure indicates that the experiment was successful in demonstrating thermal smoothing for 0.35 μm laser light at an absorbed irradiance above approximately 5×10^{13} Wcm^{-2} for a beam modulation wavelength of approximately 50 μm. This result supports a laser wavelength scaling for thermal smoothing of $\lambda_L^{2.0} - \lambda_L^{2.5}$ in reasonable agreement with previous results for $\lambda_L = 1.05$ μm and 0.53 μm.

6.5 Comparison of smoothing results

A comparison of the results of smoothing-irradiance experiments from Cole et al and the author is now made in order that a coherent picture of smoothing effects might be assembled. To make a valid comparison it is important that the results be presented with a careful choice of the 'degree of smoothing parameter' to be plotted as a function of absorbed laser irradiance. This smoothing parameter could either be (a) the smoothing expressed in its natural form i.e. $Z_{max}/Z_{min} - 1$ for the shadowgrams and $T_{max}/T_{min} - 1$ for the shock transit and colliding foils, although it is necessary to normalise the results to a low zero smoothing limit; or (b) use a $P_{max}/P_{min} - 1$ inferred from the smoothing parameters.

The former case has been used in the comparison since there is considerable uncertainty introduced by transforming the shadowgraphy and modulated shock transit ratios data to the

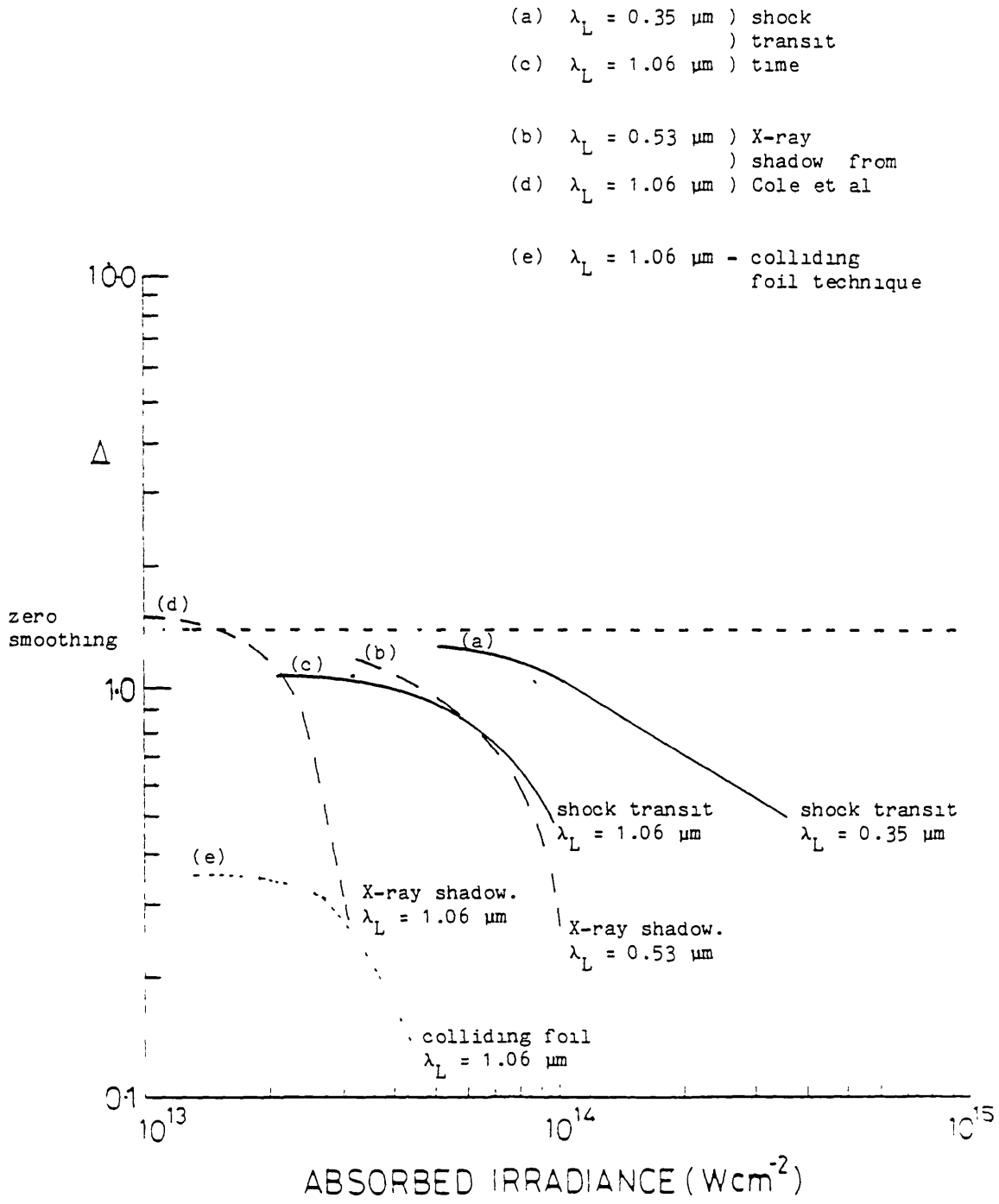

Fig.6.6 A comparison of the results of 'smoothing' measurements as a function of laser irradiance at different laser wavelengths using three different experimental techniques.

pressure non-uniformity $\Delta P/P$.

For the data presented the wavelength of modulation used λ_p has been the same ($\sim$90 μm) and the measurements have been made when a steady state separation of critical density to ablation front has been achieved (section 5.12). The intensity modulation however does complicate the comparison since the results from Cole et al were for I_{max}/I_{min} = 2:1 compared with 4:1 for the author's results. A correction has been made to Cole's results by adding a factor of 1.0 to each value of $(Z_{max}/Z_{min} - 1)$, this factor being the difference between the zero smoothing limit of 4:1 and a 2:1 intensity modulation i.e. $(4)^{0.7} - (2)^{0.7} = 0.6$. In this way a common zero smoothing limit of $\approx$1.6 is indicated on the Δ axis in Fig.6.6. The key describes the origin of the data and is as follows :

(a) shock transit time results at λ_L = 0.35 μm
(c) shock transit time results at λ_L = 1.06 μm } Chapter 5

(b) X-ray shadowgraphy data at λ_L = 0.53 μm
(d) X-ray shadowgraphy data at λ_L = 1.06 μm } Cole et al[6.3]

(e) colliding foil results at λ_L = 1.06 μm (Chapter 5)

A number of features are apparent in the smoothing graph :

(a) The X-ray shadowgraphy and modulated shock transit results appear to have a region of a common low irradiance-zero smoothing limit for all laser wavelengths. Assuming the correction factor to transform the different initial intensity modulations is

valid.

(b) The threshold of irradiance before some degree of smoothing begins seems to be $I_{abs} \approx 2 \times 10^{13}$ Wcm^2 at λ_L = 1.06 μm for the shadowgrams and $I_{abs} \approx 4 \times 10^{13}$ Wcm^3 at λ_L = 1.06 μm for the shock transit. The rate of increase of smoothing (reduction in Δ) is much greater for the shadowgraphy compared to the shock transit time.

(c) The irradiance for the 0.53 μm shadowgraphy data is ≈ 6 x 10^{13} Wcm^{-2} whereas the threshold for the 0.35 μm shock transit data is ≈ 1 x 10^{14} Wcm^{-2}. The rate of increase in smoothing for the 0.35 μm data is much less than the 0.53 μm shadowgraphy data.

(d) The colliding foil results at 1.06 μm show greatly enhanced degrees of smoothing which is consistent with considerable hydrodynamic effect contributions.

The fact that further accurate comparisons cannot be made from these results is evidence that far too little data is available to predict accurately the degree of 'thermal' smoothing present under different laser conditions.

There are a number of caveats which are associated with each of the measurements made to date. The modulation shock transit time suffers from the interpretation problem associated with the scaling of the shock transit time being different for different phases of the irradiation. Additionally there is the possibility that as the modulated shockfront transits the target the shock non-uniformity profile tends to smear itself out. This 'shock smoothing' process has been examined by some workers(6.16,6.17) and considered not to produce a significant

contribution.

A tentative scaling of smoothing with wavelength from the 1.06 μm and 0.35 μm data is $1/\Delta \propto \lambda_L^{0.9-1.4}$ although much more data is required to have confidence in such a scaling.

6.6 Conclusions and future work

The conclusions from the shadowgraphy results in this chapter are somewhat tentative. No scaling of smoothing versus irradiance has been obtained due to the large uncertainty in laser irradiance and wavelength of modulation λ_p. However the data obtained has demonstrated some evidence of thermal smoothing at a laser wavelength of 0.35 μm using a modulation wavelength of ≈ 50 μm. The results are not inconsistent with a smoothing scaling of $\lambda_L^{2.0} - \lambda_L^{2.5}$.

The increased laser irradiances available with the new VULCAN system will ensure that the gross uncertainties observed in this experiment will not plague future studies. Interpretational problems have become apparent in the use of the 50 μm period modulation with beams of spatial fill factor of 0.5. This suggests that it may be safer to return to the higher periods of modulation and use the higher laser irradiances now available which are capable of probing the regions where simulations predict significant smoothing may occur.

An attempt was made in this experiment but due to operation difficulties was not successful, to perform a simultaneous measurement of smoothing using both X-ray shadowgraphy and modulated shock transit time. Such an experiment may resolve a number of questions about the

relationship between the two techniques of measurements.

Clearly more data particularly for the shock transit time λ_L = 1.06 μm and 0.53 μm is important. Also is good quality shadowgraphy data at 0.35 μm. An intriguing scaling of $\lambda_L^{0.9-1.4}$ is tentatively inferred from the shock transit data.

Some workers(6.14,6.18) have suggested a differential mass ablation rate technique using a layered target as an alternative to infer the pressure non-uniformity of the ablation front. Such an approach would have a lot to commend itself since it directly accesses the ablation front and as such avoids diagnosing the pressure non-uniformity by measurement of an intermediate second parameter.

The results described in Chapter Three of this thesis employing multi-layer transparent targets suggest a technique which could provide a time resolving analysis of the development of the pressure non-uniformity during irradiation. Optical streak photography would produce a series of non-uniform shock transit profiles which would diagnose the modulation in shock transits and therefore the pressure non-uniformity. A similar type of observation has already been made with a colliding foil target where the second target was transparent(6.19). However careful choice of materials to match the material layer impedances would be important to avoid the complications of non-uniformity growth with the Richtmyer-Meshkov instability(6.20,6.21).

CHAPTER SEVEN

COMPRESSION OF MATERIAL TO HIGH DENSITY USING COLLIDING SHOCKWAVES

7.1 Abstract

X-ray streaked radiographic measurements have been made on planar targets strongly heated and highly compressed by the collision of two opposed shocks driven by 0.53 μm radiation. Additionally, single sided irradiation has allowed the simultaneous measurement of shockwave and particle velocity defining a point on the mylar Equation of State. The pressures inferred from these measurements are in good agreement with the pressure-irradiance scaling obtained from experimental data in Chapter Two. Both dual and single sided irradiation results agree well with computer simulations using the 1-d Hydrocode MEDUSA. Compressions of the order of six and three respectively infer a density enhancement of a factor of two by using colliding shocks.

7.2 Introduction

Ultra high power lasers have the ability to compress and heat materials to densities and temperatures otherwise unattainable in the laboratory. Apart from its intrinsic

interest the study of materials under such conditions allows an equation of state to be defined and is important in inertial confinement fusion studies. The experiments described in this chapter use time resolved X-ray radiography to diagnose the state of compression, density and pressure of material produced by the collision of two opposed 'shocks' driven by dual sided 0.53 μm radiation. Also, using single sided irradiation a simultaneous measurement of shockwave and particle velocity has been made allowing an equation of state point to be defined for the target material. Only in experiments using nuclear explosions has this been possible previously(7.1,7.2).

In this work a novel technique employs thin Bismuth tracer strips to diagnose the dynamics of material compression, the planar geometry used being particularly amenable to radiographic probing. Previous specific measurements(7.3) of particle velocity have only been made in a regime a factor 10 lower than velocities recorded here and with only moderate time resolution (hundreds of picoseconds).

7.3 Experimental

Two frequency doubled beams of the VULCAN laser were used to irradiate both sides of planar 'slab' targets with 1.5 nsec FWHM pulses of 0.53 μm radiation. The experimental arrangement is shown in Fig.7.1.

The targets consisted of a layer of mylar coated with equal thicknesses of n-type parylene either side. The targets were self backlighting by means of an additional horizontal bismuth bar (A) vacuum deposited on the front of one side of the

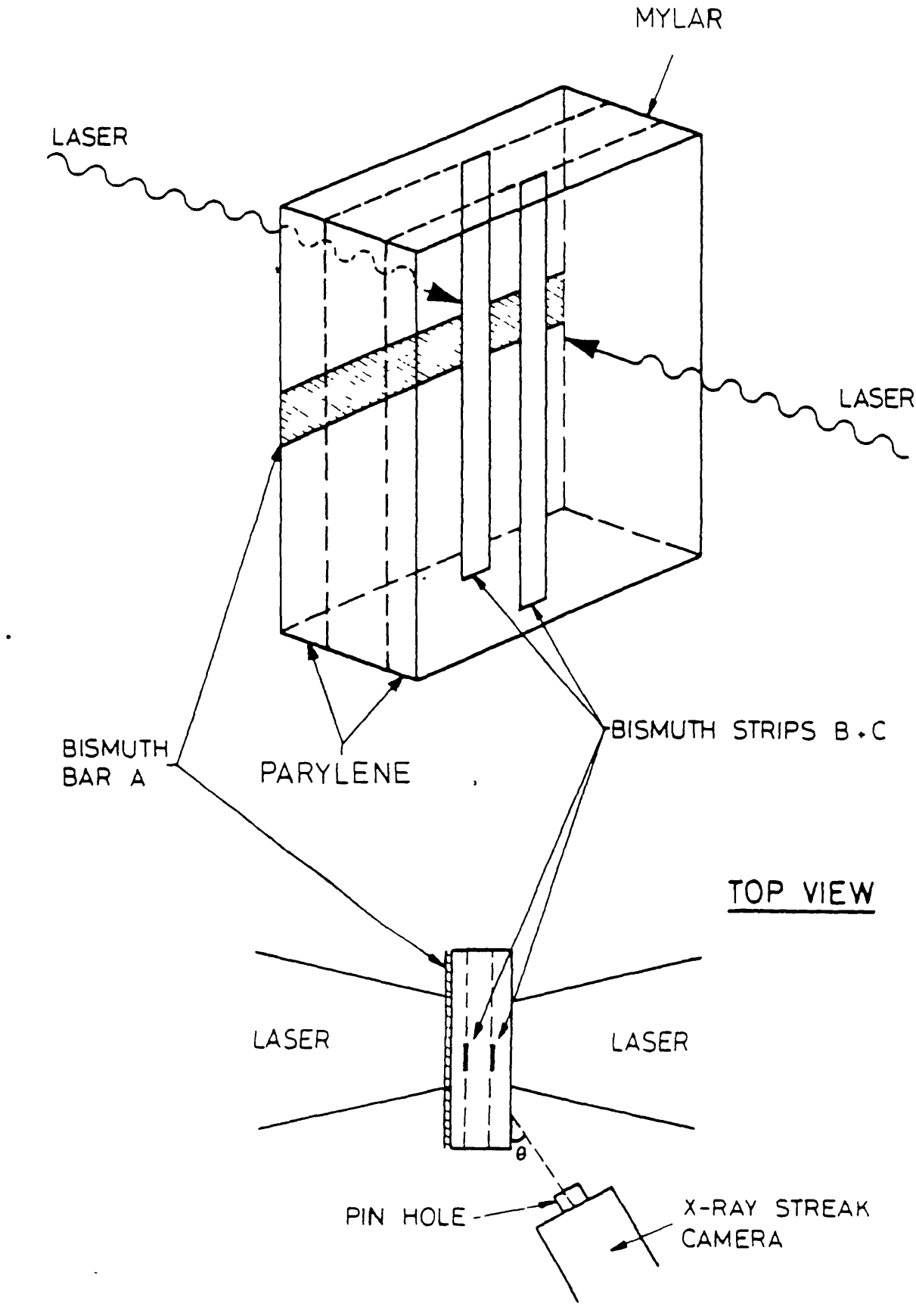

Fig.7.1 Experimental arrangement to perform X-ray streaked radiographic measurements using dual and single sided laser irradiation.

target. The compression of the material was followed by the X-ray shadow of two vertical bismuth tracer strips ($\sim$ 0.1 μm) (B and C) vacuum deposited between the mylar and parylene layers. The laser focal spot was placed on the 'cross' formed by the bismuth horizontal and vertical strips. The X-ray shadow of the tracer strips was time resolved with a KENTECH X-ray streak camera(7.4) imaged through a 4 μm platinum pinhole. The angle of view θ, was a trade off between target absorption (lower for high θ) and spatial resolution (better for small θ). The angle chosen gave a backlighting cut off energy of 2.5 KeV and a spatial resolution of 8 μm (with the pinhole used).

An alternative separate backlighting target scheme (as used in Chapter Six) was investigated to avoid the complications of target preheating inherent in the self backlighting approach. However a sufficiently bright and uniform X-ray backlighting source proved unattainable and was complicated by the sensitive separate alignment procedure.

In the initial stage of the experiment single sided irradiation was used to measure the shockwave and particle velocities from the trajectories of the bismuth tracer strips. The position of the shockfront was well diagnosed by the reaction of the tracer strips during the shock transit.

It was found that the quality of target preparation was an overriding factor to obtain the good clarity necessary for an unambiguous measurement. Rigorous microscopic analysis was used to check target quality before insertion into the target chamber. Precise alignment of the bismuth bars, laser focal spot and X-ray streak camera pinhole proved an onerous task and

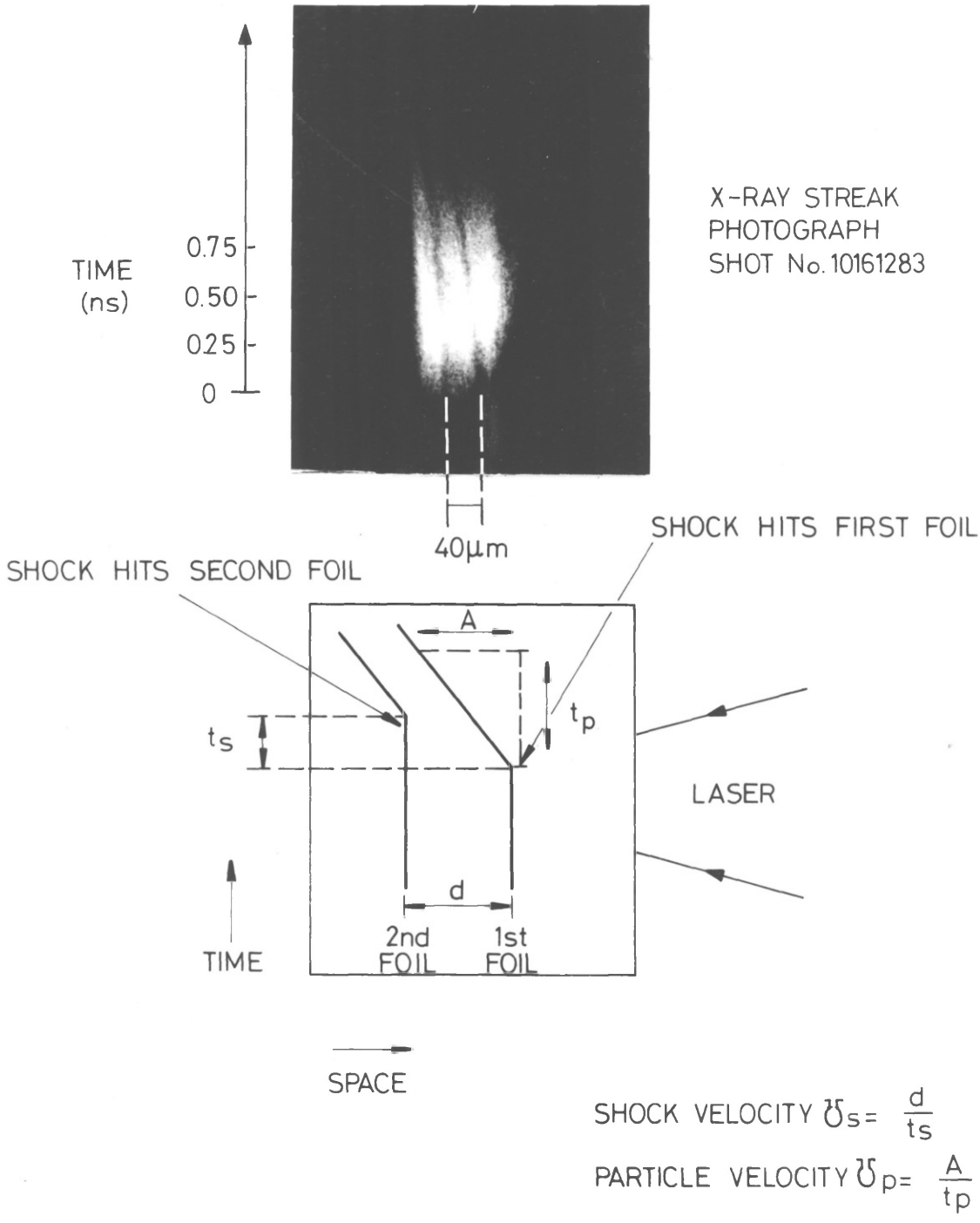

Fig.7.2 X-ray streak photograph and schematic diagram showing the use of two embedded bismuth tracer strips to measure shockwave and particle velocity.

resulted in only a very small number of unambiguous experimental results.

7.4 Results

7.4.1 Single sided irradiation

An X-ray streak radiograph is shown in Fig.7.2 together with a schematic diagram representing the reaction of the bismuth tracer strips. The average shockwave velocity over the mylar layer is measured from the time delay between the reaction of each of the strips as the shockfront transits the target. The particle or matter velocity imparted to material behind the shock is calculated from the slope of the trajectory of the first bismuth strip. Unfortunately only one shot proved to have conditions of target quality, bismuth strip alignment, source brightness and uniformity sufficient to produce an unambiguous streak radiograph with good clarity. The details of target dimensions and laser irradiance parameters are shown in Table 7.1.

A complication of the interpretation of the strip trajectory arises in the curvature or 'pincushion' distortion(7.5) imposed by non linearities in the image intensifier used in the X-ray streak camera. Correction for this effect can be made by deconvolving the image with a function derived from the distortion imposed on a static fine scale grid. Such an approach has been used by some workers(7.6). However, 2-d digitization of each image is necessary to perform this operation. No facility was available to deconvolve the images obtained and estimates based on worst

TABLE 7.1

DETAILS OF X-RAY RADIOGRAPHIC SHOTS FOR SINGLE AND DUAL SIDED 0.53 μm LASER RADIATION

Shot type	Dual sided	Dual sided	Single sided
Shot number	11 14/12/83	21 14/12/83	10 16/12/83
North beam energy (J) ± 10%	29.6	30.0	32.0
South beam energy (J) ± 10%	27.6	29.0	-
Spot diameter (μm) ± 20 μm	110	140	110
Pulse length (nsec)	1.5	1.5	1.5
Average intensity (W/cm^2) ± 30%	2.01×10^{14}	1.3×10^{14}	2.2×10^{14}
Target details	0.35 μm bismuth bar/ 7 μm N-parylene/ 48 μm mylar/ 7 μm N-parylene. (0.1 μm vertical strip on each side of mylar region)	0.35 μm bismuth bar/ 7 μm N-parylene/ 45 μm mylar/ 7 μm N-parylene. (0.1 μm vertical strip on each side of mylar region)	0.35 μm bismuth bar 8 μm N-parylene/ 45 μm mylar/ 8 μm N-parylene. (0.1 μm vertical strip on each side of mylar region)
Peak Compression	6.0	5.0	2.3

case values for the same intensifier[7.7] have been used to correct the trajectories. In the example used the peak distortion is only a nominal few percent due to the careful positioning of the image in the centre of the intensifier face where least distortion is encountered.

The particle and shockwave velocities measured from shot no.10161283 are respectively :

$$V_p = (2.5 \pm 0.4) \times 10^6 \text{ cm s}^{-1}$$

$$V_s = (4.4 \pm 0.8) \times 10^6 \text{ cm s}^{-1}$$

From equation 1.10 the pressure P, shock velocity V_s, particle velocity V_p and initial material density ρ_i can be described by

$$P = \rho_i V_s V_p$$

Using the measured values and $\rho_i = 1.39$ g cm^{-1} gives

$$P = (15 \pm 5) \text{ MBAR}$$

The internal energy Δ_i can be expressed in terms of V_p by equation 1.12 :

$$\Delta_i = \frac{1}{2} V_p^2$$

which gives $\Delta_i = 3.1 \times 10^5$ J.g^{-1}

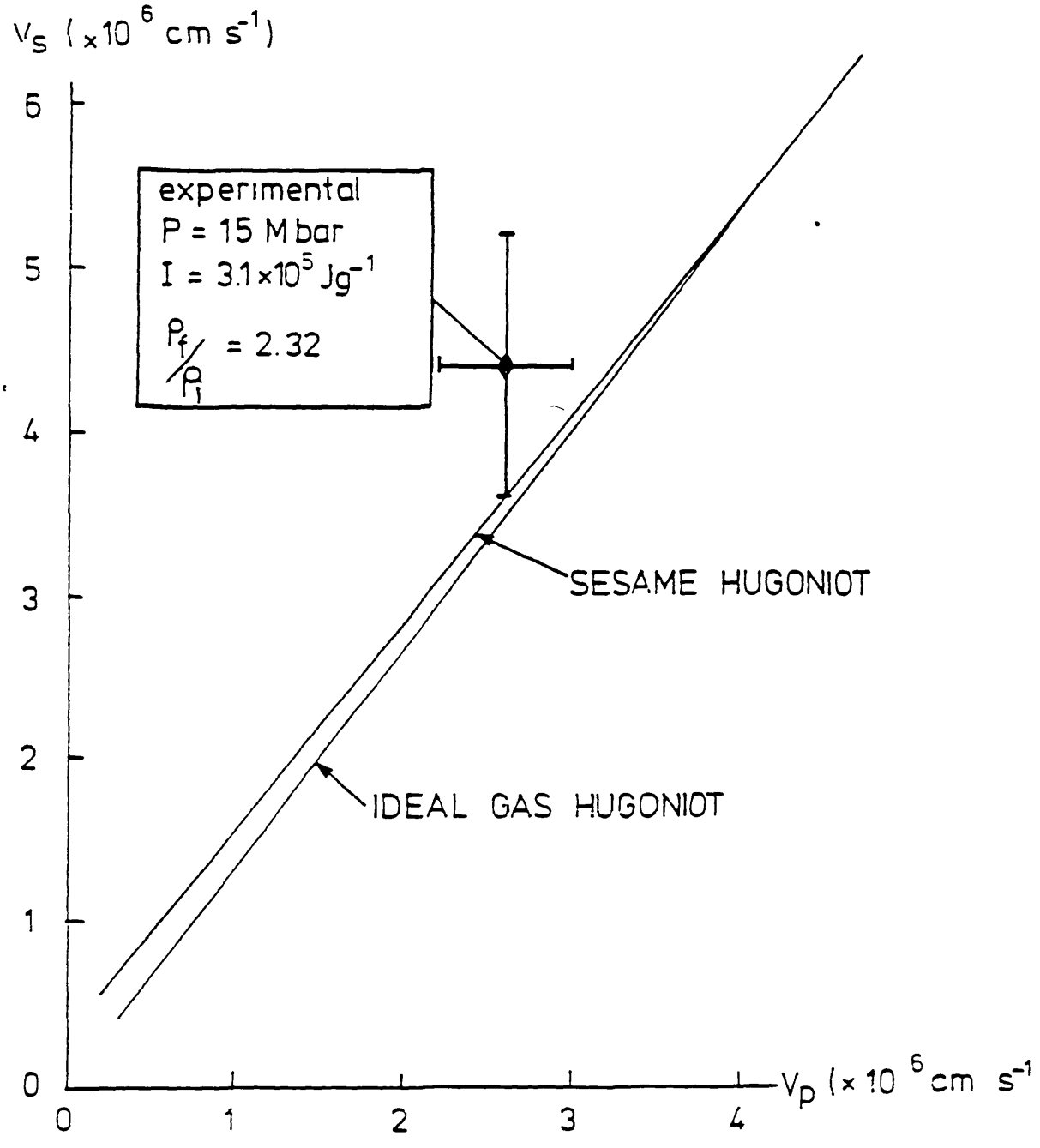

Fig.7.3 A comparison of SESAME Hugoniot for mylar and an ideal gas Hugoniot from ref.(7.6) with the experimental measurement.

The compression in the material can be expressed from equation 1.9 as :

$$\frac{\rho_f}{\rho_i} = \frac{V_s}{V_s - V_p}$$

where ρ_f is the density of the 'shocked' material. Using the measured values gives

$$\frac{\rho_f}{\rho_i} = 2.3$$

It is interesting to compare the measured values with code simulations using the 1-d Hydrocode MEDUSA(7.8), EOS data for mylar(7.9) and the experimentally determined scaling law for pressure and laser irradiance at 0.53 μm from Chapter Two.

Taking the last case first, the scaling law from Chapter Two gives

$$P[\text{MBAR}] = 3.1 \pm 0.7\ I_{abs}^{0.63\pm0.15}[/10^{13}\ \text{Wcm}^{-2}]$$

For the irradiance used and an absorption fraction of ~ 0.8 gives :

$$P = 17 \pm 10\ \text{MBAR}$$

This is in very good agreement and corroborates two independent measurements of pressure using different techniques enhancing

Fig.7.4 A 1-d code simulation using MEDUSA showing the predicted bismuth tracer strip trajectories during single sided irradiation, laser incident from the right.

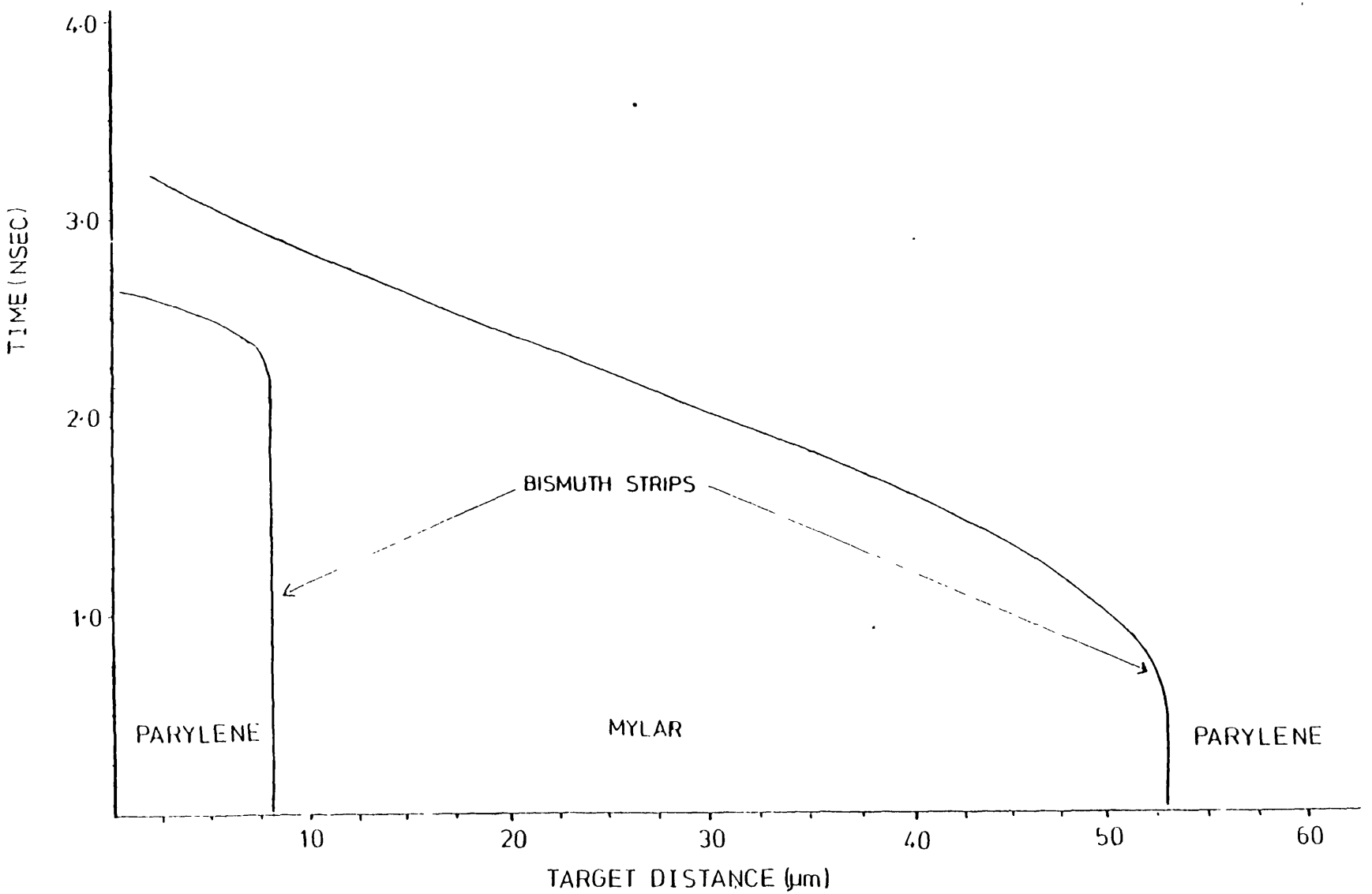

confidence in the validity of both results.

To compare the theoretical EOS data for mylar with the experimental EOS point Fig.7.3 has been plotted showing the SESAME EOS for mylar Hugoniot and the experimental point. The ideal gas Hugoniot has also been shown for comparison. As can be seen good agreement is found within the limits of experimental error.

7.4.2 Comparison with 1-d code simulations

The experimental trajectories of the strips have been compared with simulations using the 1-d Hydrocode MEDUSA. It should be noted that no account has been taken of the bismuth bar or strips in either the hydrodynamics or radiative heating of the mylar layer. Additionally no account of incident irradiance non-uniformities have been taken in this one dimensional code.

Fig.7.4 shows the code predicted trajectories of the strips. The values for particle and shockwave velocity predicted by the code compare with the experimental velocities as follows :

$V_{p\ code} = 2.4 \times 10^6$ cm s^{-1} $\quad V_{p\ exp} = 2.5 \pm 0.4 \times 10^6$ cm s^{-1}

$V_{s\ code} = 3.4 \times 10^6$ $\quad V_{s\ exp} = 4.4 \pm 0.8 \times 10^6$ cm s^{-1}

The discrepancies between the shock velocity values could be explained by the radiative heating of the mylar from the high z bismuth bar increasing the shock velocity in the experiment

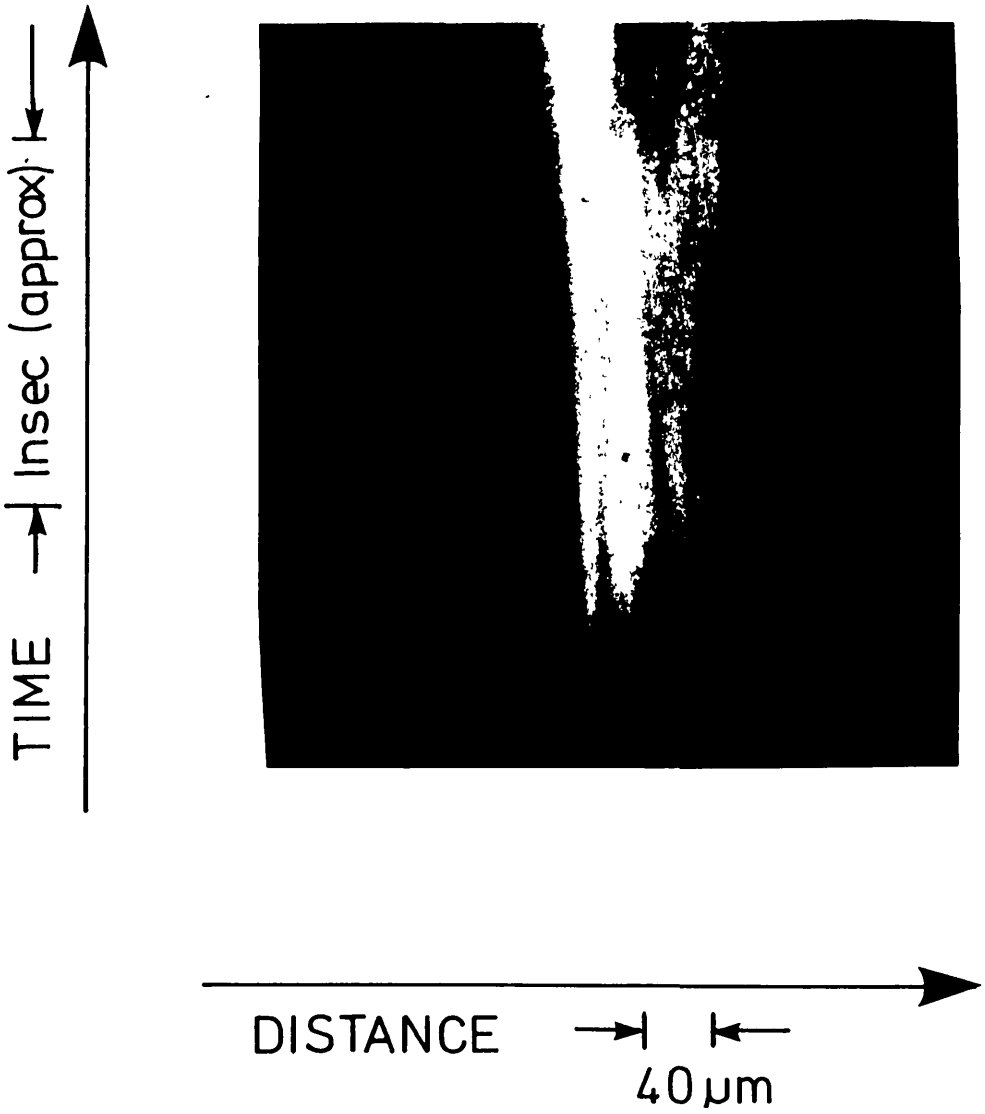

Fig.7.5 An X-ray streak radiograph for dual sided irradiation.

compared to the code prediction. Also there is a slight numerical uncertainty of the position of the shockfront arising from the cell size used in these code runs. This uncertainty could easily be resolved by running the code with a larger number of cells defining the mylar/surface interface more precisely.

The compression predicted by the code compares with the experimentally inferred value by

$$C_{code} = \frac{\rho_f}{\rho_i} = \frac{43}{1.39} = 3.0$$

$$C_{exp} = 2.3$$

These values are in reasonably good agreement with each other and could be in significantly better agreement if target preheating from the bismuth layer was included in the simulations.

7.4.3 Dual sided irradiation

An example of a streaked radiograph from shot no.11141283 (details given in Table 7.1) is shown in Fig.7.5. The peak compression in this shot, measured from the ratio of the initial and final tracer strip separations was ≥ 6, the lower limit being set by the resolution. Again the 1-d code MEDUSA has been used to simulate the experiment. The degree of material compression during irradiation predicted by the code is

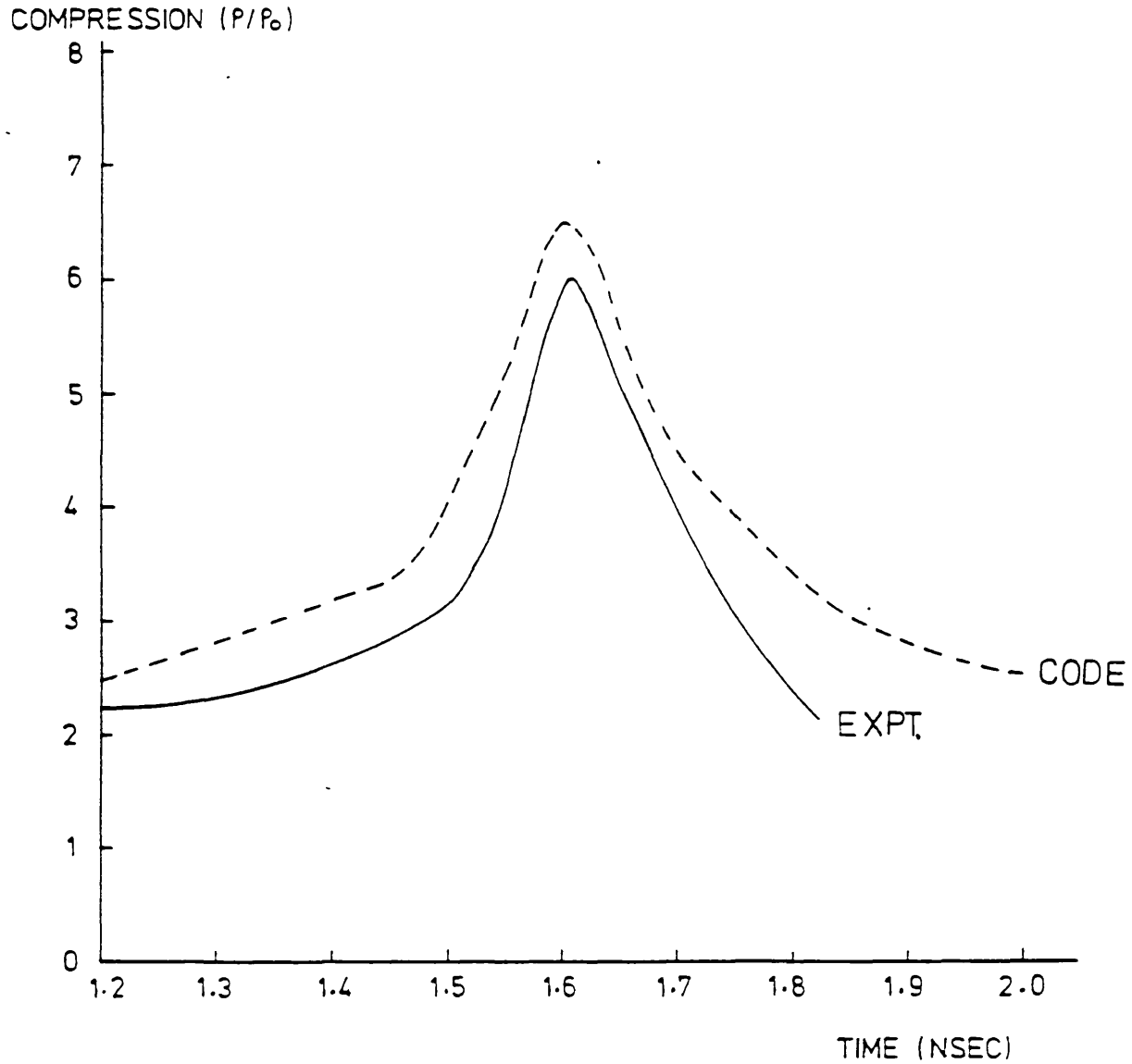

Fig.7.6 A comparison of 1-d hydro simulation from MEDUSA and experimental measurement of compression during dual sided irradiation, shot no.11141283.

shown in Fig.7.6 together with the experimentally inferred values. The time of experimental peak compression has been normalised to the code peak compression time.

The peak values are within 10% of each other. After peak compression the experimental measurements have an increased uncertainty since the X-ray bismuth backlighter begins to reduce significantly in brightness level.

The time during which the X-ray backlighter remains on is controlled by the 'burnthrough' time of the bismuth layer. There are opposing constraints on increasing the bismuth thickness to extend the backlighter duration and reducing the thickness to lower the radiative preheating on the remainder of the target. A scheme in future experiments could utilise a plastic overcoat which could prevent the 'turn on' of the backlighter until close to the time of peak compression although this of course would impose an additional complication in the hydrodynamics. The peak compression compared to the single sided irradiation case infers a density enhancement of the order two by using colliding shocks.

7.5 Conclusions and future work

The results presented in this chapter have demonstrated the use of colliding shocks to compress material to high density. Compressions of six compared with three obtained from single sided irradiation infer a density enhancement of a factor of two by using colliding shocks. For the first time a simultaneous shockwave and particle velocity measurement has been made in a laboratory study at ultra high pressure (> 10

MBAR), defining an EOS point for the target material (mylar). The inferred pressure values from single sided irradiation have corroborated the pressure irradiance scaling from Chapter Two. Good agreement has been reached between both dual and single sided irradiation experiments and predictions by the 1-d hydrocode MEDUSA, particularly if some level of target preheating (not treated in the code) is taken into account.

The complications of target hydrodynamics (particularly in the dual sided case where asymmetry is introduced) and preheating arising from the self backlighting scheme could largely be resolved by using a separate backlighting target. The separate backlighting approach investigated for these experiments suffered due to the limited laser energy available and the 1.06 μm laser wavelength. Future experiments would have 50% more energy available in the new upgraded VULCAN laser system and the option for 0.53 μm backlighting irradiation where conversion efficiency for X-ray radiation is much higher(7.10). The alignment difficulties encountered with the separate backlighting scheme could be resolved with a CW laser alignment axis technique.

The different material layers are not concomitant with a 'clean' shock experiment. The propagation of the shocks over the material layer boundaries could lead to growth of laser beam induced non-uniformities in the shockfront via the Richtmeyer Meshkov instability(7.11) (as discussed in Chapter Three), degrading the final compression. A more satisfactory target design would have the tracer strips embedded in a block of a single material. Even then the shockfront would have to

negotiate the slight impedance mismatch. Future experiments will replace the mylar with a material whose EOS is better studied. Aluminium may be a suitable candidate. The problems will lie in the necessary increase in X-ray probing energy (around 5 KeV) due to the position of the aluminium 'k' absorption edge. To accurately diagnose high compressions the initial tracer strip separation would have to be increased since to maintain brightness levels no reduction in pinhole size could be tolerated.

A longer pulselength with the recently increased VULCAN energy would be able to drive steady shocks for a longer time allowing the target size to be increased.

It is important to provide a comprehensive analysis by 2-d digitization of the streak images. Facilities are now available and will be used to analyse future results.

CHAPTER EIGHT

CONCLUSIONS

8.1 Abstract

The conclusions and contribution of this thesis are stated. Future directions for further experimental work are discussed.

8.2 Conclusions

In Chapter Two the first systematic measurement of laser induced shock pressure as a function of laser irradiance at 0.53 m has been obtained. Furthermore the measurements have been made using a stepped target emission technique, capable of giving a precise measurement of shockwave velocity. The accuracy of the corresponding shock pressure is dependent on the accuracy of the E.O.S. data used in its determination, which for the case of Aluminium (the target material) is currently one of the most well-defined. The results are in good agreement with 1-d hydrocode simulations(8.1) using multi-frequency radiation transport and pressures derived from mass ablation rate measurements(8.2) for the case of negligible lateral energy loss. This corroborates the importance of lateral energy loss in planar target experiments.

Some data at 0.35 μm has been obtained and pressure

enhancement at short wavelengths has been demonstrated. This effect has been predicted by many authors due to two factors; the increase in dominance of Inverse Bremsstrahlung absorption at short wavelength leading to higher absorption fractions(8.3) and the higher hydrodynamic efficiency expected as a result of the energy becoming deposited at higher densities(8.4).

An important future experiment would be a simultaneous measurement of mass ablation rates and shock velocities from stepped targets which would resolve questions about pressures inferred from each type of measurement.

Chapter Three describes a novel sequence of temporal shock emission which may prove to be a useful diagnostic in a number of future experiments. The data is however only qualitative in nature due to the non-ideal experimental conditions and the over complexity of the target design - a feature which was not controllable in this study. The changes in shock luminosity have been shown to agree with the times at which the shockfront would be expected to cross the interface between the layers of different acoustic impedance. Gross impedance mismatch has been shown to cause sharp rises in compression and temperature by some workers(8.5). This is in reasonable agreement with the experiments described in this chapter, although target preparation of material interfaces may account for some anomalies.

Sufficient evidence has been obtained to warrant a further study using a simple two layer target configuration where interpretation of the results will be easier. Collaboration with the workers at Soreq research Centre is

planned in this respect(8.6).

In Chapter Four a dual channel low level (few eV) preheat diagnostic was designed and constructed to measure low levels of target preheating up to 2 eV. Results from a commissioning experiment demonstrate that it is capable of diagnosing preheat levels of 0.1-0.5 eV and shock temperatures of 0-2 eV, consistent with the target and laser irradiation conditions. Additionally a simultaneous streaked spectrograph inferred a shock velocity which through E.O.S. data for Aluminium predicted a shock temperature in good agreement with the dual channel temperatures. The diagnostic is now well placed to infer low level temperatures with improved accuracy by optimising the spectral response function of the two channels.

An interesting future study could involve an additional channel in the near UV region of the spectrum to separate the channels and extend the useful temperature range to $\sim$ 10 eV.

Chapters Five and Six describe measurements of the smoothing of imposed laser beam homogeneities. Three basic studies were performed, the first compared smoothing rates using a colliding foil measurement and a previously unused modulated shockwave transit technique to infer degrees of smoothing. The results suggested that hydrodynamic effects were contributing significantly to the colliding foil measurements of smoothing which were considerably greater than those inferred from the modulated shockwave transit technique. Even with ideal target preparation or design it seems unlikely that such an approach could eliminate target acceleration effects completely.

The second study then used the modulated shock transit

approach to obtain a scaling of smoothing with irradiance which was significantly lower than previous work. The measured scaling agrees with previous computer simulations[8.7] and with an analytical model of thermal smoothing which suggests that a smoothing factor f relates the pressure non-uniformity ($\Delta P/p$) due to an irradiation non-uniformity ($\Delta I/I$) by

$$\frac{\Delta P}{P} = f \frac{\Delta I}{I}$$

where $f = \exp(-4\pi D_\infty/L_p)$ and D_∞ is the steady state separation between the critical density and ablation front and L_p is the wavelength of the imposed perturbation. This exponent is in agreement with recent theoretical work[8.8] which is higher than a simple diffusion model exponent ($-2\pi D_\infty/L_p$).

A third experiment using X-ray shadowgraphy was successful in demonstrating evidence of some degree of smoothing with a reduced wavelength of modulation λ_p, although a scaling of smoothing with irradiance was not obtained.

Future experiments in this field are essential to obtain further understanding, data at 1.06 μm and 0.53 μm is necessary to qualify the 0.35 μm data already obtained. Possibly a differential mass ablation rate approach would provide useful results accessing the pressure non-uniformities on the ablatiion front directly.

In Chapter Seven a novel experiment has been performed. Single sided 0.53 μm laser irradiation has allowed a

simultaneous shockwave and particle velocity measurement to be made. Streaked X-ray shadowgraphy has given good accuracy in this measurement which has permitted a point on the E.O.S for mylar to be inferred. Excellent agreement has been reached between the pressure inferred in this experiment and that from the scaling law of pressure and irradiance in Chapter Two. Further corroborative evidence has been obtained with computer simulations with the 1-d hydrocode MEDUSA which predicted pressures in close agreement.

Dual sided irradiation has been used to collide two opposing shocks which gave compressions of the order of six. Again good agreement between the experiment and MEDUSA simulations was found which demonstrated a factor of two in density enhancement by using colliding shockwaves.

Further work here is necessary in the deconvolving of image intensifier distortion and the re-design of the irradiance geometry to optimise resolution in view of the greater laser energy now available with the VULCAN laser system.

APPENDIX A

THE TEMPORAL AND SPECTRAL CALIBRATION OF THE HADLANDS IMACON 675 OPTICAL STREAK CAMERA

Before meaningful accurate measurements can be made using a streak camera it is important to know the variation of streak rate of the camera at a particular streak speed setting for different positions of the streak image at the rear of the camera intensifier face. Obviously for studies involving the relative emission at different wavelengths the spectral sensitivity of the camera photocathode is an essential parameter.

The calibration of the streak cameras used in the experiments described in this thesis have been carried out using the streak camera calibration facility at AWRE Aldermaston[A.1]. The basic experimental set up is shown in Fig.A.1.

A Nd. glass and Nd. YAG oscillator were used and the output pulse frequency doubled using a KD*P crystal. Typically the Nd. glass gave pulse durations in the range 6-12 psec. The pulse was passed through a reflection Fabry Perot etalon employing a 50% reflective and a 100% reflective mirror. The separation between each of the train of pulses produced was

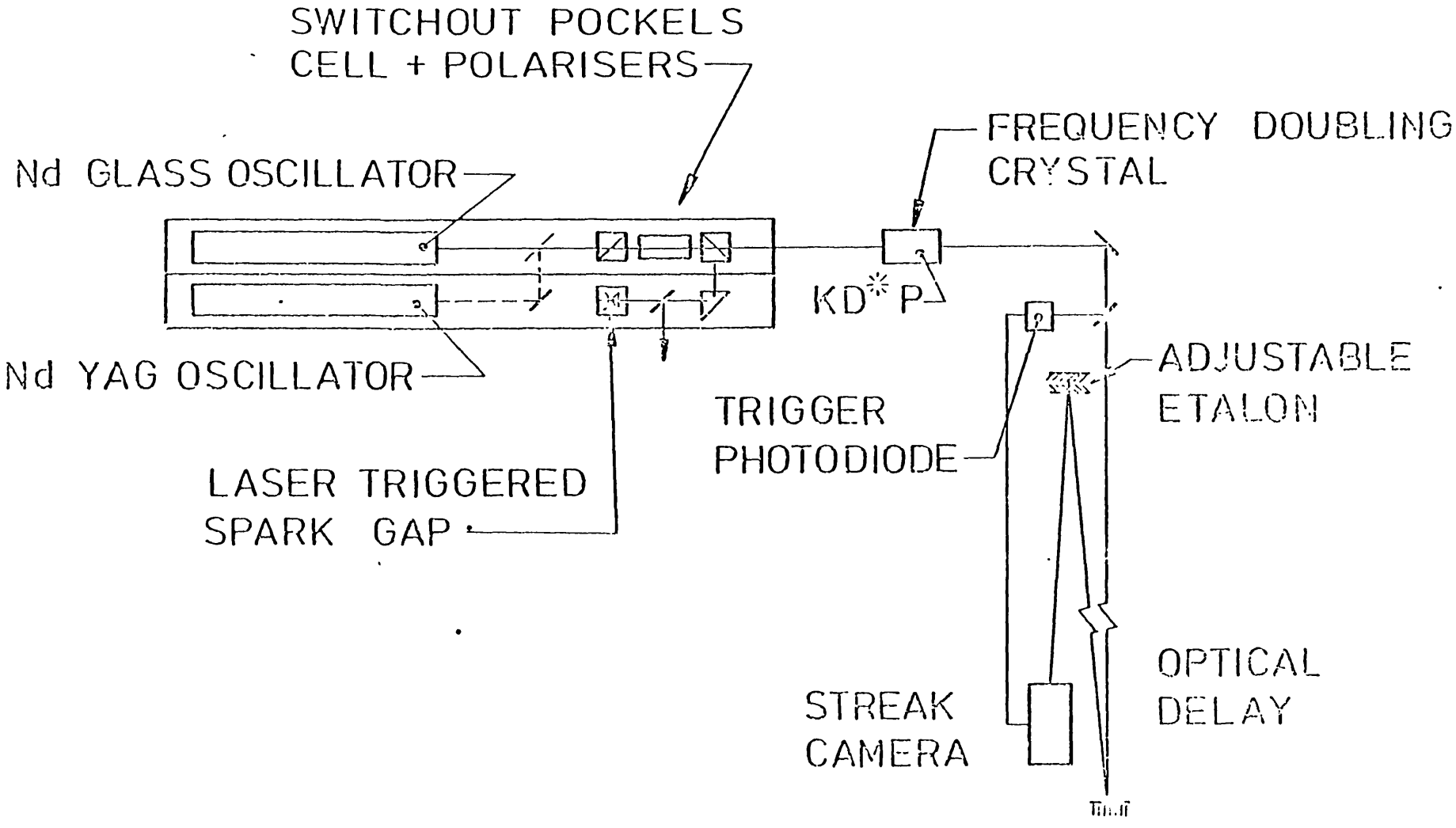

Fig.A.1 The streak camera temporal calibration facility from Ref.(A.1).

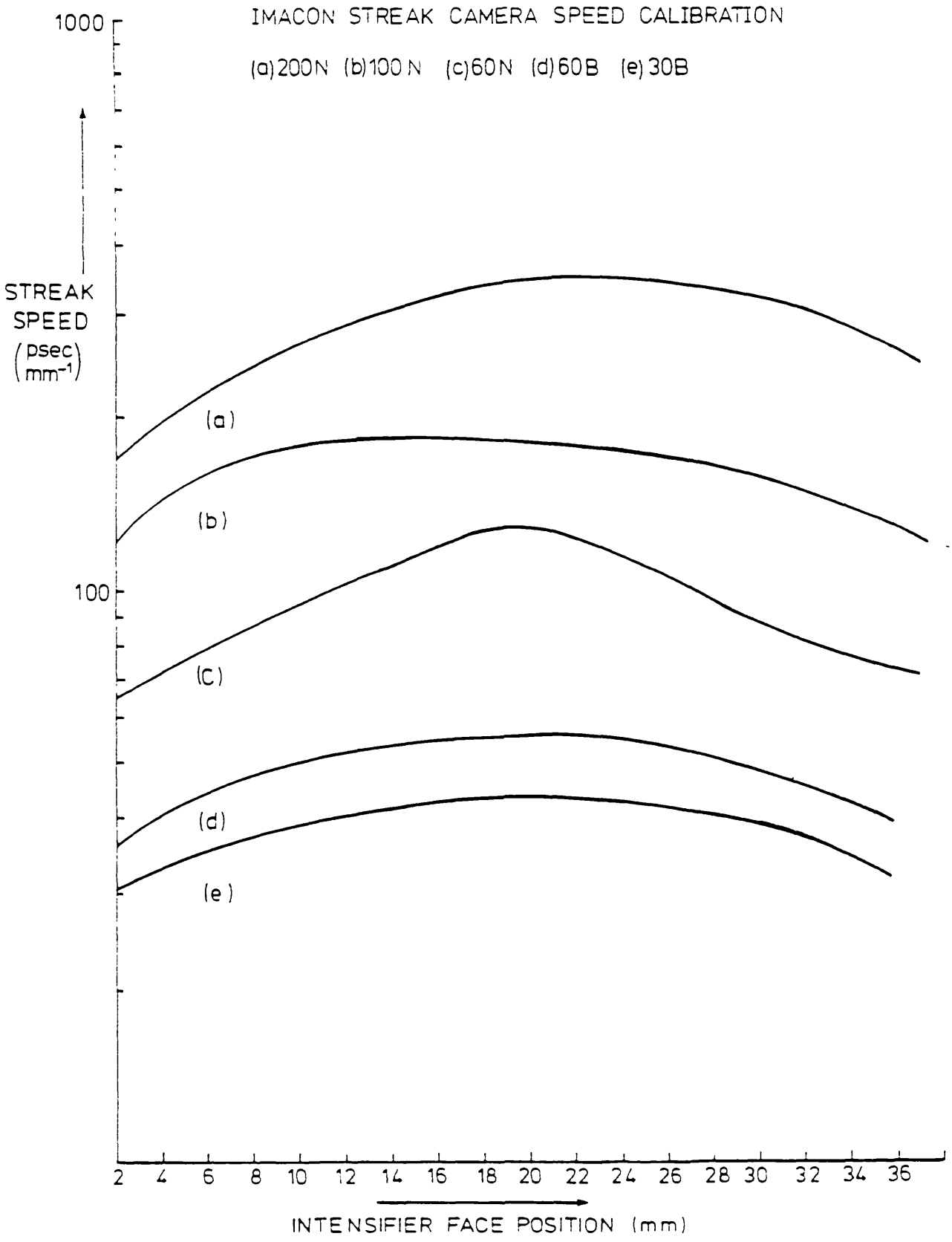

Fig.A.2 The calibration of streak camera speed as a function of the intensifier face position for streak rates of (a) 200 N, (b) 100 N, (c) 60 N, (d) 60 B, and (e) 30 B.

adjusted by variation of the etalon spacing.

The streak speed was calculated from the spatial separation of the pulse images and the known etalon spacing. By empirical adjustment of the camera trigger delay the whole of the camera face could be scanned.

The variation of the streak rate at different streak speed settings is shown graphically in Fig.A.2.

The spectral sensitivity measurements of the streak camera image tube were performed using the purpose built AWRE Aldermaston facility. The system images a known intensity of light at a specific wavelength onto a unit area of photocathode which is set a specific voltage relative to the camera extraction grid and focus cone. Electrons from the photocathode are accelerated towards and collected by the grid and focus cone and the current flow, which is related to the cathode sensitivity, is obtained from the voltage drop in a standard resistor. The photocathode sensitivity of the S20 tube is shown graphically in Fig.4.2.

REFERENCES

1.1 J. Nuckolls, L. Wood, A. Thiessen and G. Zimmerman, Nature, 239, 139 (1972)

1.2 J.J. Duderstadt and G.A. Moses, "Inertial confinement fusion", New York, Wiley (1982)

1.3 M.D. Rosen et al, Phys.Fluids, 22, 2020 (1979)

1.4 D.C. Slater et al, Phys.Rev.Lett. 46, 1199 (1981)

1.5 J.J. Thomson, W.L. Kruer, A.B. Langdon, C.E. Max and W.C. Mead, Phys.Fluids 21, 707 (1978)

1.6 K. Estabrook, W.L. Kruer, Phys.Rev.Lett. 40, 42 (1978)

1.7 D.W. Forslund, J.M. Kindel, K. Lee, Phys.Rev.Lett. 39, 284 (1977)

1.8 J.P. Freidberg, R.W. Mitchell, R.L. Morse, L.I. Rudsinski, Phys.Rev.Lett. 28 795 (1972)

1.9 V.L. Ginsburg, "The propagation of electromagnetic waves in plasmas", New York, Pergamon (1974)

1.10 K.A. Brueckner and R.S. Janda, Nucl.Fusion 17, 451, (1977)

1.11 D.T. Attwood, D.W. Sheeney, J.M. Auerbach and P.H.Y. Lee, Phys.Rev.Lett. 41, 1715 (1978)

1.12 M.H. Key, "Lectures on the physics of the superdense region", 20th Scottish University Summer School in

Physics, St Andrews, RL-80-020 (1980)

1.13 P.F. Du Bois and M.V. Goldman, Phys.Rev. 162, 207 (1967)

1.14 K. Nishikawa, J.Phys.Soc.Japan 24, 916 (1968)

1.15 C.G.M. Van Kessel and R. Sigel, Phys.Rev.Lett. 33, 1020 (1974)

1.16 T.J. Goldsack et al, Opt.Comm. 42, 55 (1982)

1.17 Amiranoff et al, Phys.Rev.Lett. 43 522 (1979)

1.18 Yaakobi et al, Opt.Comm. 39, 178 (1981)

1.19 J. Grun et al, Appl.Phys.Lett. 39, 545 (1981)

1.20 T.J. Goldsack et al, Phys.Fluids, 25, 1634 (1982)

1.21 M.H. Key et al, Phys.Fluids 26, 2011 (1983)

1.22 L. Spitzer, "Physics of fully ionized gases", 2nd ed., New York, Wiley (1962)

L. Spitzer and R. Harm, Phys.Rev. 89, 977 (1953)

1.23 R.C. Malone, R.L. McCrory and R.L. Morse, Phys.Rev.Lett. 34, 721 (1975)

1.24 B. Yaakobi and T. Bristow, Phys.Rev.Lett. 38, 350 (1977)

1.25 B. Yaakobi et al, Phys.Fluids 27, 516 (1984)

1.26 A. Hauer et al, Phys.Rev.Lett. 53, 2563 (1984)

1.27 A.R. Bell, R.G. Evans and D.J. Nicholas, Phys.Rev.Lett. 46, 247 (1981)

1.28 D.J. Bond, Phys.Lett. A88, 144 (1982)

1.29 D.W. Forslund et al, Phys.Rev.A 11, 679 (1975)

1.30 J.D. Hares, J.D. Kilkenny, M.H. Key and J.G. Lunney, Phys.Rev.Lett. 42, 216 (1979)

1.31 F. Amiranoff et al, Bull.Am.Phys.Soc. 24, 1054 (1979)

1.32 R.J. Mason, Phys.Rev.Lett. 43, 1975 (1979)

1.33 H.D. Shay et al, Phys.Fluids 21, 1634 (1978)

1.34 D. Duston, R.W. Clark, and J. Davis, Phys.Rev.A 31, 3220 (1985)

1.35 R.J. Trainor, H.C. Graboske, K.S. Long and J.W. Shaner, UCRL No.52562, (1978)

1.36 A.J. Cole, J.D. Kilkenny, P.T. Rumsby, R.G. Evans and M.H. Key, J.Phys.D. Appl.Phys. 15, 1689 (1982)

1.37 J. Clarke, H. Fisher and R. Mason, Phys.Rev.Lett. 30, 89 (1973)

1.38 W.J.M. Rankine, Philos.Trans.R.Soc. London, 160, 277 (1870)

1.39 H. Hugoniot, J.Ecole Polyt., Paris 57, 3 (1887)

1.40 H. Hugoniot, J.Ecole Polyt., Paris 58, 1 (1889)

1.41 R.G. Evans, private communication

1.42 P.C. Thompson, private communication

2.1 P.C. Thompson and P.D. Roberts, Lasers and particle beams, 2, 13 (1984)

2.2 M.H. Key et al, Phys.Fluids 26, 2011 (1983)

2.3 B.H. Ripin et al, Phys.Fluids 23, 1012 (1980)

2.4 B. Meyer and G. Thiell, Phys.Fluids 27, 302 (1984)

2.5 M.D. Rosen et al, 'Shock waves in condensed matter' APS Conference Proceedings, North Holland (1983)

2.6 T.J. Goldsack et al, Opt.Comm. 42, 55 (1982)

2.7 B. Yaakobi et al, J.Appl.Phys. 57, 4354 (1985)

2.8 L.R. Veeser and J.C. Solem, Phys.Rev.Lett. 40, 1291 (1978)

2.9 R.J. Trainor, J.W. Shaner, J.M. Auerbach and N.C. Holmes, Phys.Rev.Lett. 42, 1154 (1979)

2.10 L.R. Veeser, J.C. Solem and J. Lieber, Appl.Phys.Lett. 35, 761 (1979)

2.11 F. Cottet, J.P. Romain, R. Fabbro and B. Faral, J.Appl.Phys. 55, 4125 (1984)

2.12 F. Cottet, J.P. Romain, R. Fabbro and B. Faral, Phys.Rev.Lett. 52, 1884 (1984)

2.13 D. Salzman, S. Eliezer, A.D. Krumbein and L.G. Tier, Phys.Rev.A 28, 1738 (1983)

2.14 R.J. Trainor, H.C. Graboske, R.S. Long and J.W. Shaner, UCRL Report No.52562 (1978)

2.15 Ya. B. Zel'dovich and Yu. P. Raizer, "Physics of Shockwaves and high temperature hydrodynamic phenomena", Academic, New York, 1967

2.16 E.A. McLean et al, Phys.Rev.Lett. 45, 1246 (1980)

2.17 D.W. Forslund, J.M. Kindel, K. Lee, E.L. Lindman and R.L. Morse, Phys.Rev.A 11 679 (1975)

2.18 Giovanelli et al, 'Proc.IEEE Int.Conf. on Plasma Sciences, Austin, Texas, 1976', IEEE, New York 1976

2.19 D. Duston, R.W. Clark and J. Davis, Phys.Rev.A 31, 3220, (1985)

2.20 W.C. Mead et al, Phys.Fluids, 27 1322 (1984)

2.21 W. Seka et al, Opts.Comms. 40, 437 (1982)
M.D. Rosen et al, Phys.Fluids 22, 2020 (1979)

2.22 R.L. McCory and R.L. Morse, Phys.Rev.Lett. 38, 544 (1978)
C.E. Max, C.F. McKee and W.C. Mead, Phys.Fluids 23, 1620 (1980)

2.23 B. Yaakobi et al, J.Appl.Phys. 57, 4354 (1985)

3.1 D. Salzman, S. Eliezer, A.D. Krumbein and L. Gitter, Phys.Rev.A 28, 1738 (1983)

3.2 C.G.M. Van Kessel and R. Sigel, Phys.Rev.Lett. 33, 1020 (1974)

3.3 L.R. Veeser and J.C. Solem, Phys.Rev.Lett. 40, 1391 (1978)

3.4 R.J. Trainor, J.W. Shaner, J.M. Auerbach and N.C. Holmes, Phys.Rev.Lett. 42, 1154 (1979)

3.5 L.R. Veeser, J.C. Solem and A.J. Lieber, Appl.Phys.Lett. 35, 761 (1979)

3.6 R.J. Trainor et al, Appl.Phys.Lett. 43 542 (1983)

3.7 F. Cottet, J.P. Romain, R. Fabbro and B. Faral, Phys.Rev.Lett. 52, 1884 (1984)

3.8 G.A. Lyzenga and T.J. Ahrens, Rev.Sci.Instr. 50, 1421 (1979)

3.9 S.H. Gold and E.A. McLean, 53, 784 (1981)

3.10 S.B. Kormer, Sov.Phys.Usp. 11, 229 (1969).

3.11 S. Eliezer, L. Gitter, A.D. Krumbein and D. Salzman, Phys.Lett. 86, 464 (1981)

3.12 Ya. B. Zel'dovich and Yu. P. Raizer, "Physics of shockwaves or high temperature hydrodynamic phenomena", Academic, New York, 1967, Vol.II

3.13 N.C. Holmes et al, 'Shock waves in condensed matter', AIP Conf. Proc. No.78, AIP, New York, 1982

3.14 C.E. Ragan, Phys.Rev.A 21, 458 (1980)

3.15 L.V. Al'tshuler et al, Sov.Phys.JETP 27, 420 (1968)

3.16 R.F. Trunin, M.A. Poudrets, B.N. Moiseev, G.V. Simakov

and L.V. Popov, Sov.Phys.JETP 29, 630 (1969)

3.17 R.F. Trunin et al, Sov.Phys. JETP 35, 550 (1972)

3.18 D. Duston, R.W. Clark and J. Davis, Phys.Rev.A 31, 3370 (1985)

3.19 F. Cottet, J.P. Romain, R. Fabbro and B. Faral, J.Appl.Phys. 55, 4125 (1984)

3.20 R.M. More, UCRL Rep.No.84911, (1981)
N.C. Holmes, Energy and Technology Review, Oct.1979

3.21 R.J. Harrach et al "Shock waves in condensed matter", AIP Conf. Proc. No.78, AIP, New York (1982)

3.22 M.H. Key et al, Phys.Fluids 26, 2011 (1983)

3.23 R. Grover and P.A. Urtiew, J.Appl.Phys. 45, 146 (1974)

4.1 J. Nuckolls, L. Wood, A. Thiessen and G. Zimmerman, Nature 239, 139 (1972)

4.2 R.A. Haas et al, Phys.Fluids 20, 322 (1977)
H.D. Shay et al, Phys.Fluids 21, 1634 (1978)

4.3 D. Duston, R.W. Clark, J. Davis and J.P. Apruzese, Phys.Rev.A 27, 1441 (1983)

4.4 B. Ahlborn, M.H. Key and A.R. Bell, Phys.Fluids 25, 541 (1982)

4.5 J.D. Hares, J.D. Kilkenny, M.H. Key and J.G. Lunney, Phys.Rev.Lett. 42, 1216 (1979)

4.6 G.A. Lyzenga and T.J. Ahrens, Rev.Sci.Instr. 50, 1421 (1979)

4.7 S.H. Gold and E.A. McLean, J.Appl.Phys. 53, 784 (1982)

4.8 D.W. Phillion, UCRL 50021-78, 6.11, Lawrence Livermore Laboratory Laser Program Annual Report (1978)

N.C. Holmes, R.J. Trainor, D.L. Banner, D.W. Phillion, R.J. Harrach, M.D. Rosen and Y.T. Lee, UCRL 50021-80 7.69, Lawrence Livermore Laboratory Laser Program Annual report (1980)

4.9 E.A. McLean et al, Phys.Rev.Lett. 45, 1246 (1980)

4.10 P.D. Carter, M. Hubbard and R.E. Allison, AWRE Aldermaston Report No.SPE1/83 (1983), unpublished

4.11 Ealing Beck Optics Ltd

4.12 T.H. Bett, P.T. Flynn, C. Ireland, and D. Pitman, AWRE Aldermaston Report No.SFO 48/76 (1976) unpublished

4.13 B. Meyer, G. Morin and G. Thiell, J.Appl.Phys 53, 2947 (1982)

N.A. Ebrahim et al, Phys.Rev.Lett. 43, 1995 (1979)

4.14 S.D. Tabatabaei, private communication

4.15 D. Duston, R.W. Clark, J. Davis, and J.P. Apruzese, Phys.Rev.A 27, 1441 (1983)

4.16 P.D. Carter, AWRE Aldermaston Report No.SPE 46/83 (1983), unpublished

4.17 SESAME, Los Alamos E.O.S. Library

4.18 N.J. Freeman, M. Hubbard, M.H. Noad and P.C. Thompson, AWRE Aldermaston Report No.SPE 33/81 (1981) unpublished

5.1 A.J. Cole, J.D. Kilkenny, P.T. Rumsby, M.H. Key and R.G. Evans, CLF Annual Report, Rutherford Appleton Laboratory, RL83-043 (1983)

5.2 J.H. Gardner and S.E. Bodner, Phys.Rev.Lett. 47, 1137 (1981)

5.3 M.H. Key in "Laser-plasma interactions 2", SUSSP (1982)

5.4 R.G. Evans, A.J. Bennett and G.J. Pert, J.Phys.D. Appl.Phys. 15, 1673 (1982)

5.5 P.C. Thompson and P.D. Roberts, Lasers and particle beams, 2, 13 (1984)

5.6 J. Eastman, J. Boles and J. Soures, Laser Focus 14, 48 (1978)

5.7 M.H. Key, CLF Annual Report, Rutherford Appleton Laboratory, RL82-039 (1982)

5.8 W.M. Manheimer, D.G. Colombant and J.H. Gardner, Phys.Fluids 25, 1644 (1982)

5.9 A.J. Cole, PhD thesis, University of London (1982)

5.10 S.P. Obenschain, R.H. Lehmberg and B.H. Ripin, Appl.Phys.Lett. 37, 903 (1980)

5.11 S.P. Obenschain, J. Grun, B.H. Ripin and E.A. McLean, Phys.Rev.Lett. 46, 1402 (1981)

5.12 M.H. Emery, J.H. Orens, J.H. Gardner and J.P. Boris, Phys.Rev.Lett. 48, 253 (1982)

5.13 A.J. Cole, J.D. Kilkenny, P.T. Rumsby, R.G. Evans and M.H. Key, J.Phys.D.Appl.Phys. 15, 1689 (1982)

5.14 R.H. Lehmberg and S.P. Obenschain, Opts.Comm. 46, 27 (1983)

5.15 D.K. Bradley, R.W. Eason, J.D. Hares, A.J. Rankin, S.D. Tabatabaei, CLF Annual Report, Rutherford Appleton Laboratory, RL85-047 (1985)

5.16 J.L. Bocher, M. Decroisette, P.A. Holstein, M. Louis-Jacquet, B. Meyer, A. Salères and G. Thiell, Phys.Rev.Lett. 52, 823 (1984)

5.17 I. Ross et al, IEEE J, Quant.Electron QE 17, 1653 (1981)

5.18 Hadland Photonics Ltd., Herts, UK

5.19 M.H. Key et al, Phys.Fluids 26, 2011 (1983)

5.20 T.J. Goldsack et al, Optics Comm. 42, 55 (1982)

5.21 J. Grun, private communication

5.22 B. Meyer, G. Morin and G. Thiell, J.Appl.Phys. 53, 2947 (1982)

5.23 Ealing Beck Optics Ltd, England.

5.24 R.W. Eason, private communication

5.25 A.J. Cole, private communication

5.26 D.A. Pepler, private communication

5.27 Los Alamos SESAME E.O.S. Data Library

5.28 C.E. Max, C.F. McKee and W.C. Mead, Phys.Fluids 23, 1620 (1980)

C.E. Max, C.F. MeKee and W.C. Mead, Phys.Rev.Lett. 45, 28 (1980)

6.1 S.P. Obenschain, J. Grun, B.H. Ripin and E.A. McLean, Phys. Rev.Lett. 46, 1402 (1981)

6.2 A.J. Cole, J.D. Kilkenny, P.T. Rumsby, R.G. Evans, and M.H. Key, J.Phys.D.Appl.Phys. 15, 1689 (1982)

6.3 A.J. Cole et al, CLF Annual Report, Rutherford Appleton Laboratory, RL83-043 (1983)

6.4 A.J. Rankin, A.J. Cole, J.D. Kilkenny and M.H. Key, CLF Annual Report, Rutherford Appleton Laboratory, RL83-043 (1983)

6.5 A.J. Rankin et al, CLF Annual Report, Rutherford Appleton Laboratory, RL84-049 (1984)

6.6 J.L. Bocher, M. Decroisette, P.A. Holstein, M.

Louis-Jacquet, B. Meyer, A. Salères, and G. Thiell, Phys.Rev.Lett. 52, 823 (1984)

6.7 H. Kramers, Phil.Mag. 46, 836 (1923)

6.8 A.J. Cole, E. Madraszek and C.L.S. Lewis, 1.74 CLF Annual Report, Rutherford Appleton Laboratory, RL83-043 (1983)

6.9 Ilford Photographic Limited, Basildon.

6.10 "Handbook of Chemistry and Physics", E136, CRC (1983)

6.11 M.H. Key, private communication

6.12 C. Dittmore, private communication

6.13 M.H. Key et al, Phys.Fluids 26, 2011 (1983)

6.14 A.J. Cole, PhD thesis, University of London (1982)

6.15 A.J. Cole et al, CLF Annual Report, Rutherford Appleton Laboratory, RL85-047 (1985)

6.16 R.G. Evans, private communication

6.17 P.C. Thompson, private communication

6.18 B.J. MacGowan, private communication

6.19 J. Grun et al, Phys.Fluids 26, 588 (1983)

6.20 R.D. Richtmyer, Comms. Pure and Applied Maths 13, 297 (1960)

6.21 Y.Y. Meshkov, NASA Report No.N70-30945 (1970)

7.1 C.E. Ragan III, M.G. Silbert and B.C. Diven, J.Appl.Phys.48, 2860 (1977)

7.2 C.E. Ragan, Phys.Rev.A 21, 458 (1980)

7.3 D.D. Bloomquist, S.A. Sheffield, J. Appl.Phys 54, 1717 (1983)

7.4 Kentech Instruments Ltd, London

7.5 Mullard Technical Report on Image Intensifiers, London, Yale (1977)

7.6 A. Hauer, private communication

7.7 A.R.N. Clarke, private communication

7.8 SESAME, Los Alamos, E.O.S. Data Library

7.9 J.P. Christiansen, D.E.F. Ashby and K.V. Roberts, Comp.Phys.Comm. 7, 271 (1974)

7.10 R.E. Turner, W.C. Mead, 1981 Laser Program Annual Report, LLNL 6-34 (1982)

7.11 R.D. Richtmyer, Comms. Pure and Applied Maths 13, 297 (1960)

Y.Y. Meshkov, NASA Rep.No.N70-30945 (1970)

8.1 P.C. Thompson and P.D. Roberts, Lasers and particle beams 2, 13 (1984)

8.2 M.H. Key et al, Phys.Fluids 26, 2011 (1983)

8.3 M.D. Rosen et al, Phys.Fluids 22, 2020 (1979)

8.4 R.L. McCrory and R.L. Morse, Phys.Rev.Lett. 38, 544 (1977)

C.E. Max, C.F. McKee and W.C. Mead, Phys.Fluids 26, 1620 (1980)

8.5 D. Salzman, S. Eliezer, A.D. Krumbein and L. Gitter, Phys.Rev.A 28, 1738 (1983)

8.6 J.L. Borowitz, private communication

8.7 A.J. Cole et al, J. Phys. D. Appl.Phys. 15, 1689 (1982)

J.H. Gardner and S.E. Bodner, Phys.Rev.Lett.47, 1137 (1981)

8.8 W.M. Manheimer, D.G. Colombant and J.H. Gardner,

Phys.Fluids 25, 1644 (1982)

A.1 D.R. Hull, N.J. Freeman and M. Noad, AWRE Aldermaston, Rep.No.SFO 4/79, unpublished